UNIVERSITÀ DEGLI STUDI DI PADOVA

DIPARTIMENTO DI FISICA E ASTRONOMIA GALILEO GALILEI

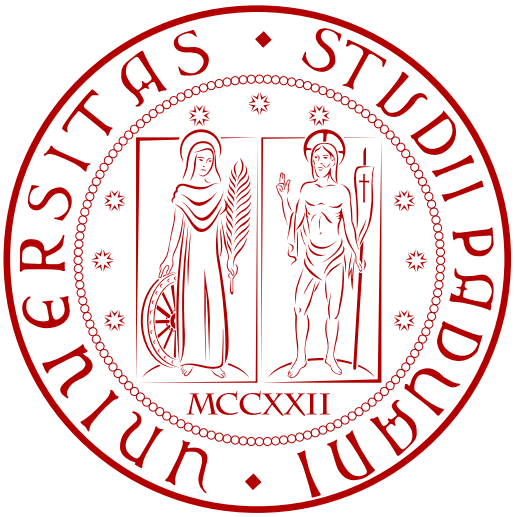

CORSO DI LAUREA MAGISTRALE IN FISICA

BEAM PROPERTY CHARACTERIZATION BY MEANS OF THREE BEAM DIAGNOSTICS AT BATMAN

RELATORE: Dr. Gianluigi Serianni

CORRELATORE: Prof. Dr. Ing. Ursel Fantz

CONTRORELATORE: Prof. Marco Zanetti

LAUREANDO: Roberto Maurizio

Settembre 2015
Anno Accademico 2014-2015

Abstract

ITER is the biggest international fusion experiment ever conceived and it is currently under construction in the south of France: its aim is to prove the technical feasibility of controlled nuclear fusion on earth. It consists of a fusion reactor based on the tokamak concept of magnetic confinement of plasmas; in order to reach the temperature required for the occurrence of thermonuclear reactions, external heating systems are required, like a Neutral Beam Injector (NBI). The neutral beam is obtained from a Hydrogen or Deuterium negative ion beam which is extracted and accelerated from a large RF driven ion source. The RF-driven cesiated negative ion source of the BATMAN (Bavarian Test Machine for Negative ions) test facility, at IPP-Garching (Germany), is since 2007 the ITER prototype source.

The present work has been performed at the IPP-BATMAN test facility during the summer semester of the academic year 2014-2015, in the framework of the Erasmus exchange agreement between the University of Padua and the Ludwig-Maximilians-Universität of Munich.

In *Chapter* 1 a brief introduction on the physics of nuclear fusion and the concept of a fusion reactor is provided: particular emphasis is dedicated to the energy balance in the plasma - between energy production and energy losses - and thus to the need for external heating systems. The ITER experiment is then outlined and one of its external heating systems, the Neutral Beam Heating (NBI), is introduced.

Chapter 2 thoroughly describes the features of a negative hydrogen ion beam source: the creation of negative ions from a low-pressure and low-temperature plasma source (in two possible ways), the extraction and acceleration of the ions by a system of multi-aperture grids. A useful parameter for the characterization of beam optics - the normalized perveance - is introduced and its relation with the beam divergence is discussed from a theoretical and an experimental point of view.

In *Chapter 3* an overview of the main parts of the BATMAN test facility is provided: the source region, where the ions are created, the extraction and acceleration region, where the beam is accelerated, and finally the drift region, where the beam propagates in vacuum and it is analyzed by several beam diagnostics. BATMAN is equipped with five horizontal lines-of-sight for Beam Emission Spectroscopy (BES), a diagnostic calorimeter made of two Carbon-Fiber-Composite tiles (*mini-STRIKE*) and finally a copper calorimeter.

The first part of *Chapter 4* describes the codes written for the analysis of the data from beam diagnostics; the second part of the chapter introduces some important remarks about data analysis, necessary to correctly interpret the experimental results.

In *Chapter 5* a characterization of the negative ion beam properties - e.g. divergence, homogeneity and asymmetries - in different operational scenarios is given: with different magnetic filter field setups, source parameters (e.g the RF power, source pressure, bias current, extraction and acceleration voltages) and finally with different gases. The evolution of the beam features during some Cs-conditioning days of the source is analyzed as well. Possible physical interpretations for the results are discussed, in some cases supported by numerical simulations developed ad hoc.

In *Chapter 6* the main results and open issues are summarized; finally possible future developments of the present work are outlined.

Sommario

ITER è il più grande esperimento internazionale sulla fusione nucleare mai concepito ed è in corso di realizzazione nel sud della Francia; il suo obiettivo è di provare la fattibilità tecnica della fusione termonucleare controllata sulla Terra. Esso consiste in un reattore a fusione basato sulla configurazione tokamak per il confinamento magnetico di plasmi; al fine di raggiungere la temperatura richiesta dalla fusione nucleare sono necessari sistemi di riscaldamento addizionali del plasma, come l'iniettore di fasci di neutri (Neutral Beam Injector, NBI). Il fascio di neutri è ottenuto da un fascio di ioni negativi, Idrogeno o Deuterio, che viene estratto da una sorgente a radiofrequenza (RF) e poi accelerato. La sorgente cesiata a ioni negativi della test facility BATMAN, presso IPP-Garching (Germania), è dal 2007 il prototipo della sorgente per ITER.

Il presente lavoro è stato svolto presso la test facility BATMAN durante il semestre estivo dell'anno accademico 2014-2015, nel contesto dell'accordo di scambio Erasmus tra l'Università degli Studi di Padova e la Ludwig-Maximilians-Universität di Monaco di Baviera.

Nel *Capitolo 1* è fornita una breve introduzione sulla fisica della fusione nucleare e il concetto di un reattore a fusione: particolare enfasi è data all'equilibrio energetico nel plasma - tra energia prodotta e perdite - e alla necessità di sistemi di riscaldamento esterni. Viene quindi descritto l'esperimento ITER e uno dei metodi ausiliari di riscaldamento, il riscaldamento con fasci di neutri (NBI), è introdotto.

Il *Capitolo 2* descrive in dettaglio le caratteristiche di una sorgente di ioni idrogeno negativi: la creazione di ioni negativi da una sorgente di plasma a bassa pressione (con due possibili meccanismi), l'estrazione e l'accelerazione degli ioni tramite un sistema di griglie a molte aperture. É quindi introdotto un parametro utile per la caratterizzazione dell'ottica del fascio - la perveanza normalizzata - e viene discussa la sua relazione con la divergenza del fascio dal punto di vista teorico e sperimentale.

Nel *Capitolo 3* è presentata una panoramica della test facility BATMAN: la regione della sorgente, dove sono creati gli ioni, la regione di estrazione ed accelerazione, dove gli ioni sono portati ad alta energia, ed infine la regione di drift, dove il fascio si propaga in vuoto e viene studiato da diverse diagnostiche. Lo studio delle proprietá del fascio in BATMAN é eseguito mediante cinque linee di vista orizzontali per Beam Emission Spectroscopy (BES), un calorimetro diagnostico - denominato *mini-STRIKE* - costituito da due tegole di un materiale composito unidirezionale in fibra di carbonio, un calorimetro in rame.

La prima parte del *Capitolo 4* descrive i codici scritti per analizzare i dati forniti dalle diagnostiche di fascio; la seconda parte introduce alcune importanti osservazioni sull'analisi dei dati, necessarie per interpretare correttamente i risultati sperimentali.

Il *Capitolo 5* si concentra sullo studio delle proprietà del fascio - come divergenza, omogeneità ed asimmetrie - in diversi scenari operativi: con diversi campi magnetici di filtro, diversi parametri della sorgente (come la potenza RF, la pressione della sorgente, la corrente di bias, le tensioni di estrazione ed accelerazione) e infine con diversi gas. Viene inoltre analizzata l'evoluzione delle caratteristiche del fascio durante alcuni giorni di condizionamento della sorgente con Cesio. Possibili interpretazioni fisiche dei risultati sono presentate, in alcuni casi supportate da simulazioni numeriche sviluppate ad hoc.

Nel *Capitolo 6* vengono sintetizzati i principali risultati e i problemi ancora aperti; infine sono delineati alcuni possibili sviluppi futuri del presente lavoro.

Contents

1 Introduction

Less than a century has passed since the discovery that the energy of the Sun, our main star, is released by *thermonuclear reactions* (1929): soon physicists began to wonder how to reproduce on earth what is happening on the Sun. During the Second World War the idea emerged that a fission explosion could be used to initiate a fusion process analogous to the reactions in the interior of the stars: after the first successful thermonuclear device explosions, discussions on controlled fusion became of great interest. To administrators it appeared that it was possible to put to work in a *controlled and peaceful way* these violent reactions; it was necessary to convince them that achieving the controlled process is *incomparably more difficult* than creating a thermonuclear explosion and that a considerable period of research, experimentation and development must precede any practical application.

1.1 Physics of nuclear fusion

Thermonuclear fusion is a reaction where exceedingly high temperatures, of the order of 10^8 K, permit light nuclei, as Hydrogen isotopes, to approach each other closely enough to *synthesize heavier nuclear species*: fusion of light nuclei in heavy ones liberates energy since the mean binding energy per nucleon decreases up to *Fe* (see Figure 1.1).

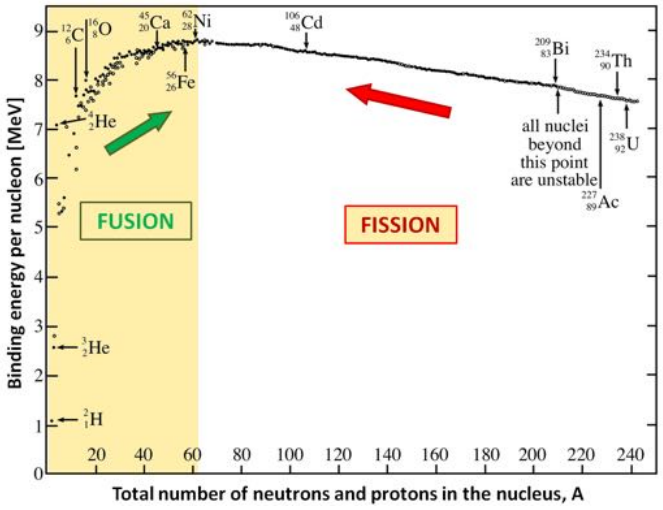

Figure 1.1. Binding energy per nucleon as a function of mass number A.

For example in the Sun the primary reaction is between two protons, namely the fusion of two ^1H nuclei into a nucleus of Deuterium $^2_1H = D$: this reaction is however so slow that is not suitable for energy production on earth. Nevertheless practical alternatives are available:

the most important among them are the reactions involving Deuterium and Tritium (Hydrogen isotopes)

$$D + D \rightarrow T + p + 4.0\ MeV$$
$$D + D \rightarrow He^3 + n + 3.3\ MeV$$
$$D + T \rightarrow He^4 + n + 17.6\ MeV$$

Figure 1.2a shows the cross section for these reactions, as a function of the kinetic energy of the reagent particles; it is clear that, at fixed kinetic energy, the D-T fusion is the most probable reaction up to about 400 keV. In Figure 1.2b the product of the cross section σ for a fusion reaction and the relative velocity v of the colliding particles, averaged on the Maxwell distribution of the positive ions in the plasma, is shown: again it may be noted that D-T reaction is clearly favorable in comparison with D-D or D-He^3 and for this reason it has been chosen as the main reaction in future fusion reactors.
Moreover, the released energy (17.6 MeV) is given to the products as kinetic energy. As a result of the different mass, the energy is not equally distributed: the lighter particle is the more energetic

$$D + T \rightarrow He^4(3.5\ MeV) + n(14.1\ MeV)$$

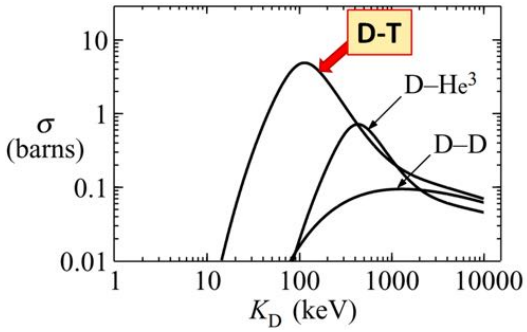

(a). Experimentally measured cross sections for some fusion reactions as a function of deuteron kinetic energy K_D [1]

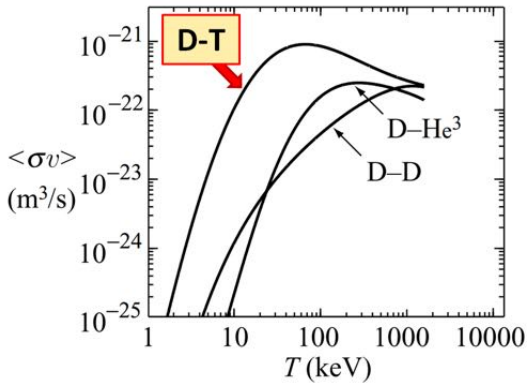

(b). Velocity averaged cross section $\langle \sigma v \rangle$ for some nuclear fusion reactions [1]

Figure 1.2

1.2 Concept of a fusion reactor

The essential condition to realize the fusion reaction in laboratory is to reach very high temperatures; wherever such high temperatures are present we run into formidable obstacles. In the hypothesis that temperatures of the order of 10^8 K can be achieved, the fusion fuel (Hydrogen and Deuterium gases) would be completely ionized: it would be a very hot *plasma*.

The first critical obstacle is the **confinement of the reaction**: the plasma must not come into contact with the walls of the reactor, because no material can resist its erosion. There are, so

far, two approaches for the confinement.
The first is to use the fuel at relatively low density, confined by strong magnetic fields, and thereby slow down the reaction so that it can be reasonably guided: this approach is called "***Magnetic confinement***" and it is exploited in the "*Tokamak*" reactor.
The other approach is to bring the fuel to extremely high densities. Explosions similar to those occurring in the hydrogen bomb can be produced, though the individual explosion will have less that one-millionth the energy output of an hydrogen bomb: this approach is called "***Inertial confinement***".

The *magnetic confinement* has been chosen by the international community as the operational scenario for ITER fusion reactor; the most common shape of the reactor chamber, which will contain the burning plasma, is a *torus* (like a doughnut).

Another critical point, regarding the energy production from fusion, is to achieve a **steady-state**: a balance must be reached within the plasma between energy input and inevitable energy losses.
The two main balancing effects are the following: on the one hand, energy production in the thermonuclear reactions with deposition of *part* of this energy in the plasma - indeed the energetic and positively charged reaction products share, by collisions, their energy with the particles in the plasma - together with *external heating systems*; on the other hand there is energy loss, due to loss of plasma on the walls (diffusive processes and convective transport) and via radiation (Bremsstrahlung radiation). This balance is described by the equation:

$$S_f + S_h = S_B + S_k \tag{1.1}$$

where S_f is the fusion power density, S_h the power density from external heating systems, S_B and S_k refer respectively to radiation and diffusive losses.
The fusion power density S_f is the product of the densities of the two colliding partners n_1 and n_2 (D and T) with the velocity-averaged D-T cross section $\langle \sigma v \rangle$ and the energy released in a single fusion reaction E_f: $S_f = E_f n_1 n_2 \langle \sigma v \rangle$. However, since Equation 1.1 applies to the plasma and only the alpha particles (^4He nuclei) contribute to heat the plasma, $E_f = E_\alpha$ (without the energy of the neutrons) and so $S_f = S_\alpha$: indeed the alpha particles, being charged, are confined by the magnetic field within the plasma, providing a source of heat. On the contrary, neutrons, which are neutral, escape from the plasma and heat the walls of the reactor by collisions; such heat is removed by a cooling system and it is used for electricity production.

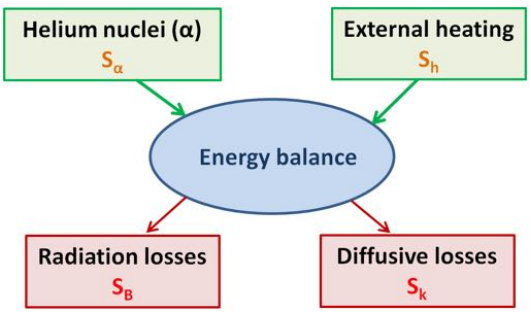

(a). Energy balance in a steady-state fusion plasma.

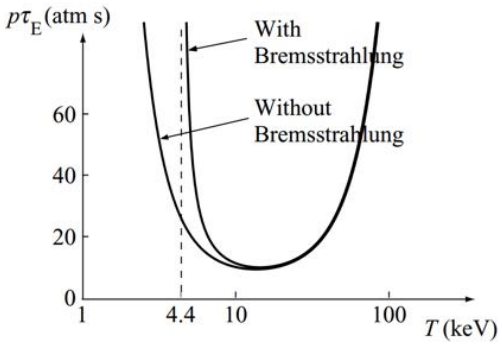

(b). Critical $p\tau_E$ for ignition as a function of temperature [1].

Figure 1.3

Transport processes such as diffusion, convection and charge exchange are empirically described by the energy confinement time τ_E; thereby the energy balance (Eq.1.1) can be rewritten to the ignition condition:

$$n\tau_E = \frac{12kT}{\langle\sigma v\rangle\epsilon_\alpha - 4c_1 Z_{eff}(kT)^{1/2}} \tag{1.2}$$

where n is the plasma density, T the plasma temperature, ϵ_α=3.5 MeV the energy of the α-particle, c_1 the bremsstrahlung constant and Z_{eff} the effective charge of the plasma (including all impurity species) [2]. Figure 1.3b shows the analogous quantity $p\tau_E$, where p stands for plasma pressure: one can notice that $p\tau_E$ must exceed a certain minimum value for *ignition* to occur, and that this value depends on the plasma temperature. The ignition corresponds to the condition of steady state power balance in the plasma with no external power heating: the alpha power heating is sufficiently large to balance the radiation and diffusive losses.
The *simplest ignition condition* is obtained at the minimum of the curve, T_{min} = 15 keV and $(p\tau_E)_{min}$ = 8.3 atm s.

1.2.1 External heating devices

The presence of external heating systems in a fusion reactor is necessary mainly for two reasons [3].
Firstly, in the contemporary fusion experiments external heating systems are required to maintain the plasma against thermal conduction losses and achieve both high temperature and a steady-state energy situation (Eq. 1.1).
Secondly, the magnetic configuration requires a toroidal current to hold the plasma in equilibrium: such current can be efficiently driven by external heating systems. External heating is used also for controlling plasma instabilities and reducing losses.

There are mainly three methods to externally heat the plasma: (1) *Ohmic Heating*, (2) *Radio Frequency Heating*, (3) *Neutral Beam Heating (NBI)* (see Figure 1.4).

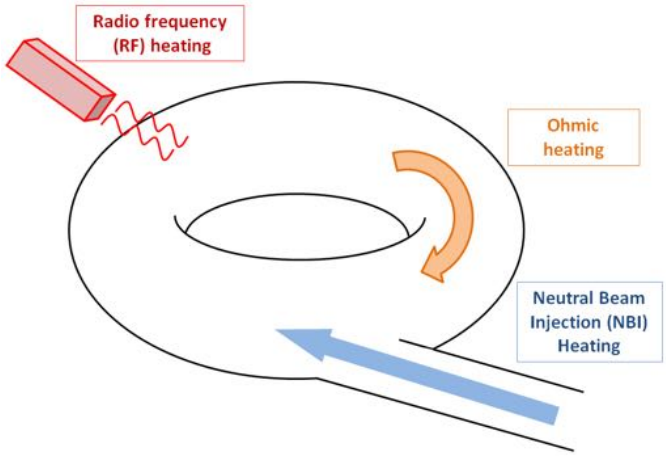

Figure 1.4. Typical heating systems in a fusion reactor.

Ohmic Heating : a toroidal current, driven along the torus, heats the plasma according to the Ohm law $P = R \cdot I_p^2$, where R is the Ohmic resistance of the plasma, I_p the current and P the power deposition. The current in the plasma is induced by the variation in time of the

poloidal magnetic field generated by an external coil located at the center of the torus. Since R is inversely proportional to the temperature of the plasma, the Ohmic heating efficiency decreases along the process, leading to a maximum achievable temperature far lower than the required temperature.

Radio frequency heating: high frequency electromagnetic waves are injected into the plasma and, depending on the frequency, different components and locations of the plasma are heated. The typical frequencies belong to the range of the low frequency Alfven waves ($1 \div 10$ MHz), ion cyclotron frequencies ($30 \div 100$ MHz), lower hybrid frequencies ($1 \div 10$ GHz) and electron cyclotron frequencies ($50 \div 150$ GHz).

Neutral beam heating: negative or positive ions, accelerated at very high energies ($50\ kV \div 1\ MV$), are neutralized, penetrate the reactor border magnetic field and via collisions with electrons and ions are finally ionized and trapped. They will transfer their kinetic energy to the plasma by collisions, thereby heating the plasma.

1.3 The Tokamak concept and ITER

Serious work on the Tokamak concept, that confines low-pressure fuel by strong magnetic fields, started in the early 1950s; the name *"Tokamak"* derives from the Russian words for "magnetic toroidal camera".

In a plain **toroidal magnetic field**, charged-particle orbits are not localized and consequently a finite body of plasma cannot be held in equilibrium: the remedy is the addition of a toroidally directed plasma current. Such a current generates a **poloidal magnetic field** component that localizes the particles and thus establishes the possibility of plasma equilibrium. When the poloidal field is quite smaller than the basic toroidal field, the magnetic configuration is called a *Tokamak*; typical radial profiles of the toroidal (B_ϕ) and poloidal (B_θ) field strength in a tokamak are shown in Figure 1.5. Moreover a **vertical magnetic field** is added, whose aim is to control better the vertical position of the plasma.

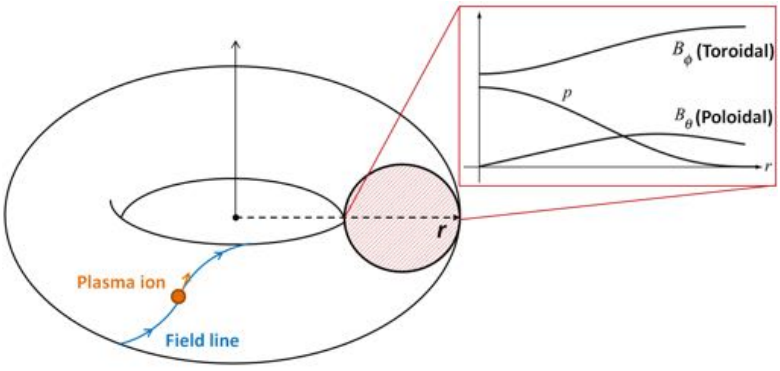

Figure 1.5. Typical radial profiles of toroidal (B_ϕ) and poloidal (B_θ) magnetic fields in a Tokamak.

In a tokamak a set of massive toroidal field coils generates the main toroidal magnetic field component; the plasma is inside a toroidal steel vacuum chamber ("vacuum vessel") and is primarily heated by currents, flowing in the plasma, induced by the toroidal primary winding (sometimes an iron core can be added at the center of the tokamak to improve this coupling).

Typical tokamak operation consists of pulse-filling the chamber with hydrogen gas which is ionized by RF heating (typically the ECRH, electron cyclotron resonance heating): as the plasma current builds up, ohmic heating raises the temperature. Hence, energetic neutral beams and/or high frequency electromagnetic waves are injected into the plasma to achieve the temperature required for fusion to occur.

ITER challenges and PRIMA site The largest fusion experiment ever conceived, named ITER, is currently under construction in the south of France and it is based on the tokamak concept of magnetic confinement (a cut-out section is shown in Figure 1.6). The primary mission of ITER is *to produce a stable, well-conditioned, Q = 10 plasma lasting for only 400 s in the inductive quasi-steady-state scenario and to produce a Q = 5 plasma for non-inductive steady-state scenarios* (Q is the ratio of the output power to the input power in the plasma, namely the gain) [1].

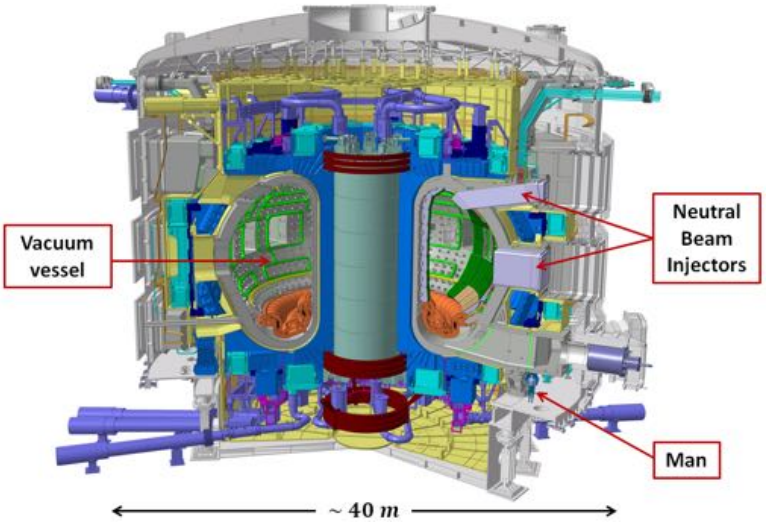

Figure 1.6. Cut section of ITER fusion reactor.

As shown in Figure 1.6, ITER requires neutral beam injection: as it will be explained in the next chapter, the beam comes from a negative ion source. *Negative ion beam sources are a relatively young and challenging area of research*; to study and characterize the properties of the ITER-like negative ion beam, a test facility is currently under construction in Padova (Italy), *PRIMA* (Padova Research on ITER Megavolt Accelerator) [8].
The facility includes a full-size negative ion source, *SPIDER* (Source for Production of Ion of Deuterium Extracted from RF plasma) and a prototype of the whole ITER injector, named *MITICA* (Megavolt ITER Injector and Concept Advancement), shown in Figure 1.7.

1.4 Neutral Beam Heating

In order to get a high-energy neutral beam, it is necessary to accelerate ions in a first step. A charged beam would never penetrate the plasma because it would be deflected out by the strong confining magnetic fields: the charged beam must then be neutralized before injection into the reactor. The beam is composed by the same species as the fusion fuel, H or D: in this way the

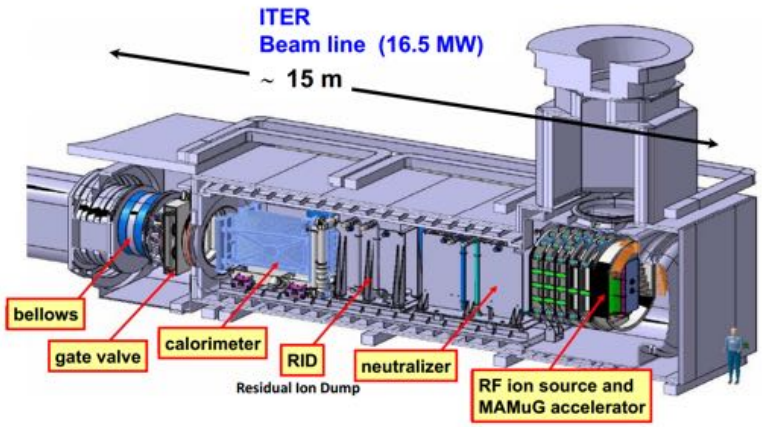

Figure 1.7. Cut-out section of MITICA neutral beam test facility, a person is shown on the lower right for comparison.

beam does not dilute the fuel.
A detailed description of beam generation and neutralization will be given in the next chapter; here a treatment of the physical mechanisms involved in the absorption of the neutral beam in the plasma is provided.

1.4.1 Beam absorption into the plasma

As the neutral beam penetrates into the plasma it is gradually absorbed, namely the neutrals are ionized and thus are trapped along the magnetic field lines. The neutralization consists of three reactions: *collisional ionization by electrons* (Eq. 1.3), *collisional ionization by plasma ions* (Eq. 1.4), *charge exchange with plasma ions* (Eq. 1.5).

$$H_{beam} + e^- \rightarrow H^+_{beam} + 2e^- \tag{1.3}$$

$$H_{beam} + H^+ \rightarrow H^+_{beam} + H^+ + e^- \tag{1.4}$$

$$H_{beam} + H^+ \rightarrow H^+_{beam} + H^0 \tag{1.5}$$

The flux of ions Γ_b represents the number of ions flowing per second and unit area through a section of the beam perpendicular to its direction. This quantity decreases along the path according to the following equation:

$$d\Gamma_b/dx = -n_p \sigma_\Sigma \Gamma_b \tag{1.6}$$

where n_p is the plasma density while σ_Σ stands for the total neutralization cross section:

$$\sigma_\Sigma = \frac{\langle \sigma_{ie} v \rangle}{v_b} + \sigma_{cx}(v_b) + \sigma_{ii}(v_b)$$

where σ_{ie}, σ_{ii} and σ_{cx} are the cross sections for the reactions of Eq. 1.3, Eq. 1.4 and Eq. 1.5 respectively.
The cross section of each neutralization process and the total cross section σ_Σ depend on the relative velocity of the colliding partners v_b, which is proportional to the energy of the beam. The total cross section is found to decrease steadily with the energy of the beam ($\sim 1/E$), as shown in Figure 1.8.

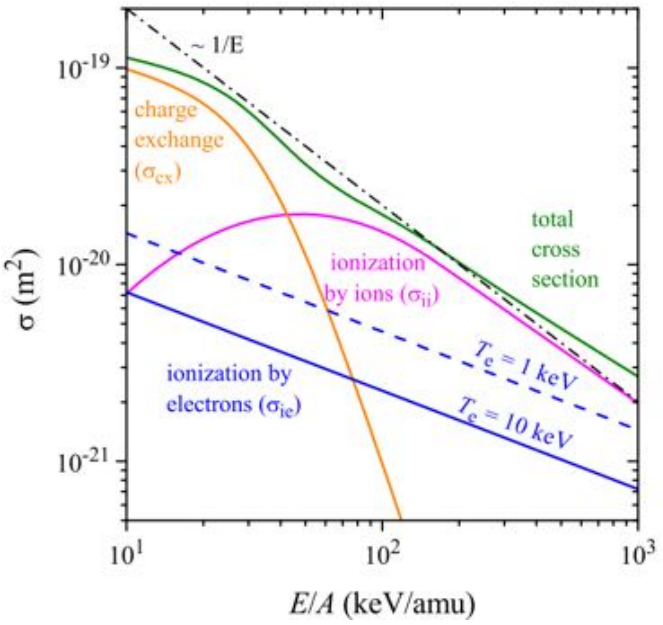

Figure 1.8. Ionization cross sections for collisional ionization by electrons σ_{ie}, collisional ionization by plasma ions σ_{ii} and charge exchange with plasma ions σ_{cx} [3].

The solution of Eq. 1.6 is an exponential with a ***decay length*** (Eq. 1.7) depending strongly on the beam energy via the total cross section: the more energetic is the beam, the lower is σ_Σ, the higher is the penetration length of the beam in the plasma (i.e. the distance after which beam flux is reduced by a factor $1/e$).

$$\lambda = \frac{1}{n_p \sigma_\Sigma(E)} \tag{1.7}$$

Hence, changing the beam energy allows to *regulate the penetration length of the beam.*
A short decay length is undesirable since most of the energy is deposited on the outside of the plasma; a long decay length leads to a high deposition in the center but can also results in the escape of the not ionized portion of the beam from the plasma. The *optimal* decay length depends on the dimensions and characteristics of the reactor; for instance in ITER the optimal decay length corresponds to a **beam energy of 1 MeV**. Such an energy implies, as it will be explained in the next chapter, the use of a *negative* ion source: this is a relatively young, challenging and demanding technology and constitutes an intense field of research.

2 Negative ion source overview

The main parts of a *neutral* beam source are schematically illustrated in Figure 2.1, which is dedicated to:

1. Beam generation
2. Beam neutralization
3. Beam transport

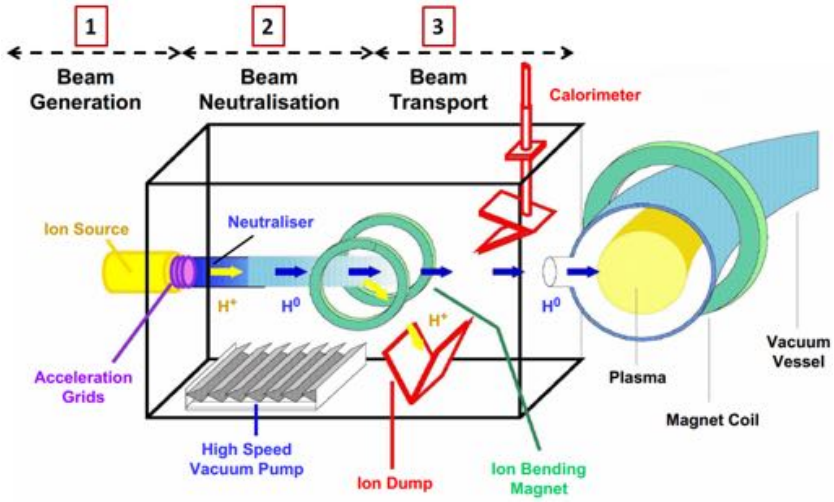

Figure 2.1. Schematic view of a neutral beam heating system [3].

The purpose of the first stage is to generate an accelerated charged beam: this task is accomplished by a *positive or negative ion source*.
The second stage consists in the neutralization of the beam. The *neutralizer* is usually a water-cooled drift tube filled with hydrogen gas: the charged particles collide with the gas and a certain fraction of them, depending on beam energy and charge, is neutralized by charge-exchange processes.
In the last stage the charged component of the beam is deflected out by a strong magnetic (or electric) field into an ion *dump*: the remaining neutral beam is injected into the plasma.

This chapter concentrates on the description of the first step, namely the generation of a charge beam.

2.1 Positive and negative ion sources

Two possible types of hydrogen ion source are possible: *positive* ion source, producing a H^+ beam, or *negative* ion source, producing a H^- beam.

In a **positive ion source**, the H^+ or D^+ can be easily created by standard techniques: the ions are produced as positively charged species of a low-temperature plasma, then extracted and accelerated to the required energy. One challenge that has been successfully addressed is the minimization of the number of molecular H_2^+ and H_3^+ ions with respect to the number of H^+ ions: the molecular ions, because of their higher mass, ultimately produce less energetic neutrals than those produced by atomic hydrogen, leading to a low penetration into the plasma and an undesirable heating of plasma edges. This kind of source is commonly used in all the major running tokamaks nowadays.

A **negative ion source** is on the contrary more challenging, since negative ions are much *more difficult to produce*.
The physical concept is in principle simple: in a partially-ionized hydrogen (or Deuterium) plasma an electron attaches to a neutral hydrogen atom producing H^-, which is ultimately extracted and accelerated. Nevertheless the hydrogen atom has a crucial property: the binding energy of the electron is very low (0.75 eV), therefore the electron can be relatively easily stripped away by collisions with gas or plasma. This effect limits the amount of ion current extracted and accelerated.

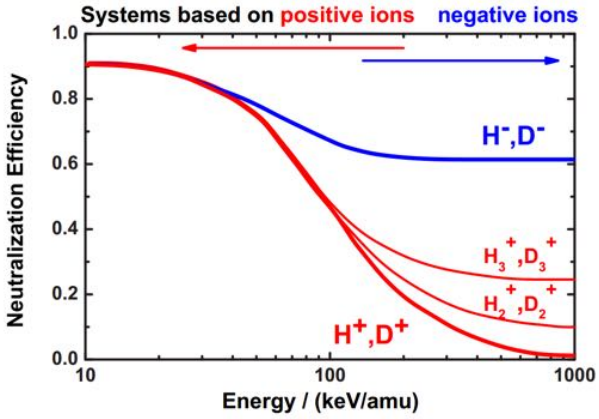

Figure 2.2. Neutralization efficiency for positive and negative hydrogen ions versus beam energy per nucleon [3].

The neutralization efficiency for a positive or negative hydrogen ion beam as a function of beam energy per nucleon is shown in Figure 2.2: the efficiency of positive ion neutralization decreases steadily with beam energy, while it saturates at about 60% for negative ions. This basically means that a high-energy positive ion beam, for istance at 1 MeV (as required by ITER), can be neutralized with very low efficiency and thus cannot be injected into the plasma: *the ITER neutral beam must come from a negative ion source.*

The development of a negative-ion beam source for ITER is an important area of current fusion technology research; it started in the early 90s in Japan (NBI of experiments LHD and JT-60U) and in the end of 90s at IPP Garching-Germany (experiments MANITU, RADI, BATMAN and, more recently, ELISE). In July 2007 the IPP RF source was chosen by the ITER board as the **reference design for the source of ITER negative-ion neutral beam injectors**.

2.2 Negative ion production

There are basically two mechanisms to create negative ions in a plasma source, *volume production* and *surface production*: these processes are here briefly treated.

2.2.1 The volume source

The aim of volume source is to maximize the production of negative ions by *dissociative attachment* of electrons on high vibrational states of hydrogen molecules ([4]): the process is made up of two steps and it takes place in the so-called *"tandem-source"* (Figure 2.3).
A tandem source comprises two regions, the driver or source chamber and the expansion chamber, separated by a magnetic field. The driver contains some permanent magnets, to create a multi-cusp configuration for plasma confinement, and either *heated filaments* in arc discharge sources or the *radio-frequency (RF) antenna* in RF sources. A description of a typical RF source is here provided.

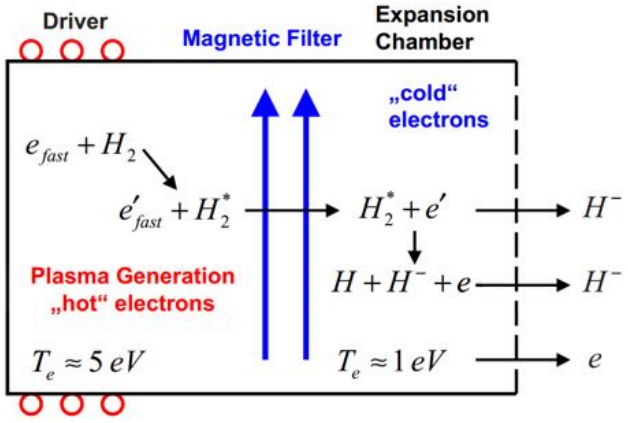

Figure 2.3. Two-step volume production of negative ions in a tandem source [5].

Firstly, the H_2 molecules are excited to high vibrational levels by collisions with fast electrons (T_e about $5 \div 10$ eV) in the driver region:

$$e_{fast} + H_2 \rightarrow e'_{fast} + H_2^* \tag{2.1}$$

The electrons belong to the plasma created by the RF coil; the rate of the process can in principle be enhanced by increasing the source pressure or RF power.

Secondly, the excited H_2^* molecules drift to the expansion chamber. Via dissociative attachment reactions with "cold" electrons ($T_e < 2$ eV) negative ions H^- are finally created:

$$H_2^* + 2e^- \rightarrow H + H^- + e^- \tag{2.2}$$

Unfortunately, the hydrogen negative ions can be easily destroyed mainly by three processes:

- the electron stripping:
$$H^- + e^- \rightarrow H + 2e^-$$
which is very effective for $T_e > 2$ eV

- the mutual neutralization:

$$H^- + H^+ \rightarrow 2H$$

  which depends slightly on ion temperature

- the associative detachment:

$$H^- + H \rightarrow H_2 + e^-$$

  which depends slightly on ion temperature too

The predominant destruction process is the *electron stripping*; in order to minimize it, a magnetic field filters the "hot electrons" ($T_e > 2$ eV) out of the expansion chamber (the details are given in the next paragraph). Consequently, the dissociative attachment reaction rate is enhanced and the destruction of H^- by hot electrons is minimized.

Filter Field physics In the presence of a magnetic field, a particle with mass m and charge q will spiral around one magnetic line of force. Its velocity along the line is arbitrary, since the motion along the line of force is not influenced by the field; on the contrary, the motion on the plane perpendicular to the line of force is circular, on a gyroradius (known as Larmor radius)

$$r = \frac{mcv_\perp}{|q|B} \tag{2.3}$$

where $v_\perp$ is the particle velocity on such plane and B the magnetic field intensity. If in vacuum, the particle (for instance one electron) would just spin in its Larmor orbit and move freely along the field line of force. In the presence of a gas and a density gradient ∇n of the particle species, when the particle collides with another charge or a neutral, its guiding center can get shifted and there can be a cross-field diffusion along the density gradient ∇n (Figure 2.4). In an ion source an electric field is moreover present: it stems from the potential drop between the plasma and a metallic grid - known as plasma grid, PG - which faces directly the plasma and extracts negative charges. The electron can thereby move towards the plasma grid, where it is co-extracted with negative ions H^-.

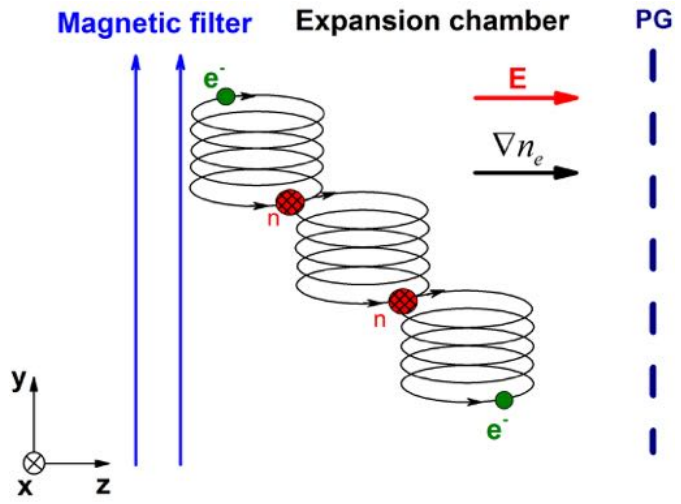

Figure 2.4. Diffusion of an electron across a (horizontal) magnetic field due to collisions.

The cross-field diffusion of the electron, however, depends on its velocity. Indeed the velocity of the electron affects considerably its capability to interact with the gas via Coulomb scattering: the collision frequency with other particles is inversely proportional to the third power of the electron velocity [6]:

$$\nu_e = n_e \sigma_C(T_e) v_e \sim v_e^{-3} \sim T_e^{-3/2} \tag{2.4}$$

Therefore hot electrons are much less collisional than cold electrons: the former diffuse more slowly and are trapped by the filter field, while the latter are able to reach the plasma grid.

2.2.2 The surface source

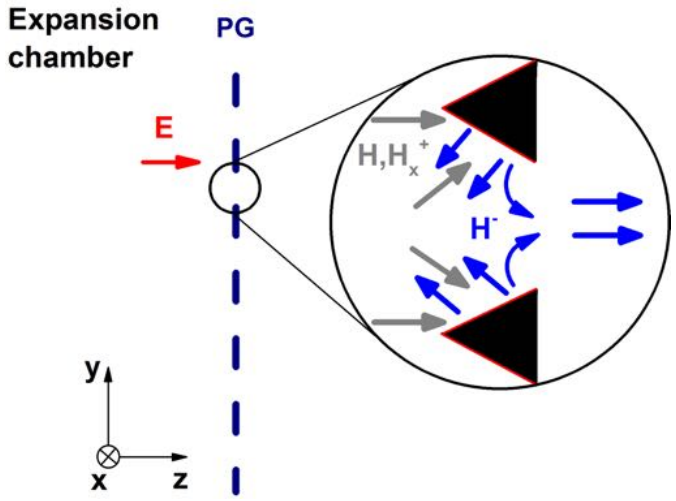

Figure 2.5. Chamfered holes at the plasma grid (PG) increase the extraction probability of surface generated H^-.

The "surface effect" consists in the conversion of neutral or positive hydrogen ions to negative ions after they collide with a material surface (the plasma grid, PG), due to the capture of one electron: the probability of electron capture depends strongly on the work function Φ of the surface [7]. This dependence can be easily quantified with the negative ion yield per H impact on the wall [3]:

$$Y(H^-/H, H^+) = \exp(-\frac{\Phi - A}{C \cdot v_\perp}) \tag{2.5}$$

where C is a constant, $v_\perp$ is the perpendicular velocity of the escaping ion, A the affinity of the electron (0.75 eV for negative hydrogen ions) and Φ the work function of the surface. Minimization of the difference $\Phi - A$ enhances the electron capture probability: this is usually obtained by lowering the PG-surface work function with **Cesium coverage** of the grid surface. The optimal amount of Cesium is about *0.6 monolayers* ([3]), which allows up to 0.67 H^- per incident atom or ion to escape, depending on its energy.
In all the current ion sources the typical value of the negative ion yield for impacting H or H^+ is always in the range $10^{-2} \div 10^{-1}$. In order to enhance the effective area for production of negative ions and facilitate the extraction, chamfered apertures instead of flat apertures can be used in the plasma grid (see Figure 2.5).

2.3 Negative ion extraction and acceleration

The extraction and acceleration system of a negative ion source is generally made of three grids: the *plasma grid* (PG), the *extraction grid* (EG) and the *grounded grid* (GG). The **extraction** phase takes place in the first gap, the **acceleration** phase in the second gap. The acceleration phase can be divided in several high voltage steps: for example the ITER accelerator will have five grids for five acceleration stages of 200 keV each (MAMuG accelerator) [8].

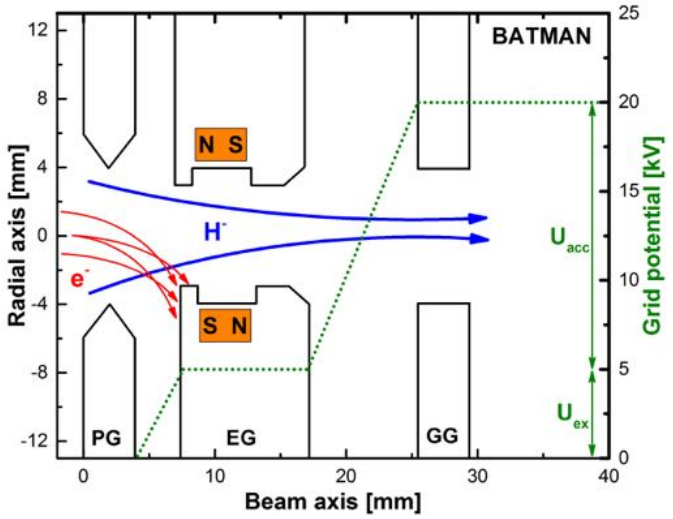

Figure 2.6. Typical extraction and acceleration system for a negative ion source, made up of three multi-aperture grids and two gaps (setup of BATMAN test facility, IPP); in this case $U_{ex} = 5$ kV, $U_{acc} = 15$ kV.

In the extraction phase it is necessary to minimize the co-extracted electrons before the acceleration gap: strong permanent magnets, embedded in the second grid, bend the electrons and force them to hit the extraction grid (Figure 2.6).

Stripping losses in the accelerator Inside and after the first acceleration gap, part of the H^- of the beam are converted into fast neutrals by collision with neutral background gas H_2 (*stripping* of the electron):

$$H_f^- + H_2 \rightarrow H_f^0 + H_2 + e \tag{2.6}$$

Such neutrals, known also as *stripped particles*, cannot be accelerated any further: they make up a low-energy component of the beam. The rate of the process is proportional to the pressure of the source (density of H_2); as a consequence, ITER requires a low source pressure, 0.3 Pa.

At 0.3 Pa and in volume production the extracted current density j_{ex} is *far lower than ITER requirement*: few mA instead of 32.9 mA/cm^2 for hydrogen. This happens because the volume production means a lot of co-extracted electrons: the limit of the electron-load on the EG in turn limits the H^- extracted. The only way to achieve ITER requirement is working in surface production mode.

2.4 Negative ion beam properties: beam divergence

One of the most important properties of a charged beam is the ***beam divergence***, measured in degrees (°). This quantity basically describes the angular spread of the particle trajectories around the beam axis: a well-focused beam is characterized by a low divergence, a bad-focused beam by a high divergence.
If we consider a **beamlet** which exits from an aperture of the grounded grid and drifts in the vacuum vessel, its size will increase due to space-charge repulsion and the particle trajectories will deviate from the beamlet axis. The distribution of the angle between each trajectory and the beamlet axis is generally assumed to be Gaussian, centered in zero; the beamlet divergence is by definition the *e-folding half-width* of such Gaussian, $\sqrt{2}\sigma$ (σ is the standard deviation).
In the case of a multi-aperture extraction and acceleration grid system, as the LAG in BATMAN ion source, the beam is the superimposition of many beamlets.

The divergence is an optical property of the beam and it therefore depends strongly on the geometry of the extraction and acceleration system. The grids constitute indeed a *system of electrostatic lenses* ([9]), and a strong analogy between charged and light beams is usually adopted: as a light beam can be focused or de-focused by the lenses, similarly a charged beam can be focused or de-focused by the electric or magnetic fields between the grids.

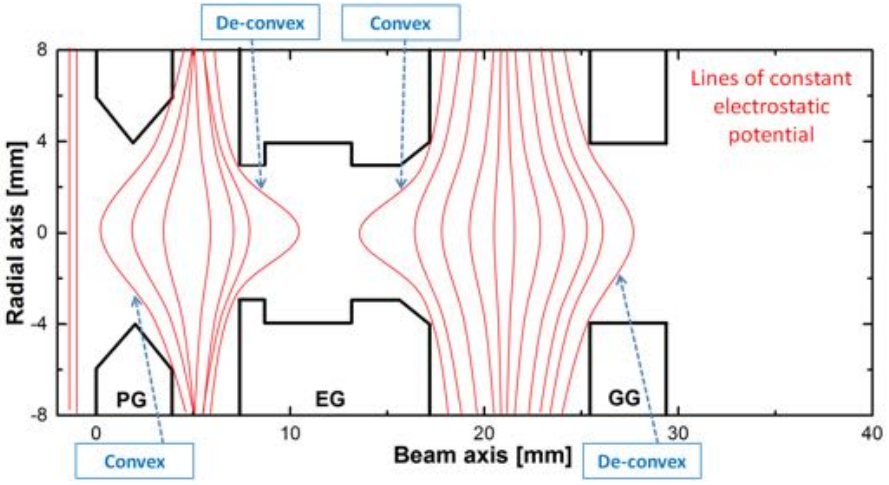

Figure 2.7. Lines of constant electrostatic potential between the plasma grid, the extraction grid and the grounded grid. The optical effect on the beamlet for each grid aperture is also indicated: a convex lens is focusing, a de-convex lens is de-focusing.

The distortion of equipotential lines near one aperture of each grid is shown in Figure 2.7, while Figure 2.8 shows the *equivalent system of electrostatic lenses*. The optical properties of each grid aperture, like the focal length, depend mainly on the electric field on both sides of the grid aperture.
The electric field present in the extraction gap penetrates both the PG aperture, forming a focusing lens (often known as *meniscus*), and the EG aperture, forming a de-focusing lens; the meniscus is also the plasma boundary during extraction and starting point of H^-. Similarly the electric field of the acceleration gap enters the EG, creating a focusing lens, and the GG, creating a de-focusing lens.
As a result, the PG aperture acts always as a focusing lens and the GG aperture as a de-focusing lens (see Figure 2.8). On the contrary the optical properties of the EG are not straightforward.

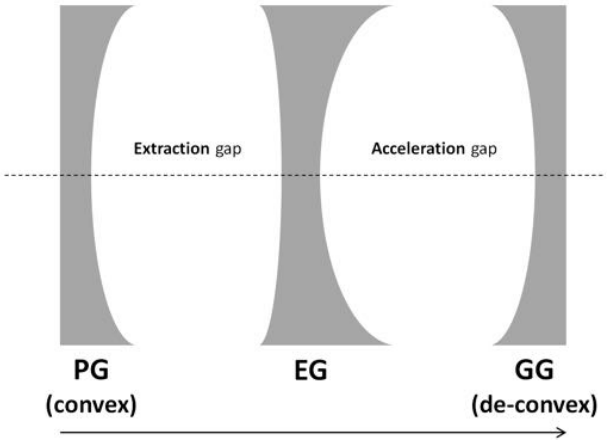

Figure 2.8. The grid system for beam extraction and acceleration can be conceived as a system of electrostatic lenses.

Indeed the EG aperture consists of a (1) de-focusing lens on the left side, a (2) focusing lens on the right side and a (3) potential-free region between them (the EG is rather thick due to the embedded magnets): an incoming beamlet is therefore de-focused by (1), expands because of space charge repulsion within the potential free region (3) and finally is focused by (2). Consequently the EG can be focusing or de-focusing, depending on the extraction and acceleration voltages.

A useful parameter in the characterization of the beam optics, as it will be shown in the next section, is the *perveance*: this quantity is strongly correlated to the optical properties of the extraction and acceleration grids.

2.4.1 Perveance definition

The perveance of a charged beam is defined as the ratio of the beam current I_{ex} to the three-halves power of the extraction voltage U_{ex} [10]:

$$\Pi = \frac{I_{ex}}{U_{ex}^{3/2}} \tag{2.7}$$

The maximum possible extracted current I_{ex}^{max} for a radially symmetric ion beamlet is limited by the space charge of the beamlet and is given by the Child-Langmuir Law:

$$I_{max} = \frac{4}{9}\pi\epsilon_0\sqrt{\frac{2e}{m}}\left(\frac{r}{d}\right)^2 U_{ex}^{3/2} \tag{2.8}$$

This equation is obtained for a beamlet of electrons extracted between two electrodes but it is valid also for beamlet of negative ions. The electrodes have radius r and relative distance d and a voltage difference is applied between them; the electric field accelerates the electrons emitted by the surface of the first electrode due to Thermoionic effect (the electrode is heated) towards the second surface. The continuous flux of charges between the plates constitutes a space charge which alters the potential distribution (Figure 2.9): as the current is increased, the potential

develops a concavity. The current cannot increase beyond the point where the potential curve becomes horizontal at P, because any further increase in current would make the potential curve slope at P downwards and the negative particles would be unable to overcome the potential well.

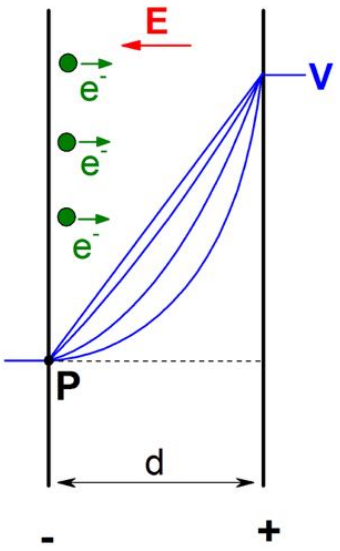

Figure 2.9. Concept of the Child-Langmuir Law.

The maximum perveance can thereby be computed:

$$\Pi_0 = \frac{I_{ex}^{max}}{U_{ex}^{3/2}} = \frac{4}{9}\pi\epsilon_0\sqrt{\frac{2e}{m}\left(\frac{r}{d}\right)^2} \tag{2.9}$$

and the *normalized perveance* is by definition the ratio Π/Π_0.

2.4.2 Beam divergence dependence on normalized perveance

The normalized perveance Π/Π_0 includes all the optical features of the grid system and thus determines the optical properties of the accelerated beam, namely the position of the *focus point* and the *beam divergence*.

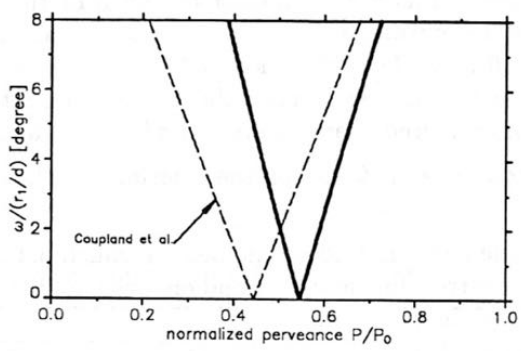

Figure 2.10. Theoretical relation between the maximum opening angle of a charged beamlet and its normalized perveance, here as P/P_0, as in [11].

A simple theoretical treatment of the relation between the normalized perveance of a beamlet and its final divergence can be found in [11]: Figure 2.10 shows the maximum opening angle of the beamlet as a function of the normalized perveance of the beamlet. The optimum of the perveance is defined as the value which corresponds to the minimum of the divergence; moreover, as the real extraction geometry is far more complicated than the one adopted in the model of [11], it is reasonable to expect that the data will not completely agree with this rule.

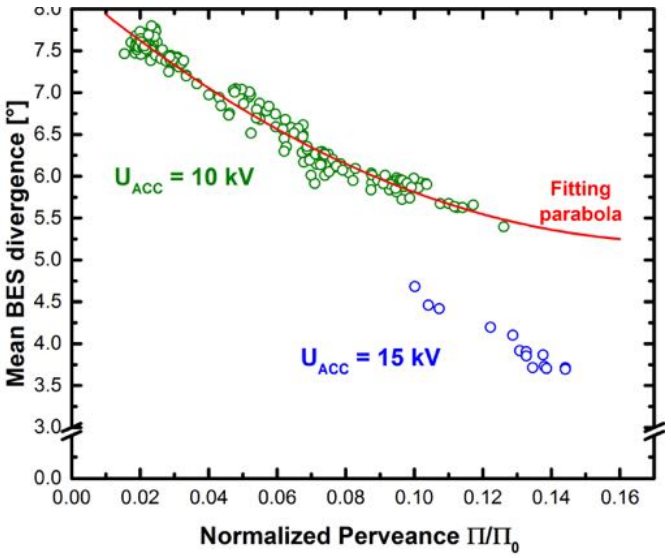

Figure 2.11. Beam divergence as a function of normalized perveance, measured with beam emission spectroscopy at BATMAN.

In Figure 2.11 the experimental beam divergence measured at BATMAN as a function of normalized perveance is shown; the divergence is estimated with spectroscopy (BES) approximately

0.7 m downstream of the last grid (GG). The experimental trend departs from the theoretical one presented above: the points can be fitted by a parabola rather than by a straight line.
The left branch of the parabola, where the divergence decreases with increasing perveance, is known as *underperveant region*; the right branch, here not present and seldom explored in BATMAN (since it corresponds to very high accelerated currents), is known as *overperveant region*. If the acceleration voltage U_{acc} is changed, the parabola shifts vertically: in Figure 2.11 a higher acceleration voltage helps the beam to focus and thereby the divergence is lower.

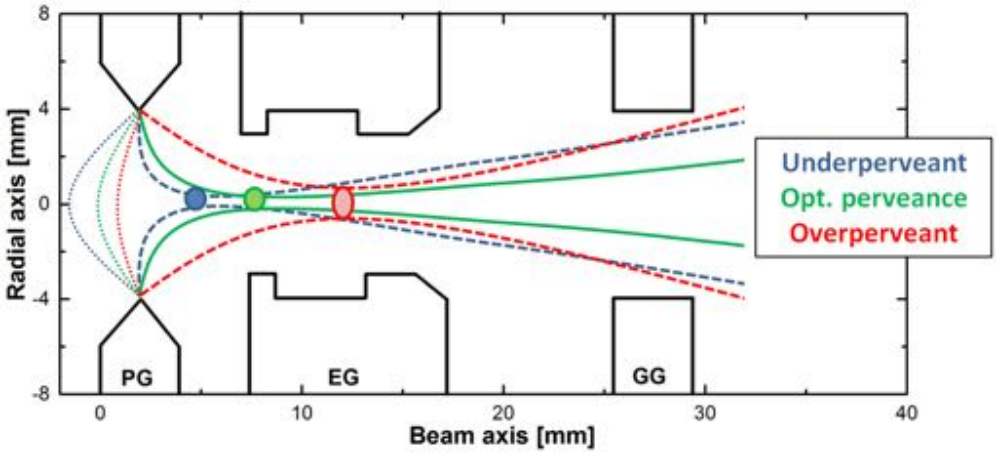

Figure 2.12. Schematic drawing of the beamlet shape in three situation: underperveant beamlet (blue), at the optimum of the perveance (green), overperveant beamlet (red).

If the beam is underperveant, the focus point of the first lens (the meniscus at the PG aperture) is located between the PG and the EG (Figure 2.12). As the perveance is increased, the curvature of the meniscus reduces and consequently the focus point moves towards the EG: the beam divergence gradually reduces, reaching its minimum when the focus is on the entrance of the EG (optimum of the perveance). Finally, if the perveance is further increased, the focus point shifts towards the GG and the beam divergence increases: the beam is overperveant (right branch of the divergence-to-perveance parabola). The dependence of the BES divergence for one of the vertical BES line-of-sight of ELISE test facility (at IPP-Garching) on the normalized perveance is shown in Figure 2.13; the minimum of the divergence, corresponding to the optimum of the perveance, is visible.

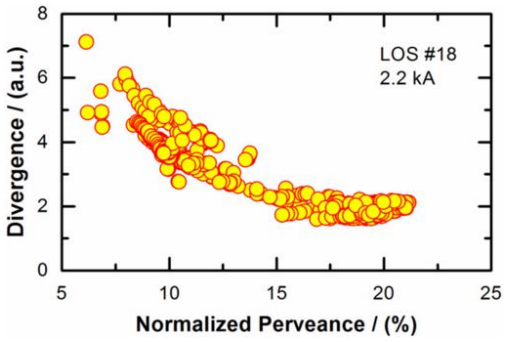

Figure 2.13. Line-of-sight averaged beamlet divergence as a function of normalized perveance, for one of the vertical BES of ELISE [12].

3 ITER prototype negative ion source: BATMAN test facility

The IPP (Max-Planck Institute fur Plasma Physics, Garching, Germany) RF driven cesiated negative hydrogen ion source is since 2007 the ITER NBI reference source [13]; the development of this source aims to meet the ITER-relevant ion source parameters (see Table 3.1). The work is carried out in different test facilities: one of them is the test bed "BATMAN" (BAvarian Test MAchine for Negative ions) at IPP.

Parameter	Deuterium	Hydrogen
Current extracted	57 A	66 A
Energy at the accelerator exit	1 MeV	870 keV
Power at the accelerator exit	40 MW	40 MW
Current accelerated	40 A	46 A
Extraction area	0.2 m^2	0.2 m^2
j_{acc}	200 A/m^2	230 A/m^2
j_{ex}	286 A/m^2	329 A/m^2
Power after neutralization	17 MW	17 MW
Source pressure	$\leq$0.3 Pa	$\leq$0.3 Pa
Electron content (j_e/j_{H^-})	$<$1	$<$0.5
Pulse length	3600 s	1000 s
Uniformity	$\pm$10%	$\pm$10%

Table 3.1. ITER requirements for its NBI negative ion source [14], [15].

3.1 The BATMAN test facility at IPP

The main aim of BATMAN is the optimization of the RF source with respect to the extracted current density in hydrogen and deuterium, operating at ***low pressure (0.3 Pa)*** and ***electron-to-ion ratio ($<$ 1)***, with a *small extraction area* ($<$ 0.01 m^2) and *short pulses* ($<$ 6 s); the extraction area of BATMAN is limited by the low pumping speed and capacity of the titanium sublimation pumps, while the short pulse length is limited by the characteristics of the high voltage power supply.

The BATMAN test facility is made up of three sections: (1) the *source region* (driver and expansion region), where the plasma is ignited and expands into the source body; (2) the *extraction and acceleration region*, where the ion current is accelerated up to 25 kV and the co-extracted electrons are deflected out of the beam; (3) the *drift region*, a vacuum chamber where the beam drifts and get analyzed by several diagnostics.

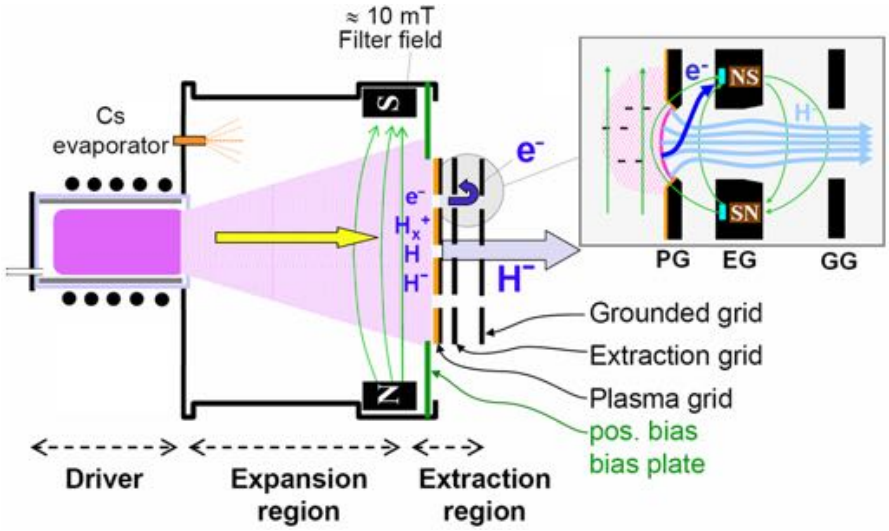

Figure 3.1. Schematic view of the IPP RF source in BATMAN.

3.1.1 The source region

RF driver The RF driver consists of a 150 mm long alumina cylinder with an inner diameter of 245 mm and a water-cooled RF coil connected to a 1 MHz oscillator; an internal edge-cooled copper Faraday screen protects the alumina cylinder from the plasma. In order to reduce the sputtering by the plasma, the plasma side of the Faraday screen is covered with a thin layer of tungsten. A starter filament together with a gas puff of a few 100 ms are required to ignite the plasma, which is then heated inductively by the RF coil.

Source body The source body consists of a 6 mm thick water-cooled stainless steel wall, and its inner side is covered with an electro-deposited 1 mm thick Cu layer for better heat distribution; the area of the source body section (0.32 x 0.59 m^2) is roughly one-eighth of the ITER source and its depth is 0.23 m. The source body is not equipped externally with any magnets for plasma confinement and in turn reduction of plasma losses at the source side walls. The magnetic filter field, described in the next paragraph, can be generated by internal fixed magnets or external movable magnets: the latter has the advantage of an easy change of the magnetic configuration, without moreover the necessity to open the source.

Filter field setups A magnetic filter field is located in the expansion region and, as previously explained, it filters out the hot electrons ($T_e > 2$ eV) from the plasma that flows towards the grids; several magnetic setups can be explored.
Figure 3.2 shows the mutually exclusive magnetic filter field setups in BATMAN: the *standard configuration*, with internal magnets embedded in the diagnostic flange, or the external and movable *magnetic frame*. The frame can be moved continuously along the source body from the diagnostic flange to the driver exit; it consists mainly of a support structure surrounding the source body with up to 2 x 4 magnets in CoSm (9 x 13 x 50 mm^3).

In Figure 3.3 the horizontal component of the magnetic filter field strength (B_x) in the center of the source for some configurations is shown. Each configuration is labeled with the distance of

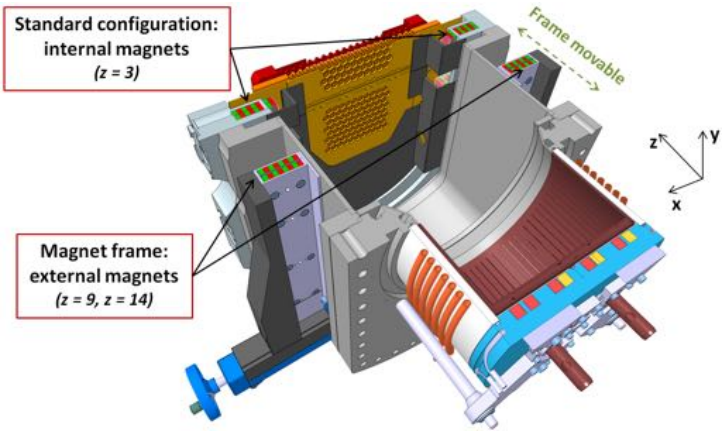

Figure 3.2. Section cut of the source (driver, source body and grids); also indicated are the magnets in the diagnostic flange (*standard configuration*) and in the magnet frame.([16]).

the magnetic field maximum from the plasma grid: for instance with the *standard configuration* the magnetic field is maximum at a distance of 3 cm from the PG, so this magnetic setup is known as $z = 3$. With the *magnet frame* (2 x 4 magnets embedded into the diagnostic flange), the explored configurations are the $z = 9$ (magnet frame in the nearest position to the PG) and $z = 14$: the position of maximum field shifts towards the source together with the frame, as expected.

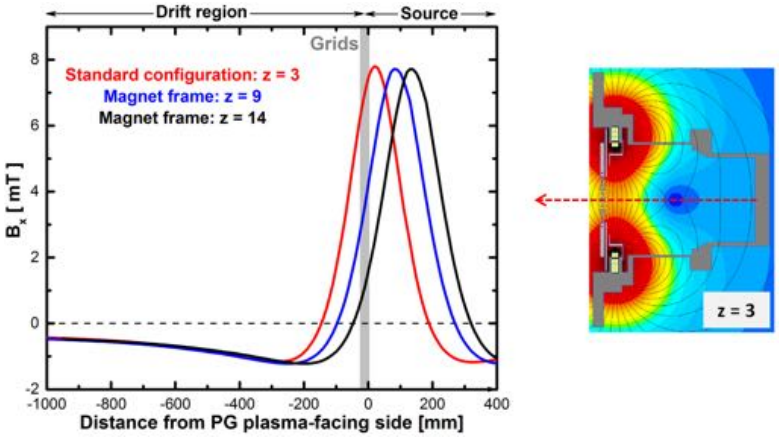

Figure 3.3. Horizontal magnetic filter field component in the center of the source: 'z' is the distance of the maximum B_x from the PG plasma-facing side.

The filter field causes drifts in the plasma - an $E \times B$ drift - leading to a top-bottom asymmetry of the plasma in front of the plasma grid. For the magnetic configurations of Figure 3.3 the drift is found to be upwards: consequently the magnetic configurations are labeled as $z = 3$ *UP*, $z = 9$ *UP* and finally $z = 14$ *UP*.
While the magnets in the diagnostic flange are fixed, the magnets in the external frame can be reversed, leading to a change of sign of the field and of the $E \times B$ drift direction (from upwards to downwards) : these setups are labeled as $z = 9$ *DOWN* and $z = 14$ *DOWN*.

Cs oven Caesium is delivered by an oven on the top of the source back-plate (see Figure 3.4): it is introduced into the source continuously, during the vacuum phase and the plasma pulses, and it can build up reservoirs on the walls.
The caesium is stored in glass capsules that are broken under vacuum by deforming a thin-walled steel tube enclosing the capsule; Cs atoms then move towards the oven nozzle and are dispensed into the source.
The evaporation rate is controlled by the temperature of five different locations of the oven (labeled as T1, T2, T3, T4 and T5 in Figure 3.4); this allows great accuracy in the regulation of the evaporation rate, which is typically around 10 mg/h and is measured by a surface ionization detector (SID) located near the nozzle [17].

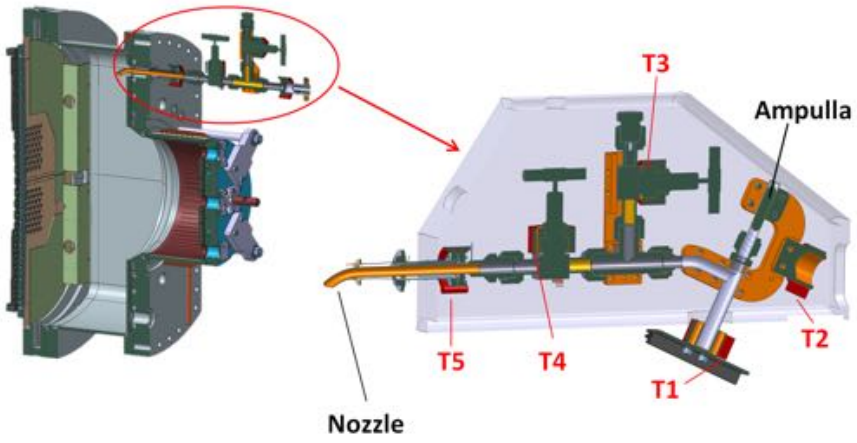

Figure 3.4. Section view of the Cs oven installed in BATMAN: it is possible to regulate the temperature of five locations independently.

3.1.2 The extraction and acceleration region

The typical voltage of the first gap - between the plasma grid and the extraction grid - is up to 10 kV (usually 5 kV), and up to 15 kV for the second gap - between the extraction grid and the grounded grid. The high voltage is delivered to the grids via a voltage divider with a resistance of about 1 $k\Omega$: this voltage divider is the main limit of the pulse length in BATMAN, with a maximum of about 5 s [18].

The current geometry of the grids is known as LAG (Large Area Grid) and it is shown in Figure 3.5. The LAG is made of two identical halves with 63 apertures each; the apertures are arranged in six rows with alternating 11 or 10 apertures with 11.6 mm distance in the horizontal and 11.9 mm in the vertical direction.

The ***plasma grid*** is made of 4 mm thick molybdenum and the holes have a chamfered shape, in order to increase the area for conversion of neutral and positive ions to negative ions (surface production). The grid faces directly the plasma and can be biased positively against the source body (+ 5 V): the *bias voltage* has been found to reduce the amount of co-extracted electrons. This biasing is provided by the addition of a so-called *bias plate* (shown in Figure 3.5), which in BATMAN is electrically connected to the source potential [18]. The current collected at the plasma grid is known as "*bias current*".

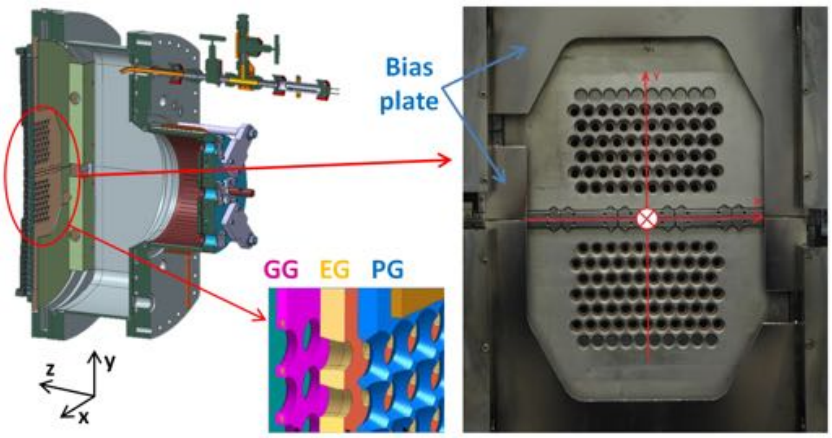

Figure 3.5. View of the LAG from the plasma side; is also shown a section of the three grids (grounded, extraction and plasma grid).

The ***extraction grid*** is made of copper and it is quite thick because it houses permanent magnets: such magnets create a "*deflection field*", which aims to deflect (horizontally) the co-extracted electrons on the EG, preventing them from being accelerated with the rest of the ion beam. Since the electrons deposit a large amount of power on the grid, this has to be actively cooled; to avoid overheating and melting of the grid, the power from co-extracted electrons cannot exceed a fixed value and this limits the total H^- extracted current.
The deflection field, mainly in the vertical (y) direction, is quite strong in the EG (see Figure 3.6) while quickly decays out of the grid (unlike the filter field, which penetrates also the drift region): the horizontal deviation induced to the ion beam is expected to be small .

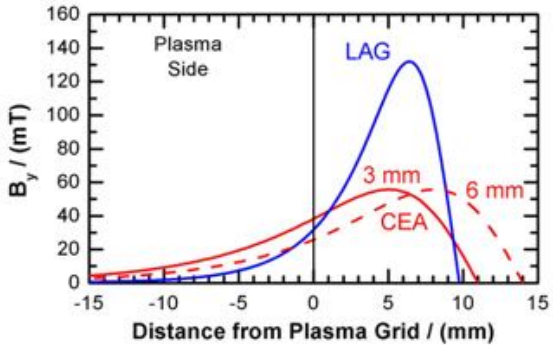

Figure 3.6. Calculated deflection field strength B_y relative to the PG position for three different extraction systems (the current is LAG, blue line) [19]

Finally, the two halves of the ***grounded grid*** are inclined ("tilted") by 0.9° for beam focusing; the total extraction area is 63 cm^2.

3.1.3 The drift region

Once extracted and accelerated, the negative ion beam enters the drift region (Figure 3.7); here it is observed by several diagnostics. A deep and detailed description of the beam diagnostics

available in BATMAN will be provided in the next chapter; they consist of:

- five vertically-aligned optical telescopes for Beam Emission Spectroscopy (**BES**), about 0.7 m downstream of the GG;
- a small diagnostic calorimeter, named ***mini-STRIKE*** , located 1 m after the grids;
- a bigger **copper calorimeter**, located near the end of the drift chamber, namely 1.7 m downstream of the GG.

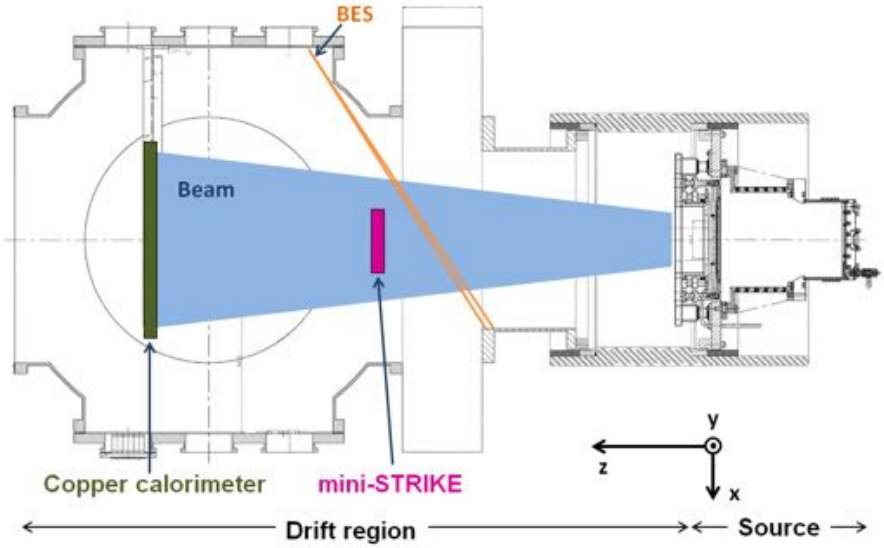

Figure 3.7. Location of the beam diagnostics in BATMAN (top view).

The current densities quoted in this work - the current density of extracted negative ions j_{ex} and of co-extracted electrons j_e - are electrically and individually measured:

- The ***electron current density***, j_e ($[mA/cm^2]$), is derived from the electrical current flowing onto the extraction grid (EG) [16]. Depending on the ion optics, some ions can hit the EG and some electrons can be accelerated with the beam; however, there is some evidence that the EG current matches the co-extracted current quite well [18].
- The ***electrically measured ion current density***, j_{ex} ($[mA/cm^2]$), is the sum of the current at the GG (I_{GG}) and the currents from the vacuum vessel (walls and all the diagnostics). This current is almost entirely (> 95 %) made up of negative ions [18]; hence, j_{ex} is a measurement of the negative ions that are extracted from the ion source.

3.2 Beam diagnostics in BATMAN

The three beam diagnostics available at BATMAN are shown in Figures 3.7 and 3.8: they consist of a vertical array of five telescopes for spectroscopy (Beam Emission Spectroscopy, BES), a diagnostic calorimeter made up of two Carbon-Fiber-Composite tiles (named *mini-STRIKE*) and finally a copper calorimeter.
A brief description for each diagnostic is here provided.

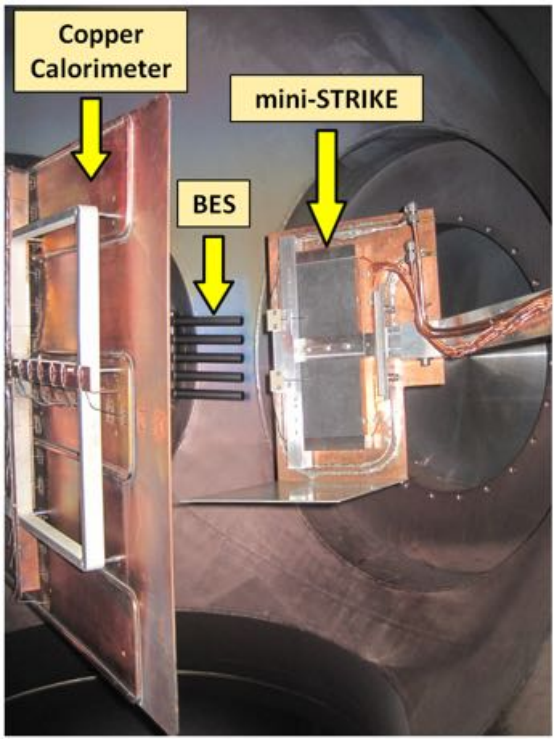

Figure 3.8. Beam diagnostics in BATMAN.

3.2.1 Beam Emission Spectroscopy (BES)

Beam emission spectroscopy, known also as H_α *emission spectroscopy*, is generally used to estimate the divergence and the stripping losses of the beam; this is performed with the evaluation of the light-spectrum produced by the interaction between the beam and the background gas in the drift region.
The emitted light is collected along five horizontal lines-of-sight (LOS), as shown in Figure 3.8; each telescope has a mean angle, with respect to the beam axis, of 52° and the vertical distance between two LOS is 40 mm. The light is then analyzed by a spectrometer in the wavelength range around the H_α line (the first line of the Balmer series for Hydrogen); it is important to point up that every information provided by BES on the beam is by definition a mean along the LOS of the telescope.
A typical BES spectrum is shown in Figure 3.9.

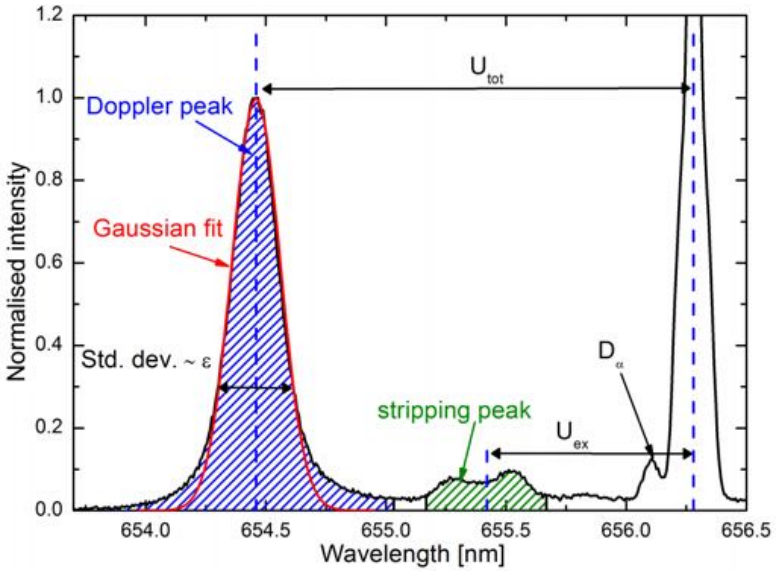

Figure 3.9. Typical BES spectrum, with three lines visible: the H_α unshifted line (on the right), the H_α Doppler-shifted line (on the left) and in the center a broad stripping peak.

Three peaks can be detected: the *unshifted H_α peak* (at about 656.3 nm), the *Doppler-shifted peak* (at about 654.5 nm) and finally, between them, the *stripping peak* .

Unshifted H_α It is the line emission caused by the dissociation and excitation of the background gas (the same gas of the plasma, usually H_2) induced by collisions with high-energy neutrals:

$$H_f^0 + H_2 \rightarrow H_f^0 + H_s^0(n=3) + H_s^0(n=3) \tag{3.1}$$

The indices s and f stand respectively for slow (background) and fast (beam) particles; the H_s^0 created are in the excited state $n = 3$ and spontaneously decade to the lower state $n = 2$. This leads to the emission of photons with wavelength $\lambda_0 = 656.3$ nm (first line of the Balmer series, H_α).

Doppler shifted H_α Some fully-accelerated beam particles H_f^- undergo the *electron detachment* process:

$$H_f^- + H_2 \rightarrow H_f^0(n=3) + H_2 + e^- \tag{3.2}$$

The fast neutral can thus decay from the excited state $n = 3$ to $n = 2$, emitting a photon at $\lambda_0 = 656.3$ nm. However, due to the motion of the neutral with respect to the laboratory frame, the emitted light is Doppler-shifted of $\Delta\lambda$:

$$\Delta\lambda = -\lambda_0 \frac{v}{c} cos\theta \tag{3.3}$$

where λ_0 is the proper wavelength (in the particle frame), θ is the viewing angle of the telescope with respect to the beam axis, v is the velocity of the particle and c the speed of light in vacuum [20].
The entity of the Doppler shift is proportional to the total energy of the particle ($\Delta\lambda \sim v \sim$

$\sqrt{U_{ex} + U_{acc}}$). Moreover, *line broadening* will occur as a result of a distribution of θ (natural divergence of the beam) and a distribution of the beam particles energy around the mean value $e \cdot (U_{ex} + U_{acc})$.

Stripping Part of the negative ions are neutralized between the PG and the GG via the reaction:

$$H_f^- + H_2 \rightarrow H_f^0 + H_2 + e^- \tag{3.4}$$

This process is called *stripping*; the fast neutrals produced are then excited by collisions with the background gas of the tank to the level $n = 3$ (as in Eq. 3.1) and subsequently relax to $n = 2$. The light emitted is partially Doppler-shifted: indeed the stripped particles do not have the full beam energy ($U_{ex} + U_{acc}$), but usually only the energy of the extraction gap ($v_{strip} \sim \sqrt{U_{ex}}$). The stripping peak is located very close to the shifted peak and partial overlap is present, as shown in Figure 3.9; its shape is not clear and thus a stable evaluation of its area, proportional to the amount of stripped particles, is an open issue.

BES spectra evaluation is a powerful method to estimate the line-integrated beam divergence and the stripping losses in the accelerator. The line-integrated beam divergence, namely the spread of beam particle trajectories around beam axis, can be measured starting with an estimate of the $(1/e) - width$ (*e-folding width*) of the Doppler-shifted line; then some corrections shall be applied in order to consider undesirable phenomena that affect the line width. A detailed description of the code for evaluating these spectra is provided in the next chapter.

3.2.2 mini-STRIKE calorimeter

As introduced in section 1.3, an ITER full-size plasma source of negative hydrogen ions is being built in Italy (Padua), named SPIDER ([21]). A section view of the experiment is shown in Figure 3.10: it consists mainly of a the negative ion source, a diagnostic calorimeter named **STRIKE** (Short-Time Retractable Instrumented Kalorimeter Experiment) to study the beam, and finally the ion dump, to absorb the beam.

The main aim of STRIKE is to characterize the beam in terms of beam *uniformity* and *divergence* during short operations (several seconds) [22] [23]. The instrumented calorimeter STRIKE is made of 16 1D Carbon-Fibre-Composite (CFC) tiles and it is able to intercept the whole ion beam; the footprint pattern will be observed from the rear side (to avoid plasma light) by infrared cameras.

A small-scale version of the such instrument, named ***mini-STRIKE*** , has been built by Consorzio RFX (Italy): *mini-STRIKE* consists of only 2 CFC tiles (120 x 90 x 20 mm^3) which are observed in the rear side (the side not exposed directly to the beam) by a thermal camera.
In the last few years *mini-STRIKE* has been used as a diagnostic in test facilities equipped with negative ion source: BATMAN test facility (IPP-Garching, Germany, [24] [25]) and the test stand of the negative-ion-driven neutral beams for the LHD stellarator (NIFS-Toki, Japan, [26]). This work studies, among other things, the most recent results obtained at BATMAN with *mini-STRIKE* (February 2014 - May 2015).

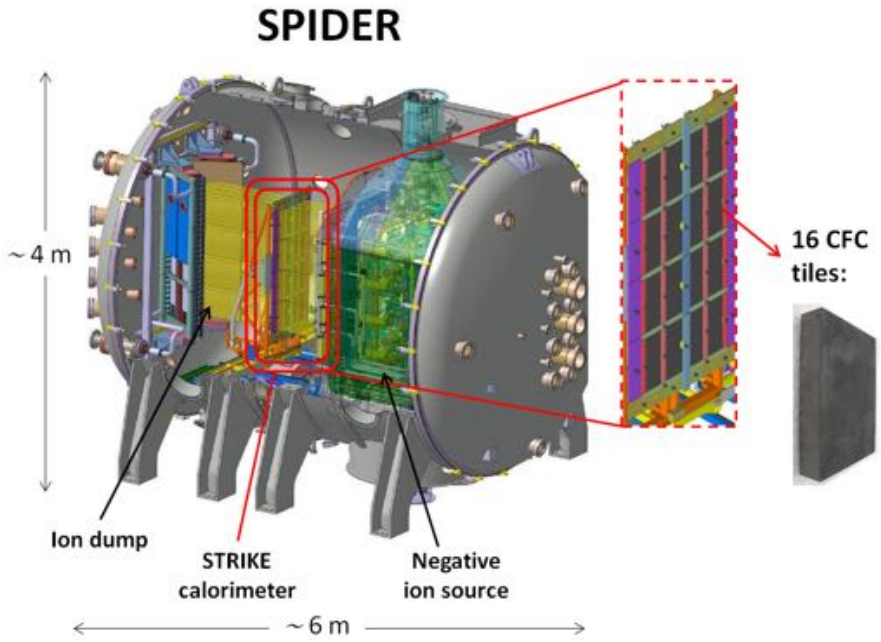

Figure 3.10. Cut-out view of SPIDER experiment; the STRIKE calorimeter is made of 16 CFC tiles as the one shown on the right.

Experimental setup at BATMAN

The experimental setup of *mini-STRIKE* at BATMAN is shown in Figure 3.11a.
The two CFC tiles are vertically arranged and housed in a dedicated frame which is connected to a supporting arm attached to the large BATMAN vacuum flange: both tiles are vertically exposed to the beam at a position 1 m downstream with respect to the extraction system, in order to avoid any carbon contamination of the source [24].

At that location, *the beamlets are expected to superimpose* (due to their divergence), leading to a quite flat ("bell-shaped") beam profile. To re-create a beamlet pattern on *mini-STRIKE* , a **copper mask** (actively cooled) with several holes is positioned just in front of the tiles: the beam is intercepted by the mask and consequently filtered, so that a beamlet pattern (SPIDER-like) hits the calorimeter.
The copper mask is 10 mm thick and one thermocouple monitors its temperature. The cooling-water flow is constant before and during beam extraction; the flow is measured together with the temperature of the input and output water, so that calorimetric measurement can be performed.
The current hole-geometry on the mask (since May 2014) is shown in Figure 3.11b: 24 holes with 7 mm diameter and 28 mm pitch each. In the very first experimental campaign of *mini-STRIKE* in BATMAN (autumn 2012), the pattern was much simpler: only 8 holes, with 10 mm diameter and 30 mm pitch each, arranged as a "C".

Figure 3.12 shows the view cone of the thermal camera that observes *mini-STRIKE* . During each pulse a IR-camera video is recorded; the start is externally triggered 3.2 s before the extraction of the beam and the sampling time is 20 s at 25 frames per second.

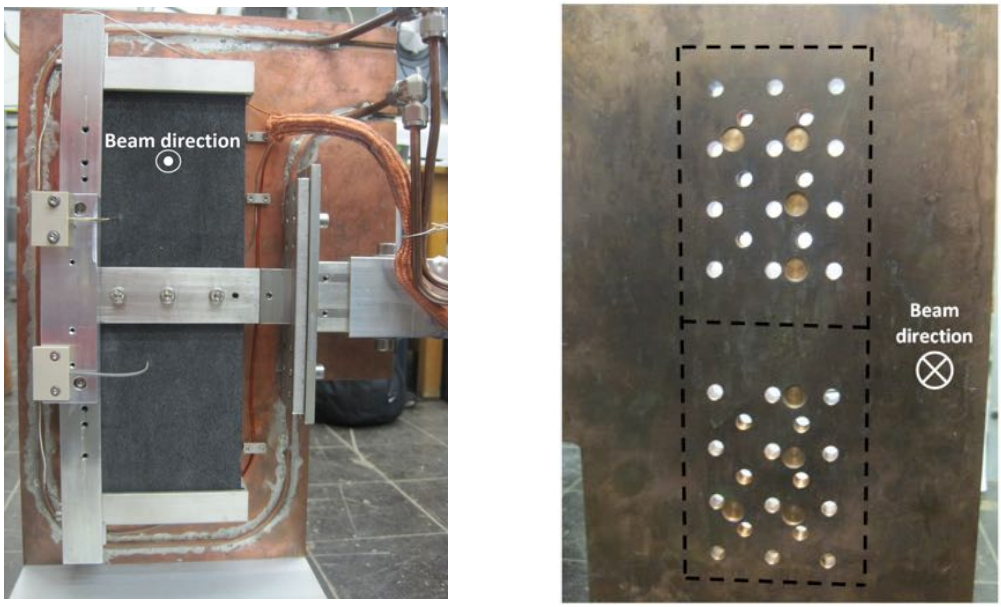

(a) (b)

Figure 3.11. *mini-STRIKE* setup at BATMAN test facility: rear side (a) and beam side (b) of the calorimeter.

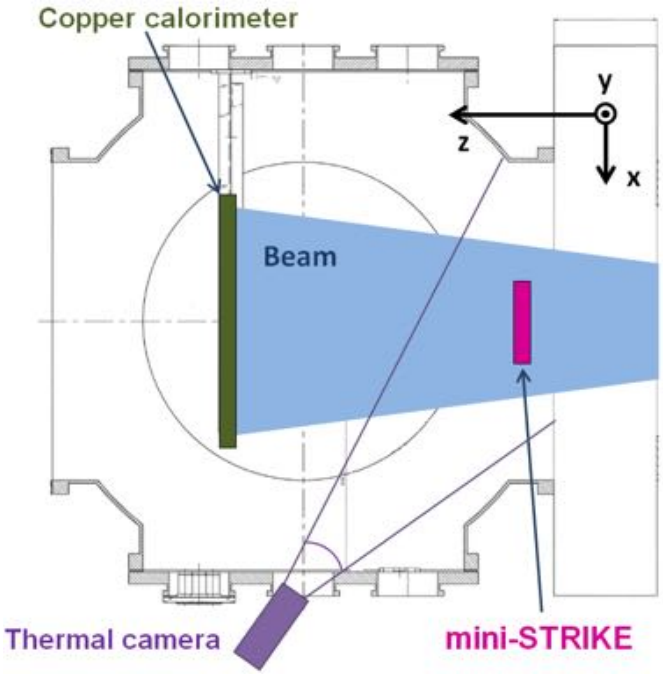

Figure 3.12. *mini-STRIKE* setup at BATMAN test facility: view-cone of the thermal camera which observes the rear side of the calorimeter (horizontal section of the vacuum chamber).

3.2.3 Copper calorimeter

The BATMAN test facility is equipped also with a copper calorimeter that intercepts the beam at the end of the vacuum vessel, approximately 1.7 m downstream of the grounded grid (see Figure 3.12) [18]. In Figure 3.13 the side of the calorimeter exposed directly to the beam is shown: it consists of a water-cooled copper panel ($60 \times 60\ cm^2$) with specially-designed thermally-isolated areas where thermocouples are embedded. 29 thermocouples are arranged as a *cross* and the distance between two consecutive thermocouples is 4 cm; during the beam phase, the temperature time trace of each thermocouple is recorded and then the temperature ΔT between the start and the end of the beam is computed. Since each thermocouple is thermally isolated from the rest of the calorimeter, the local beam power density can be calculated from the measured ΔT.

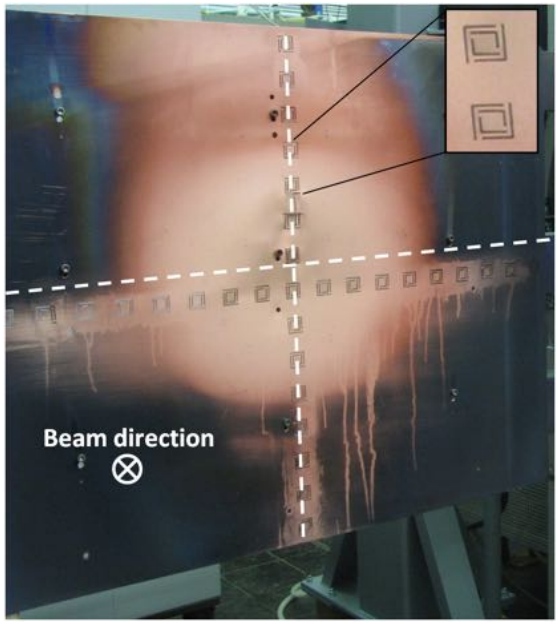

Figure 3.13. BATMAN copper calorimeter, side exposed directly to the beam. The dashed lines correspond to the central vertical and horizontal planes of BATMAN.

Typical vertical and horizontal power density profiles measured by the calorimeter are shown in Figures 3.14a and 3.14b: evaluation of the profiles, performed up to now with a simple Gaussian fitting, leads to an estimate of both the beam divergence at the calorimeter position and the total beam power impinging on the plate. The details of the fitting procedure are provided in the next chapter.

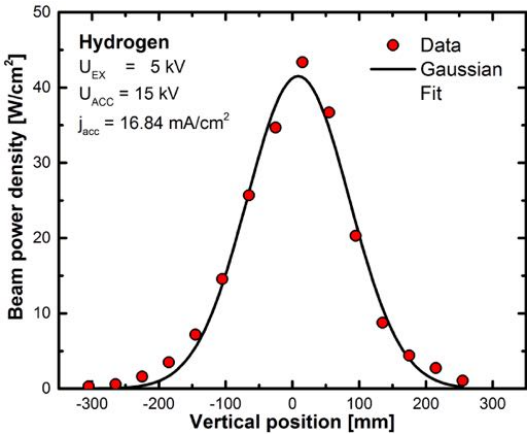

(a)

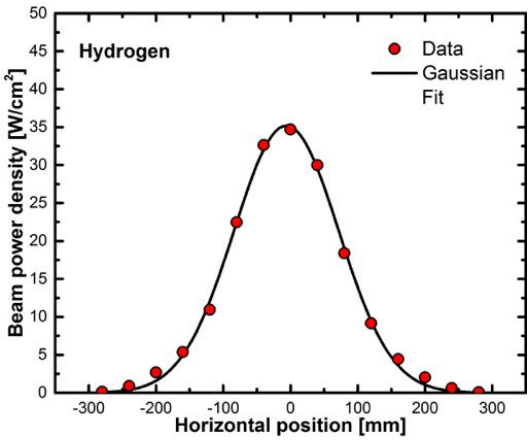

(b)

Figure 3.14. Typical beam profiles, along the vertical and horizontal direction, on the copper calorimeter; the magnetic setup is z = 9 UP. Another example can be found in [19]

4 Software development and introductory remarks

The first part of the chapter provides a detailed description of the analysis of beam diagnostics: the (1) *BES spectra*, the (2) *mini-STRIKE thermal videos* and finally (3) the thermocouples signals of the *copper calorimeter*. For diagnostics (1) and (3) a new code has been written, following the major steps of existing old programs; for diagnostic (2), several improvements and modifications were applied to more recent code (2014). A Graphical User Interface (GUI) was furthermore developed: its aim is to make the user able to handle and access easily the results of all the beam diagnostics simultaneously.
The second part of the chapter introduces some important remarks about data analysis, necessary to understand and interpret correctly the results reported in the following.

4.1 Software development for data analysis

4.1.1 Beam Emission Spectroscopy

Each BES spectrum collected at BATMAN is normally evaluated by a Fortran-code in real time, so that the main outcomes of the fits are available online right after the end of the beam. This code has however a disadvantage: the user is given only the final results of the fits and all the intermediate steps and interpolations are not accessible.
In order to better understand the functioning of the code and eventually to introduce some modifications and improvements, a software in IDL (Interactive Data Language) has been developed as part of the thesis work: it basically follows the major steps of an existing Fortran-code (the so-called ***standard evaluation*** of BES spectrum) but it permits a better control on the entire fitting procedure.
The code is organized in three steps: (1) background subtraction from the spectrum, (2) approximation of the H_α Doppler-shifted line (test of different fitting functions) and finally (3) derivation of beam divergence from the width of the line.

Step 1 - Background subtraction Early studies on the spectra from Beam Emission Spectroscopy ([20]) showed that, superimposed on spectra lines, there is a background which is by no means constant throughout the spectrum: it was found to be structured. The origin of the background is not fully clarified but it is likely the sum of several different phenomena, as for instance H_α-light reflection on the walls of the vacuum tank.
Hence, a simple polynomial fit is performed on the peak-free zones of the spectrum: the result is an almost flat profile, a straight line with negligible slope. Such line is then subtracted from the spectrum.

Step 2 - Approximation of the Doppler line: choice of the function The most natural choice to fit the Doppler-shifted bell-shaped line is a Gaussian.

However, early experimental results ([20]) showed that a Gaussian fit to the peak is much better if not a single Gaussian is used but a sum of a narrow Gaussian and a second one with half the intensity and width 2.5-times the width of the first one: this fact suggests that there is a beam *halo* created by the edge region of the extraction holes. Even if this way gives a better fit of the peak, it contains too much arbitrariness both in the fit and in the evaluation of fit results: indeed the beam divergence, in principle, could be evaluated either from the *e-folding* width of the narrower line or from a sort of "weighted sum" of the *e-folding* widths of both.

Another possible function for the Doppler-shifted peak approximation is the so-called *Pseudo-Voigt*, a linear combination between a Lorentzian $L(x)$ ([27]) and a Gaussian $G(x)$ ([28]):

$$V(x) = \eta \cdot L(x; x_0, \omega) + \beta \cdot G(x; x_0, \omega) \tag{4.1}$$

where the two functions are

$$L(x) = \frac{1}{\pi\omega} \frac{1}{1 + \left(\frac{x-x_0}{\omega}\right)^2} \tag{4.2}$$

and

$$G(x) = \sqrt{\frac{ln2}{\pi}} \frac{1}{\omega} \exp\left\{-ln2 \left(\frac{x - x_0}{\omega}\right)^2\right\} \tag{4.3}$$

while ω, x_0, η and β are free parameters.
As part of the thesis work, three different fitting alternatives have been explored, with the aim of finding the best choice:

1. **Gaussian fit with symmetric thresholds** (30% on the left and 30% on the right), that is considering solely the portion of the peak exceeding 30 % of its maximum, in order to avoid background fluctuations. This is the choice made in the official code used at IPP-BATMAN (known as *standard evaluation*). In some experimental situations the stripping peak, located on the right of the Doppler-shifted line, can contaminate the right-half of such a line: the 30% threshold can be not enough to exclude this contamination from the fitting range, which leads to a worsening of the fit quality (usually a *slight over-estimate of the line width*).
2. **Gaussian fit with asymmetric threshold** (30% on the left and 60% on the right) in order to exclude the zone of the peak contaminated by the stripping events.
3. **Pseudo-Voigt interpolation with asymmetric thresholds** (10% on the left and 30% on the right): this function is usually more precise than the Gaussian in interpolating the shifted peak. Moreover, the fit is very stable since the outcomes remain basically invariant if the thresholds for the fitting range are lowered or increased.

Figure 4.1 shows in detail the H_α shifted peak (measured by BES 4, the second telescope from the top) interpolated by a Gaussian with symmetric threshold (30% - 30%) and a Pseudo-Voigt. The two function are quite superimposed in the central region (above the 30% of the peak), while along the tails the Pseudo-Voigt approximation is better; these considerations are valid for the majority of the beam pulses.

In Figure 4.2 the BES divergence (for all the five LOS) from method (2) and (3) is plotted against the divergence from the *standard evaluation* (method 1); data refer to a typical day of

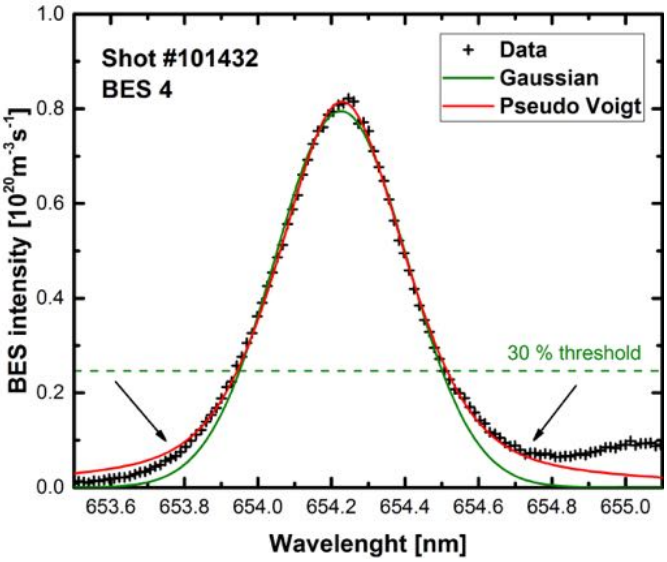

Figure 4.1. Comparison between two interpolating functions for the H_α Doppler-shifted peak: the Gaussian with symmetric thresholds 30% - 30% (green line) and the Pseudo-Voigt with thresholds 10% - 30% (red line).

Cs conditioning in Hydrogen. If the Gaussian with asymmetric thresholds or the Pseudo-Voigt is chosen as fitting function, the *divergence is slightly lower* than with the standard evaluation and *a better agreement with data exists* along the tails of the peak (Figure 4.1).
The difference in divergence between method (2) or (3) and method (1) is however very small and uniform along the range $[5 \div 8]^\circ$: the value from method (1) is basically compatible with those from (2) and (3) within the error bars. Furthermore no significant variations are found in the BES intensity if the fitting function is changed.

As a consequence of these observations, the **Gaussian with symmetric thresholds (30% - 30%) has been chosen** as the interpolating function for the H_α Doppler-shifted peak, in agreement with the IPP-BATMAN *standard evaluation*.

Step 3 - Derivation of the divergence from the line e-folding width As already set out in the previous chapter, the H_α line is Doppler shifted by a quantity $\Delta\lambda$ [20]:

$$\Delta\lambda = -\lambda_0 \frac{v}{c} \cos\theta$$

where λ_0 is the wavelength of the radiation in the frame of the emitter particle (energetic H^0) moving with speed v with respect to the laboratory frame, while θ stands for the viewing angle of the BES telescope with respect to the beam axis. Both v and θ have a distribution and let be v_0 and θ_0 the mean values; they correspond to the mean Doppler-shift $\Delta\lambda_0$:

$$\Delta\lambda_0 = -\lambda_0 \frac{v_0}{c} \cos\theta_0$$

.The differential deviations $dv_\parallel$ and $dv_\perp = v_0 d\theta$ will thus result into a deviation from the mean shift of ([20])

$$\delta \equiv d(\Delta\lambda) = \Delta\lambda_0 \left(\frac{dv_\parallel}{v_0} + \tan\theta_0 d\theta \right) \tag{4.4}$$

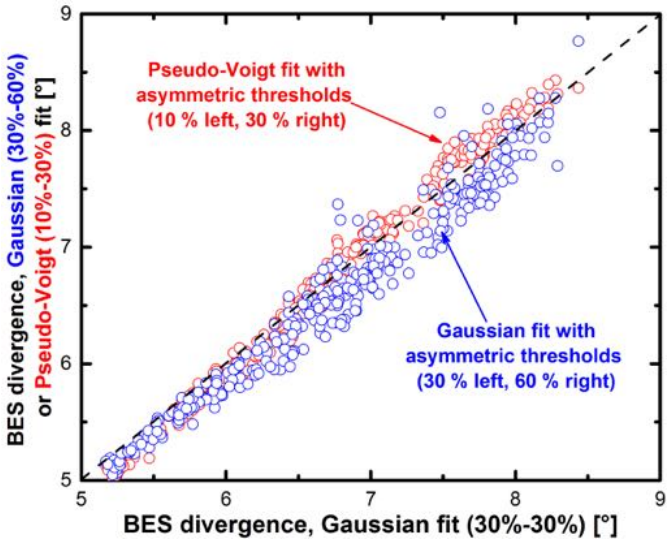

Figure 4.2. BES divergence (LOS 1 to 5) from Pseudo-Voigt fit (red points) or Gaussian fit with asymmetric thresholds (blue points), plotted against the divergence obtained with the *standard evaluation*. Data refer to a Cs-conditioning day in Hydrogen.

which can be simplified considering all the particles at the same energy:

$$\delta = \Delta\lambda_0 \tan\theta_0 d\theta \equiv \delta_{app} \tag{4.5}$$

The quantity δ_{app} is known as ***apparent e-folding*-width of the Doppler-shifted H_α line**. The experimental *e-folding*-width of the line, δ_{fit}, is always greater than δ_{app}: indeed other effects induce a further *broadening* of the line, and they are schematized in Figure 4.3.

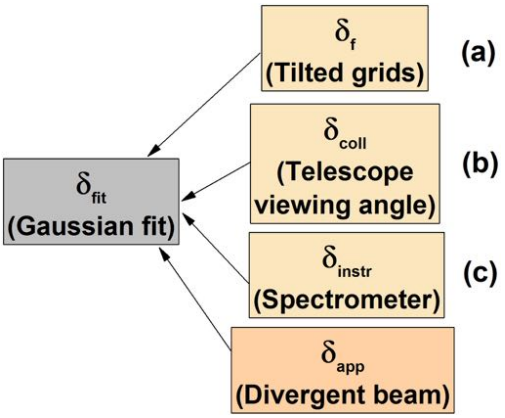

Figure 4.3. Contributions to the *e-folding*-width of the Doppler-shifted H_α line.

These contributions are caused (a) by the fact that the two halves of the GG are tilted (δ_f), (b) by the light-collection system (δ_{coll}) and finally (c) by the spectrometer itself (δ_{instr}). Consequently

the experimental width is the convolution:

$$\delta_{fit} = \sqrt{\delta_f^2 + \delta_{coll}^2 + \delta_{instr}^2 + \delta_{app}^2} \tag{4.6}$$

The next paragraphs provide a brief description of each of these effects.

(a) Line broadening by beam focusing The LAG (see Figure 3.5) can be roughly approximated as a circular source with diameter $2R$ and focal length f; then the half-angle of the beam becomes $\epsilon_f = R/f$ (see Figure 4.4). If θ_0 is the angle between the viewing direction and the beam axis, then the viewing angles will spread from $\theta_0 - \epsilon_f$ to $\theta_0 + \epsilon_f$. The correspondent spread of the Doppler shifted line can be easily computed ([11]) as

$$\delta_f = \epsilon_f \Delta\lambda_0 \tan\theta_0 \tag{4.7}$$

The aforementioned focusing is, in BATMAN, provided by using tilted grids; the tilt angle is by definition the total angle of the beam (namely $2\epsilon_f$) and its value is 1.75°. A simple conceptual scheme is shown in Figure 4.4.

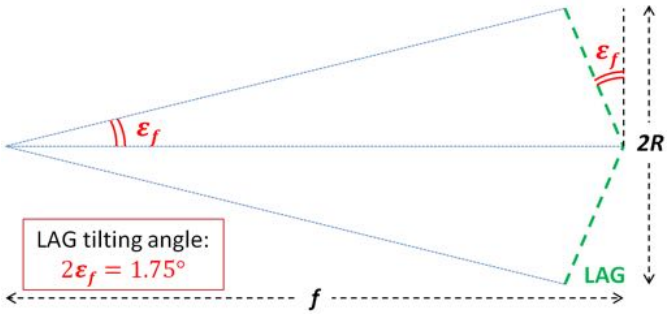

Figure 4.4. Conceptual scheme of the line broadening due to beam focussing (tilted grids).

(b) Line broadening by the light-collection system Any light-collecting system needs a finite cross-section and angular range to work: thereby the viewing angle has an unavoidable spread. Let ϵ_{coll} be the angle in the plane of the beam axis and viewing axis (horizontal plane): this will lead to a line spread of

$$\delta_{coll} = \epsilon_{coll} \Delta\lambda_0 \tan\theta_0 \tag{4.8}$$

For the BES telescopes installed in BATMAN, the exact value is $\epsilon_{coll} = 0.22$ rad.

(c) Line broadening by the spectrometer A line broadening is caused finally by the instrument itself; the spectrometer used in BATMAN, an *Andor* (Oxford Instruments), introduces a line broadening of $\delta_{instr} = 0.126$ nm.

Finally, the apparent width δ_{app} is computed using Eq. 4.6 and then the beam divergence $d\theta$ is calculated with Eq.4.5.

4.1.2 mini-STRIKE

An automatic analysis procedure has been set up to analyze the videos recorded by the thermal camera that watches *mini-STRIKE* : the code is written in IDL (Interactive Data Language) and it has been amply improved during the thesis work. In the following, the features of the temperature 2D-profile on the masked tiles will be improperly referred to as the "beam pattern". Each thermal video is decomposed in 500 frames (FPF images), which constitute the input of the code: the algorithm performs a complete parametrization of the beam as it is seen in the rear side of the tiles, and a list of significant "beam parameters" is provided as output.

A short overview of the most important procedure steps is here set out; a more detailed description can be found in [29].

- **Step 1 - Background subtraction and perspective correction** Firstly the program estimates the background image by averaging the first 25 frames of the video (when no beam is still extracted from the source): the background is then subtracted from all the remaining frames.
  It has been observed that when the beam starts, the tile temperature increase - on the front side - can be seen thanks to a reflection on the rear side of the copper mask (lower part of the thermal image): this frame is identified as the starting frame. The end of the beam takes place usually 4 s after its start; on the third frame before the end of the beam all the interpolations are performed. Figure 4.5a shows a typical thermal image used as input to the program.
  Moreover a perspective correction is applied to the image because of the viewing angle of the thermal camera.

- **Step 2 - Approximation of the 2D thermal pattern** The fitting phase is articulated in three steps.
  (1) To begin with, on each of the 36 beamlets a 2D-Gaussian fit is performed: the 2D-location of the 36 centers is the input of the next step ((x_i, y_i) with $i = 1...36$).
  (2) A user-defined function, the superimposition of 36 Mod-Hubbert functions (Eq. 4.9), is used to approximate the entire thermal pattern of both tiles simultaneously.

$$f(x,y) = \sum_{i=1}^{36} a_i \cdot \left[cosh\left(\sqrt{\left[\gamma \cdot (x - x_{c,i})\right]^2 + \left[\gamma \cdot (y - y_{c,i})\right]^2} \right) \right]^{-q} \tag{4.9}$$

  Both γ and q are related to the width of the single beamlet and they are supposed to be the same for all the beamlets: indeed the 36 holes of the mask are identical and the thermal properties of the tiles are spatially homogeneous [29].

  (3) Finally an asymmetric function (Eq 4.13) is adopted to interpolate the 36 amplitudes $a_1...a_{36}$: it is simply the product of a *parabola* in the horizontal direction (Eq. 4.10) and a *skewed Gaussian* in the vertical direction (Eq. 4.11, see [29]), namely a Gaussian with non-zero skewness.

$$p(y) = ay^2 + by + c \tag{4.10}$$

$$g(x) = \exp\left\{ -\frac{1}{2} \left(\frac{x - x_0}{\omega} \right)^2 \right\} \cdot \left[1 + erf\left(\alpha \frac{x - x_0}{\sqrt{2}\omega} \right) \right] \tag{4.11}$$

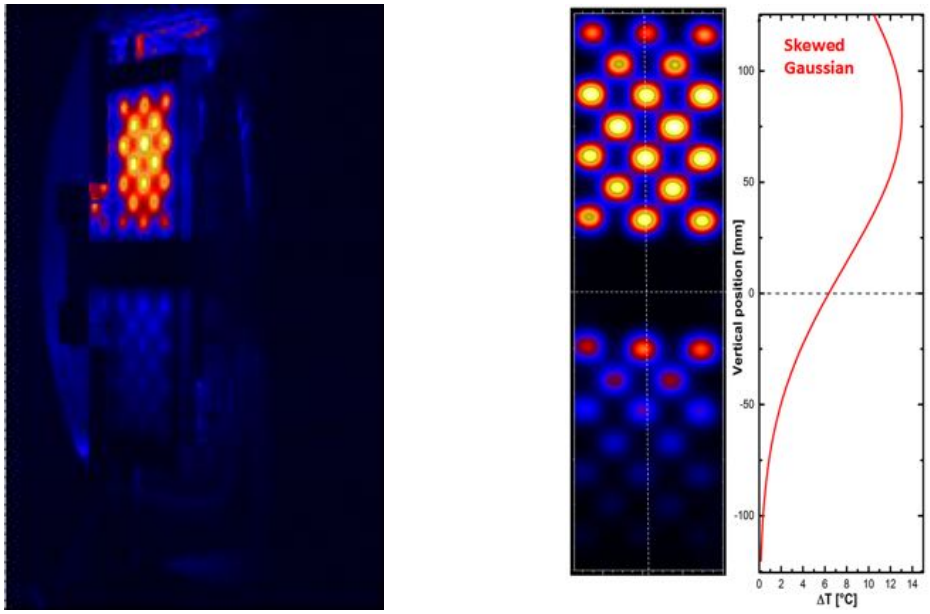

(a) (b)

Figure 4.5. (a): Thermal image of *mini-STRIKE* , input of the code. (b): Parametrization of the beam behind the tiles (output of the code); the vertical section of the beam fitting function is also shown.

$$erf(x) = \frac{2}{\sqrt{\pi}} \int_0^x e^{-t^2} dt \tag{4.12}$$

$$h(x, y) = g(x) \cdot p(y) \tag{4.13}$$

This choice was driven by the empirical observation that the vertical profile of the beam was slightly asymmetric ([29]); the observation is confirmed by the most recent results contained in this dissertation. Such function has been chosen because it describes quite well the 2D temperature map of the beam on the rear side of the tiles; it does not have a specific theoretical meaning.

Results retrieval: development of a GUI software

A Graphical User Interface (GUI), in IDL, has been developed in order to access easily and quickly the huge amount of results of beam diagnostics, in particular of *mini-STRIKE* ; more than a thousand beam pulses have been analyzed.

Figure 4.6 shows the main interface of the GUI software.
The user must select an experimental scan and two parameters, an x-parameter and a y-parameter; then the software automatically searches for the database, retrieves data and finally plots the results in a graphic window. Typical quantities plotted as y-parameters are *source parameters* (the source pressure, the acceleration and extraction voltages, the bias current, etc...), *calorimetric parameters* (from *mini-STRIKE* , like the vertical position of the maximum heat-flux, or from the copper calorimeter, like the beam divergence or the vertical position of the

beam center) and *outcomes from beam spectroscopy (BES)* (like beam divergence and intensity along each LOS).

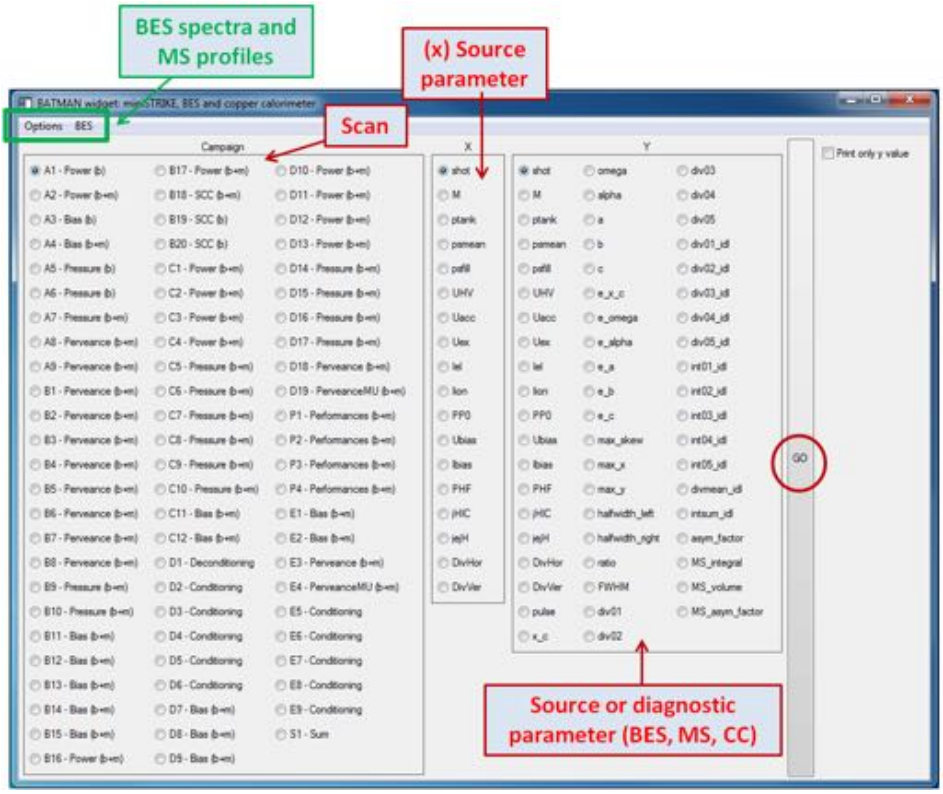

Figure 4.6. Main interface of the GUI software.

The codes for data analysis of Beam Emission Spectroscopy and the Copper Calorimeter were embedded in the GUI software. Hence, the user has full access (1) to all the BES spectra (raw data, fitting functions, results) for all the LOS, (2) to vertical and horizontal beam profiles at *mini-STRIKE* (beamlets) and finally (3) to the data of the copper calorimeter thermocouples, namely vertical and horizontal beam profiles with fitting functions and outcomes (see Figure 4.7).

Thermocouples on mini-STRIKE copper mask

The *mini-STRIKE* calorimeter is equipped with five thermocouples: two are installed on the tiles (one for each tile), one on the copper mask, while two monitor the inlet and outlet water of the cooling system. The time-trace recorded from the water outlet thermocouple is shown in Figure 4.8, with a detail of one beam pulse: it is clear that as long as the beam is extracted the water temperature goes up quickly, while when the beam is off it decreases slowly, going back to the initial value before the start of the next beam pulse.

It may be noted that at the beginning of each experimental day the copper-mask cooling-water flux was regulated so that the coolant could remove from the mask all the energy deposited by the beam before the start of the successive beam: in this way the whole beam energy can be

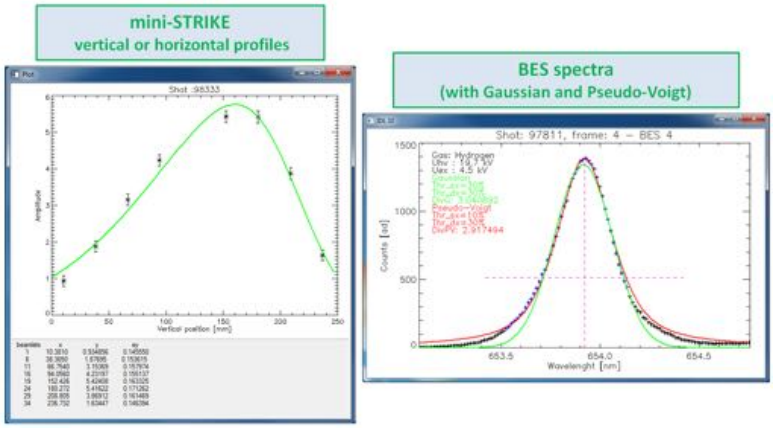

Figure 4.7. GUI secondary windows, with *mini-STRIKE* 1D-profiles and BES spectra.

reconstructed from the temperature time-trace with calorimetric calculations.
In order to study some basic correlations between the ΔT of the outlet cooling water and the beam properties, namely the beam current or divergence, an IDL software has been developed: it takes as input the time-trace of the thermocouple and gives as output the difference in temperature ΔT between the begin and the end of each steep rise. The results of this study are however not presented in this dissertation since they are not relevant to the topic of the dissertation, namely beam property characterization.

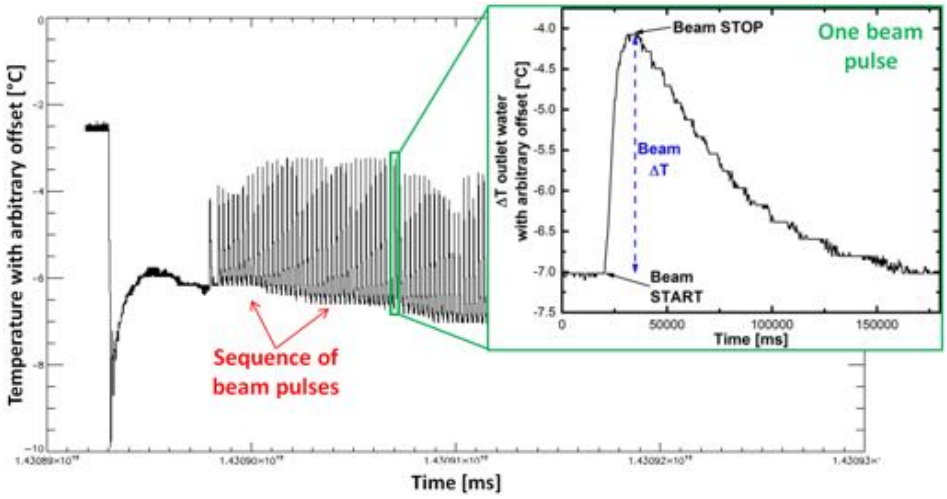

Figure 4.8. Temperature time-trace for the cooling water coming from the *mini-STRIKE* copper mask; a detail of a single beam pulse is also shown.

4.1.3 Copper calorimeter

The analysis of the copper calorimeter thermocouple signals is in BATMAN performed by a Fortran code. A similar software in IDL has been developed, with the aim of understanding better and more deeply all the steps of the code and in case introduce some improvements.

The program takes as input the temperature increase ΔT due to the beam measured by each of the 29 thermocouples: Figures 3.14a and 3.14b show such values (red points), which are simply interpolated with two 1-D Gaussian. Finally, from the temperature increase one can evaluate the power density (W/m^2) for each thermocouple.
The relation between the width of each Gaussian (the standard deviation, σ) and the divergence of the beam is not straightforward, since the beam is the superimposition of many beamlets; the divergence of the beam is estimated by a comparison of the measured beam profile with a *geometrical beam model* using the ***IPP-DENSB code***. This code assumes that each beamlet emitted by the grounded grid has a Gaussian profile where the width of the Gaussian is given by the assumed beamlet divergence: the calibration relation between the *beam divergence* (namely of each beamlet) at the grounded grid (GG) and the *beam standard deviation* σ at the copper calorimeter is plotted in Figure 4.9.
A much simpler but wrong approach would be to consider the divergence as the angle under which the *e-folding half-width* of the beam profile at the calorimeter is seen from the GG (red dashed line in Figure 4.9); moreover this choice would lead to a general overestimation of the actual divergence.

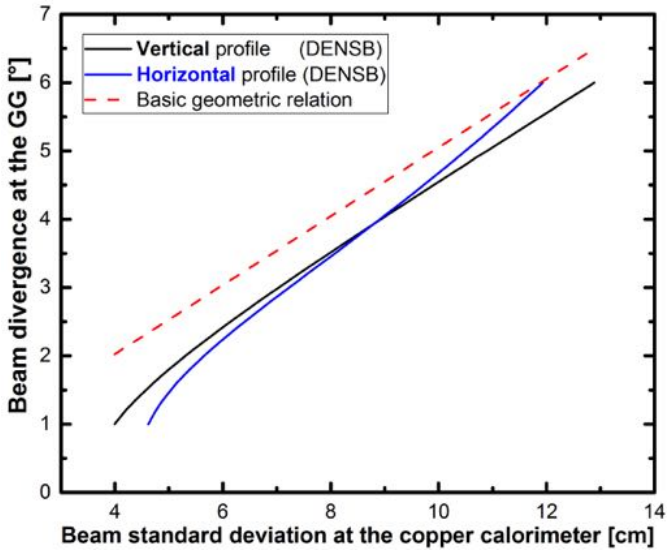

Figure 4.9. Calibration between the beam standard deviation at the copper calorimeter and the corresponding beam divergence at the GG (from IPP-DENSB code).

In the original Fortran code a 2D-Gaussian fit, instead of two 1D-Gaussian interpolations, was performed; however, with the latter choice the residuals from experimental data are found to be lower and the data-fit agreement is in general much better. Anyway the fit results obtained with the two methods, namely the vertical and horizontal standard deviations, positions of the center, amplitudes etc.. are usually compatible within the error bars.

4.1.4 Simulation activity

A simulation code to reproduce beam propagation through the drift vessel has been developed in the past at Consorzio RFX. The concept of the code is simple: a bi-dimensional array of accelerated beamlets, whose geometry is determined by the geometry of the grid apertures, with possibly *inhomogeneous power and angular divergence*, is propagated starting from the grounded grid (GG). The heat flux pattern impinging on a plane surface (a calorimeter), positioned vertically with respect to the horizontal, is provided as output.
This code has been run with the LAG grid geometry of BATMAN and with the copper mask as calorimeter.

The grid geometry at IPP BATMAN (Large Area Grid) consists of two identical grid halves with 63 apertures each, as already explained: the apertures are arranged in a total of 12 horizontal rows, with alternatively 10 and 11 holes each (see Figure 3.5). The copper mask is modeled simply as a rectangular plane surface, parallel to the GG and located 1 m downstream it.

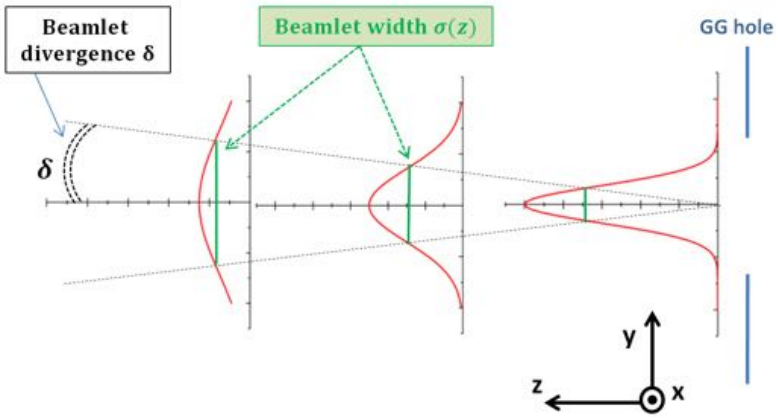

Figure 4.10. Concept of RFX code for beam propagation.

Figure 4.10 shows a concept of the code working principle.
The beamlet extracted from a grid hole is modeled as a bi-dimensional Gaussian of power density $q(x, y, z)$ (Eq. 4.14), with identical horizontal and vertical widths $\sigma_u = \sigma_v = \sigma$: the beamlet power and divergence δ (angular semi-aperture) are not uniform along the grid, but a vertical profile for both is provided as input to the code.

$$q\,(x, y, z) = q_c(y, z) \cdot exp\left[-\frac{(x - x_c)^2}{2\sigma(y, z)^2} - \frac{(y - y_c)^2}{2\sigma(y, z)^2}\right] \tag{4.14}$$

$$q_c(y, z) = \frac{q_0(y)}{2\pi\sigma^2(y, z)} \tag{4.15}$$

Each beamlet is thereby propagated into the drift region. Its width increases linearly with space (Eq. 4.16) since the beam is assumed to be space charge compensated; this assumption is only in first approximation true for a real beam.

$$\sigma(y, z) = \sigma_0 + z \cdot tg(\delta(y)) \tag{4.16}$$

As a consequence, the beamlet power density profile is smoothed and it broadens during the propagation (see Figure 4.10 and Eq.4.16).
Finally, a vertical deflection angle (α_{FF}) can be set for the whole beam, in order to roughly reproduce the vertical deflection caused by the magnetic filter field.

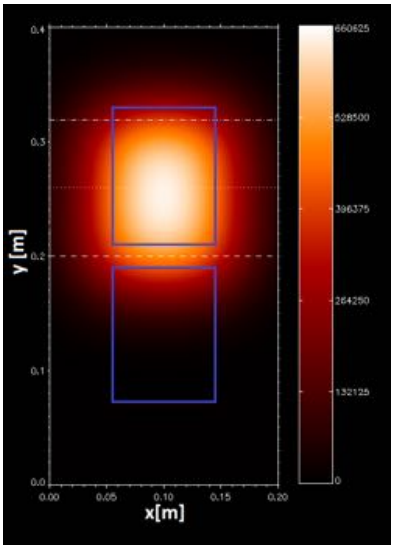

Figure 4.11. Typical 2D-pattern of the beam power flux [W/m^2] at the copper mask of *mini-STRIKE* .

The output of the code is the beam power density 2D-pattern impinging on the copper mask at a given distance from the grid, due to the superimposition of all the 126 beamlets. Figure 4.11 shows a typical power flux pattern provided by the code, looking in the beam direction: the blue lines indicate the edges of the two CFC tiles, located behind the copper mask. For this example, the beam is provided with an inclination of $\alpha_{FF} = 3.0°$ and both divergence and power profiles are uniform: the beam divergence (namely the divergence of the beamlets) is 3.6° and the power is 100 Watt for all the grid apertures.

Sensitivity tests In order to check the reliability of the code and the influence of each parameter (deviation angle, divergence and power profiles,...) on the final beam (vertical) profile, several sensitivity tests have been performed. A vertical inhomogeneity in the divergence or beamlet power has been usually introduced: this inhomogeneity is quantified in percentage. When the inhomogeneity is for example 20%, then the divergence of the *top row* of beamlets is 20% bigger than the value at the center of the grid (at y=0) and similarly the divergence of the *bottom row* of beamlets is 20% lower than that; the opposite happens with a -20% inhomogeneity.

Figures 4.12 and 4.13 show the results of the sensitivity tests.
The vertical position of maximum heat flux (the "beam center", as it will be explained in the following) has a deviation from the center of the calorimeter proportional to the deviation angle α_{FF}, as expected; the shift is upwards if α_{FF} is positive, downwards if α_{FF} is negative (see Figure 4.12a). In the case that no inhomogeneities are introduced and the beamlet divergence is gradually lowered, for values below 3.0° the beamlets are so well-focused that the contributions of the two half grids are distinguishable (two peaks): indeed the beamlets of the lower grid and those of the upper grid get only marginally superimposed (Figure 4.12b).
When the divergence inhomogeneity is increased, the beam center moves towards the region of

lower divergence: upwards, if the inhomogeneity is more and more negative, or downwards, if it is more and more positive. Consequently, the vertical beam profile becomes very steep on one side (Figure 4.13b): the same tendency happens whether the power inhomogeneity is changed, but the impact on the beam vertical shape is less significant (Figure 4.13a).

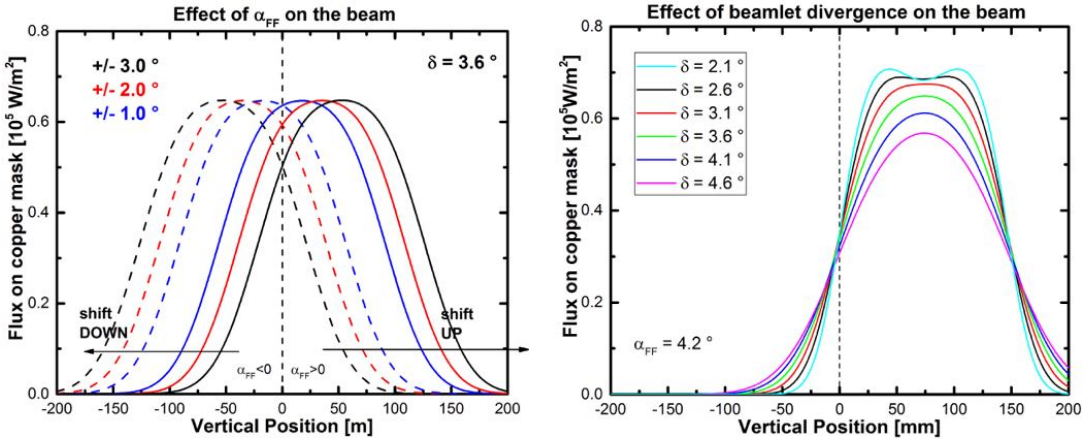

(a) (b)

Figure 4.12. Sensitivity tests on the RFX code for beam propagation: study of the effect of α (left) and beamlet divergence (right).

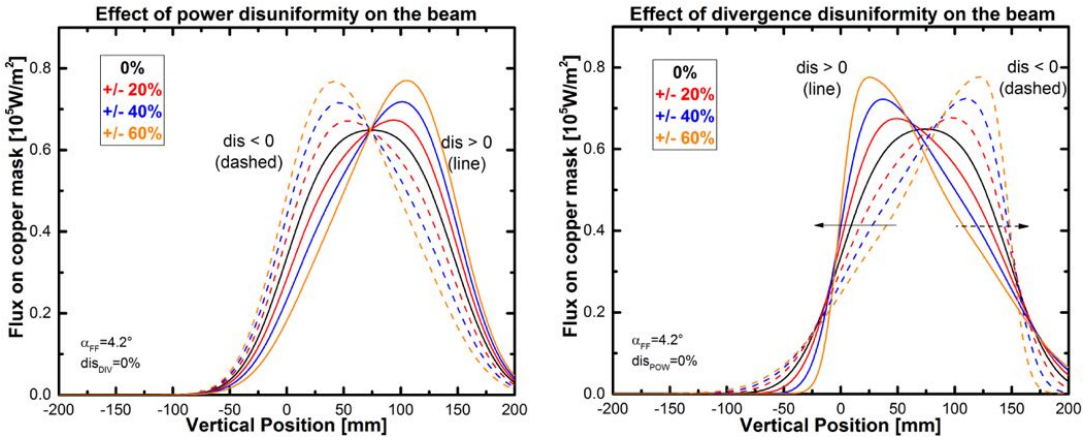

(a) (b)

Figure 4.13. Sensitivity tests on the RFX code for beam propagation: study of the effect of beamlet power disuniformity (left) and divergence disuniformity (right).

Finally it is important to point out that, from a physical point of view, the local variation of the beamlet power is always accompanied by a variation of the beamlet divergence: indeed the power and divergence profiles at the GG are strongly correlated due to the Child-Langmuir law (see section 2.4.2).

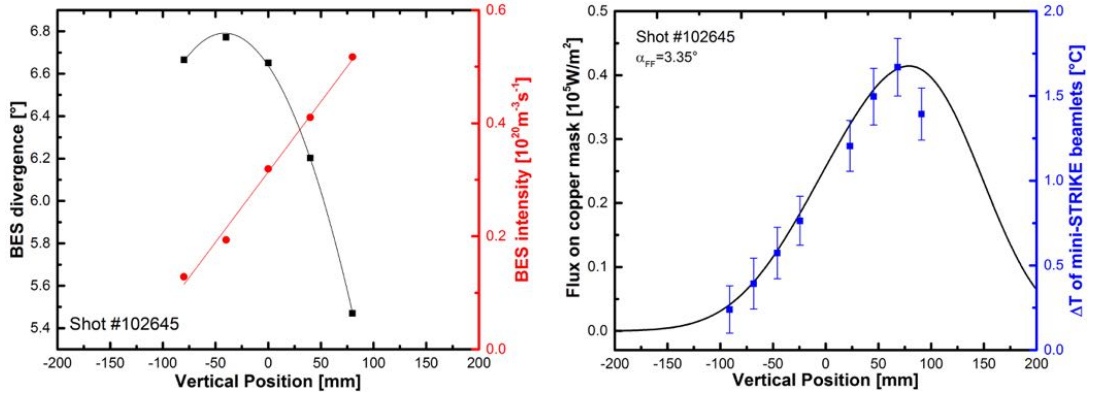

(a) (b)

Figure 4.14. Left: BES divergence and intensity vertical profiles, interpolated by simple functions. Right: comparison between the beam power flux vertical profile on the copper calorimeter (RFX code) and the beam ΔT sampled by *mini-STRIKE* .

Reproduction of mini-STRIKE profile The *mini-STRIKE* calorimeter provides a *vertical profile of the beam* ΔT on the *rear side of the CFC tiles*, while the RFX code gives a *vertical profile of the beam power flux* (W/m^2) on the *copper mask*: these two profiles are linked by the transfer function from the front to the real side of the tiles. Since the thermal conductivity of the tiles in the longitudinal direction is much higher than in the transversal direction, it may be reasonably assumed that the alterations in the profile shape introduced by the transfer function are not large; thereby, within the error bars and only in first approximation, these two profiles are assumed to be proportional and to have the same shape.
If the proper inputs are given to the code (power and divergence inhomogeneities, deflection angle), it is in principle possible to reproduce the shape of the profile of *mini-STRIKE* ; to test such statement, a beam pulse was chosen (#102645, Hydrogen)

The vertical profiles of BES intensity and BES divergence are taken as a rough estimate, respectively, of the power and divergence vertical profiles at the grounded grid. As it will be explained in the following, the light intensity collected by a BES telescope ($[m^{-3}s^{-1}]$) is proportional to the beam current density along that LOS ($[mA/cm^2]$) and thus to the power of the beamlets at the GG. Similarly, if the beam is space-charge-compensated the divergence measured at the BES is almost equal to that at the GG.
The BES intensities are interpolated by a straight line (see Figure 4.14a): a straight line with the same slope and which equals 100 Watt at the center of the grids (y=0) is the beamlet-power input profile. The BES divergences are approximated by a parabola, which is the beamlet-divergence input profile (Figure 4.14a).

Figure 4.14b shows the expected profile of the beam on the copper mask (heat flux), compared with the experimental ΔT measurement by *mini-STRIKE* : the agreement in the shape is quite good. It is worth to notice that the proper deflection angle α_{FF} has been set *a posteriori* (3.35°), since it is not possible to predict in an easy way its value; this parameter does not affect the shape of the beam but gives only a rigid vertical shift.
Furthermore, as it will be shown in the next chapter, the position of the beam center depends on several factors, like the filter field configuration and nearly all the source parameters: the experimental location of the center is the sum of many different contributions, and so far it is not clear how to de-convolute them.

4.2 Introductory remarks on the experimental results

4.2.1 Relation between BES intensity and current density

This section explains in detail how the beam interacts with the background gas, describing also the relation between the electrically measured extracted ion current density j_{ex}, the total light emitted by the beam and the total light collected by the BES: here and in the following the term "light" (or "light emitted by the beam") will refer to the Doppler-shifted H_α light *only*.
The main conclusions that will be discussed in detail are as follows:

- The light *emitted* by the beam is linearly proportional to the electrically measured ion current density j_{ex}.
- The light *collected* by the five Beam Emission Spectroscopy telescopes is linearly proportional to the ion current density only within short current intervals: indeed the dependence is globally parabolic.

To begin with, a brief theoretical description of the light emission mechanism is given.

Light emission mechanism: H_α Balmer line The H_α emission is a two step process: firstly a negative ion of the beam loses its electron by collision with an atom of the background gas (*electron detachment*, Eq. 3.1), ending in an excited state ($n = 3$). It consequently decays to the lower state $n = 2$ by emission of one photon: such spectral line, usually known as H_α *Balmer line*, is Doppler-shifted because of the motion of the atom.
The rate of electron detachment with final excited state $n = 3$ is:

$$\Gamma = n^-_{beam} \cdot v_b \cdot \sigma_{det,3s}(E) \cdot n^0_{bk} \tag{4.17}$$

where n^-_{beam} and n^0_{bk} stand respectively for the mean beam density and the density of background gas, v_b is the mean velocity of a beam ion while $\sigma_{det,3s}(E)$ is the electron detachment cross section with final state $n = 3$. This cross section is in principle a function of the energy of the beam particle.

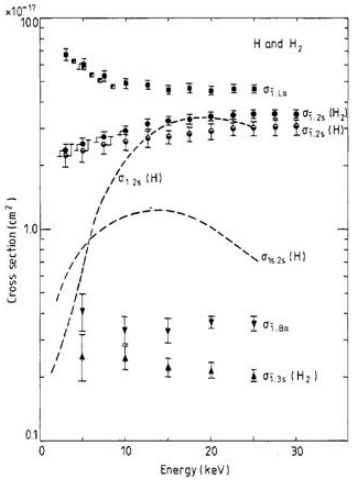

Figure 4.15. Cross section of electron detachment of H^- colliding with H or H_2, as a function of H^- energy [30].

Figure 4.15 shows the cross section of the general process

$$H^- + X \rightarrow H(n,l) + X(\Sigma) + e \tag{4.18}$$

namely the electron detachment of H^- colliding with H or H_2 ($X = H$ or $X = H_2$; Σ denotes all final and bound states of the target), as a function of H^- energy: both the total cross section for Balmer-α emission ($\sigma_{\bar{1},B\alpha}$) and for electron detachment with final state $n = 3$ ($\sigma_{\bar{1},3s}(H_2)$) are *flat* in the typical ion energy range at BATMAN ($[10 \div 22]$ keV excluding the stripped particles, which are less energetic).
Apart from pressure scans, in a typical experimental scan the pressure in the tank is maintained constant by the vacuum-pumps system: hence the background gas density n^0_{bk} is constant too.

As a result of these observations, the rate Γ at which the H_α photons are emitted depends, during a typical scan, solely on the product $n^-_{beam} \cdot v_b$ and thus on the extracted ion current density $j_{ex} = n^-_{beam} \cdot e \cdot v_b$: *the intensity of emitted H_α light is then expected to be linearly proportional to the extracted ion current density j_{ex}.*

Light collection mechanism: BES telescopes BATMAN test facility is equipped with five BES telescopes, arranged vertically as shown previously in Figure 3.8. Each telescope collects the light along its line of sight, which is roughly a cone, for an integration time of 1 s.
At fixed extraction and acceleration voltages, the amount of Doppler-shifted H_α light collected by the telescope is proportional to the *integral* of the Doppler-shifted H_α line in the spectrum or, equivalently, to the *height* of such line; the integral and the height of the line contain essentially the same piece of information. The **height of the Doppler-shifted H_α line** was chosen as the quantity to be studied, and it is conventionally referred to as ***BES intensity***.

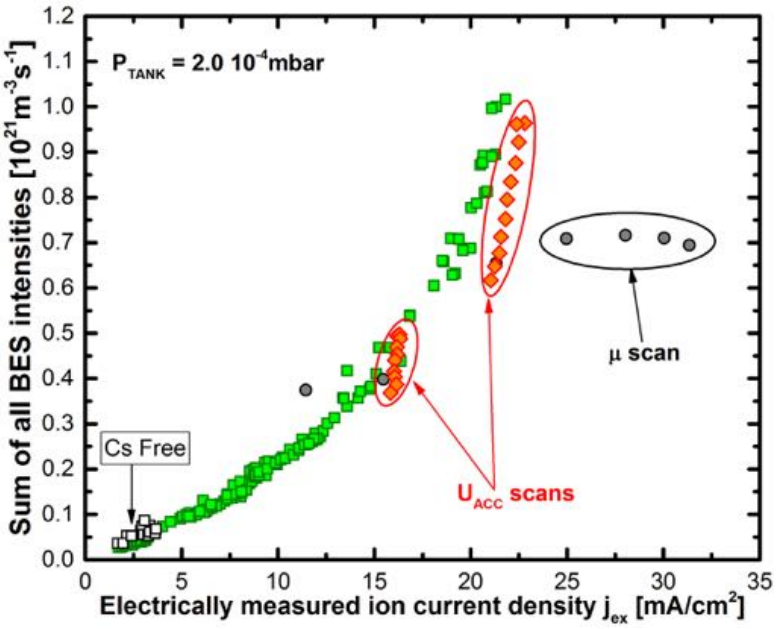

Figure 4.16. Sum of the five BES intensities as a function of the electrically measured ion current density: the dependence is found to be parabolic.

It is important to point out that the total amount of beam light collected by the five BES (proportional to the sum of the five BES intensities) is proportional but not equal to the total amount of light emitted by the beam (namely Γ of Eq. 4.17), since each telescope has a *finite and fixed cone-of-view*. The **fraction** of collected light depends on the *optical properties of the beam*, namely on its divergence: the more focused the beam, the higher the fraction of beam "seen" by each BES channel along its cone-of-sight and thus the higher the fraction of collected light.

Figure 4.16 shows the sum of the five BES intensities as a function of the electrically measured ion current density, for a series of scans performed at the same tank pressure ($P_{tank} = 2.0 \cdot 10^{-4}$ $mbar$): the departure from a linear dependence is explained exactly with the mechanism here exposed.

If the current is increased, and the voltages are kept constant, the normalized perveance Π/Π_0 will increase, leading to a more and more focused beam in accordance with the parabolic relation between beam divergence and normalized perveance of Figure 2.11.
Consequently, as the current increases, the global amount of light emitted by the beam must increase ***linearly*** with the current (Eq. 4.17) but, since the beam is more and more focused, the total amount of light *collected* by the BES increases faster (the dependence is by no means linear, but rather ***parabolic***). The parabolic shape is not an accident, but stems from the parabolic relationship between divergence and normalized perveance.

Finally, it may be noticed that since in a typical scan the explored range of current is not broad (usually not more than 10 mA/cm^2), the dependence of the total light collected by the BES on the extracted current density appears *linear* (the details are given in the next chapter): the curve in Figure 4.16 can indeed be locally approximated with a straight line.

4.2.2 Calorimetric measurements with mini-STRIKE and the copper calorimeter

A calorimeter is, in general, a diagnostic tool that intercepts the beam and measures the local temperature increase ΔT, due to the beam power, on various positions of its surface.
The signal from a calorimeter is proportional to the ***energy flux*** of the beam, which is by definition the *product* between the beam current density j_{ex} and the *total voltage* of the extraction and acceleration system $U_{HV} = U_{ex} + U_{acc}$ (proportional to the mean energy per ion).

The local ΔT bi-dimensional pattern is usually interpolated by a proper 2D function, a vertical skewed-Gaussian multiplied by a horizontal parabola in *mini-STRIKE* (as explained above) and a 2D-Gaussian for the copper calorimeter. The ***volume*** of the fitting function is measured in $[^\circ C \cdot m^2]$. This can be calibrated to Watt and thus it becomes a rough estimate of the beam power; since the power divided by the extraction area equals the beam energy flux at the GG ($j_{ex} \cdot U_{HV}$), then it is clear that *the volume of the fitting function must be proportional to the extracted current density j_{ex} as long as the total grid voltage U_{HV} is constant.*

This relation should be true both for *mini-STRIKE* and the copper calorimeter; the volume of the skewed-Gaussian of the former (Vol_{MS}) and the volume of the 2D-Gaussian of the latter are expected to increase roughly linearly with the electrically measured extracted ion current density

(Eq.4.19 and Eq.4.20). A detailed study of this topic is carried out in the next chapter.

$$Vol_{MS} \sim j_{ex} \cdot U_{HV} \sim j_{ex} \tag{4.19}$$

$$Vol_{CC} \sim j_{ex} \cdot U_{HV} \sim j_{ex} \tag{4.20}$$

4.2.3 Agreement between mini-STRIKE and BES

As explained in Section 4.2.1, the light emitted by the beam and collected along the line-of-sight of one BES telescope is proportional to the local ion current density (Eq. 4.17); similarly, the local temperature increase given by *mini-STRIKE* is proportional to the local energy flux and therefore (at fixed U_{HV}) to the local current density. As a result, a linear proportionality is expected between the vertical temperature profile on *mini-STRIKE* and the vertical BES intensity profile.

Figure 4.17 shows the vertical temperature profile given by *mini-STRIKE* and the vertical BES intensity profile for some beam pulses of a Cs-conditioning day. The agreement between the diagnostics is very good; moreover, it has been verified widely in several other experimental conditions.

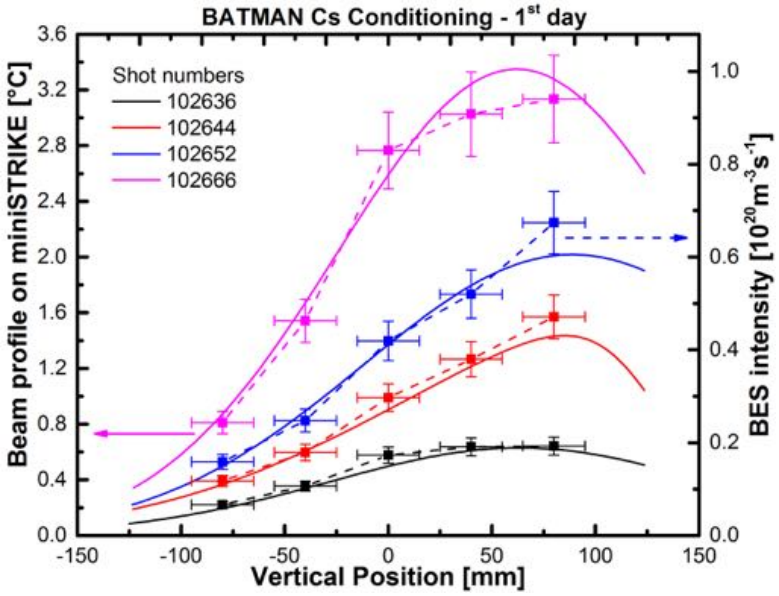

Figure 4.17. Beam vertical profile on *mini-STRIKE* and BES intensities for four beam pulses during a Cs-conditioning day in Hydrogen.

Figure 4.17 shows also the typical horizontal and vertical error bars. A relative error of 10 % is taken as uncertainty on the BES intensity, while the error on the vertical position comes from geometrical reasonings. Each telescope is indeed characterized by a cone-of-sight intercepting the beam, with angular aperture of 0.6° : the diameter of the cone is 20 mm at the telescope entrance (the diameter of the lens), while it is approximately 30 mm at the center of the beam

(about 50 cm from the lens). Then a ± 15 mm uncertainty is taken for the vertical position of each BES telescope.

4.2.4 Correlation between beam and extracted current vertical profiles

Figure 4.18 shows a schematic view of the extraction and acceleration system and of the BES-telescopes vertical array; it suggests that a correlation can be expected between the extracted current distribution at the PG (a), the accelerated current distribution at the GG (b) and finally the BES intensity (vertical) distribution at the telescopes location (c).
The aim of this section is just to provide some basic observations and reasonings that bear out such hypothesis; a rigorous proof, indeed, can only be given by a complete simulation of beam behavior between the grids and then in the drift region.

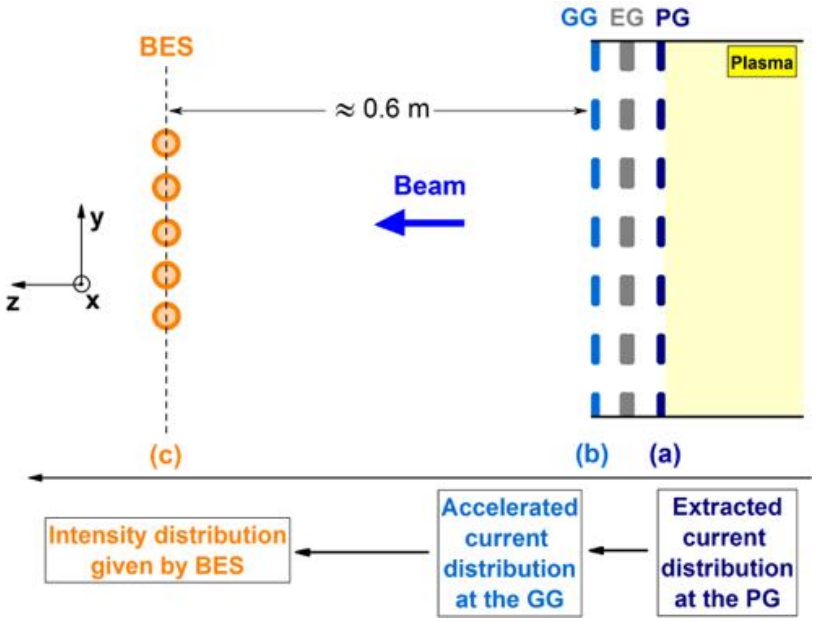

Figure 4.18. Conceptual scheme of the correlation between the vertical profiles of the beam at different locations along the beam-line.

Figure 2.12 shows in detail the passage from (a) → (b), namely the transmission of the ions from the plasma source to the vacuum chamber. The ions, as previously described, enter a PG aperture and get accelerated in two steps; they form a beamlet, which has optical properties. In the hypothesis that the ion losses between the grids are small (low stripping) the amount of ions exiting the GG is similar to the current entering the PG: this reasoning suggests that the vertical profile of accelerated current density (GG) is similar in shape to that of the extracted current density (PG).

Once in the vacuum, the repulsion between the beamlet charges induces an expansion of the beamlet perpendicularly to its axis: the divergence $\delta = \delta(z)$ increases. At the same time the charges collide with the background gas (H_2) and they create positive ions H^+. At a certain location downstream of the GG, the positive space charge of the background compensates for the negative space charge of the beamlet: the beamlet is said to be *space charge compensated*

and the divergence no longer increases. The same reasoning is valid for the beam, since it is the superimposition of many small beamlets.
As a consequence of such dynamics, the divergence at the GG $\delta(z = 0$ m) and at the BES telescope location $\delta(z = 0.6$ m) are functionally correlated; the same is true for the local current density, which is a function of the beam divergence. Section 4.2.1 showed that the local current density and BES intensity are proportional; therefore *the beam accelerated current density profile at the GG (z = 0 m) is somehow correlated to the BES intensity vertical profile at the telescope position (approximately z = 0.6 m).*

Putting together these considerations, *the Doppler-shifted H_α intensity distribution at the BES location reflects the distribution of the extracted current density at the PG*: **if a beam inhomogeneity is observed by the BES, then a similar inhomogeneity is expected to exist at the PG**, namely the H^- are extracted dis-uniformly along the grid. This is a crucial point, because every variation of the vertical beam inhomogeneity, namely a variation in the shape of the vertical beam profile, can be interpreted as a modification of the ion extraction conditions at the PG.

Finally, it is worth to notice that horizontally, namely along the x-direction, no shift of the beam is expected: thereby all the following studies concern solely the behavior and the characterization of the beam in the vertical (y) direction.

4.2.5 Definition of the beam center

The *beam center* is the spatial location of the maximum ion flux of the beam; it corresponds to the position of maximum ΔT in the temperature pattern given by *mini-STRIKE* or, similarly, by the copper calorimeter.
As a consequence of such definition, the position of the *beam center* depends primarily on two factors:

- the **inclination of the ion trajectories** ($v \times B$ interaction between the beam particles and the Filter Field)
- the **vertical distribution of the current** at the Plasma Grid

The *inclination of the ion trajectories* is basically due to a $v \times B$ force: the filter field indeed penetrates the vacuum chamber and it induces a vertical shift on the ions, as it will be thoroughly described in the next chapter. The deviation of the ion trajectory can be modified by changing the *filter field strength* in the vacuum region: several filter field configurations are available in BATMAN (see Figure 3.3), and the net shift can be upwards or downwards.
Furthermore, the ion trajectory inclination can be altered also using more massive ions (eg: Deuterium instead of Hydrogen): a higher mass will result into a higher Larmor radius ($r_L \sim m$), thus leading to a lower vertical deviation of the particle.

The *vertical distribution of the ion current* at the PG is experimentally found to depend, at z = 3, on many source parameters such as the RF power, the bias current and the amount of Cs in the source, while at z = 9 such dependencies are not found; in the next chapter a detailed and in-depth analysis of these trends is carried out and some possible interpretations are provided.

It is also important to point up that *the shift due to the magnetic filter field is a **first order** effect*, while *the movements due to change in the vertical current distribution are a **second order** effect.*

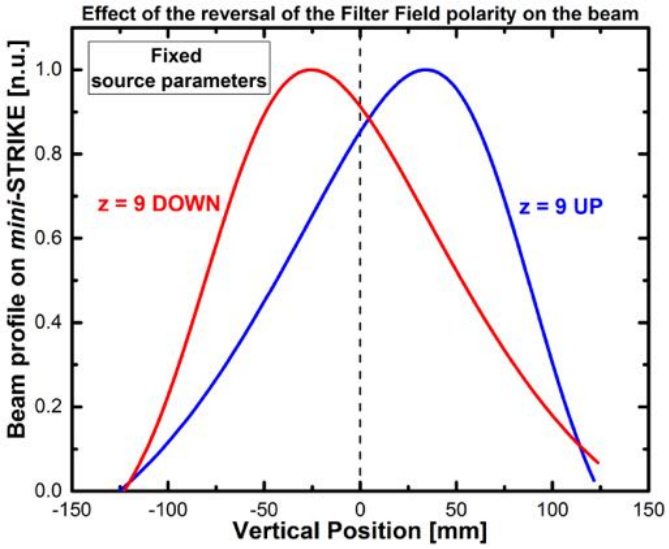

Figure 4.19. Vertical beam profiles on *mini-STRIKE* at fixed source parameters but opposite filter field polarity: the curves are symmetric with respect to the *zero of BATMAN*, namely the vertical position of the horizontal plane of symmetry of the source.

Figure 4.19 shows the beam vertical profile on *mini-STRIKE* for two pulses with fixed source parameters and opposite filter field polarity (z=9 UP and z=9 DOWN). The profiles are clearly symmetric with respect to the *zero of BATMAN*, namely the vertical position of the horizontal plane of symmetry of BATMAN source. Such symmetry implies that the *zero of the beam center*, which would be the vertical location of the beam center if no filter field were applied, essentially coincides with the zero of BATMAN source.

4.2.6 Agreement between BES and the copper calorimeter

The aim of this section is to compare the shape and the position of the center of the beam vertical profile at two different locations: approximately 0.7 m and 1.7 m downstream the grounded grid, as provided by the BES telescopes and the copper calorimeter respectively. The comparison has been made for the z = 3 UP and z = 9 UP filter field setups.
The **beam center** position is expected to depend, as previously outlined, on two elements: (1) the inclination of the ions trajectories and (2) the vertical distribution of the current. Both contributions are in principle present.
For the considered "UP" filter field setups, the particle trajectories are inclined slightly upwards; as a result of effect (1) only, the beam center is expected to move *upwards* as the distance from the grounded grid increases.
The influence of effect (2), namely the vertical current distribution, on the beam center is more complicated. Experimental measurements, thoroughly discussed in the following chapter, show that in the beam a vertical asymmetry and inhomogeneity exists. This inhomogeneity is expected to *reduce gradually as the beam propagates*: indeed the beamlets overlap because of their divergence, leading to a smoothing of the vertical beam profile and a movement of the beam center towards the zero, namely *downwards*. Such behavior is confirmed by some simulations performed with the RFX code previously described for an inhomogeneous beam: as the distance from the GG is increased, the beam vertical profile smooths (Figure 4.20a) and the position of

the center shifts towards the zero (Figure 4.20b).

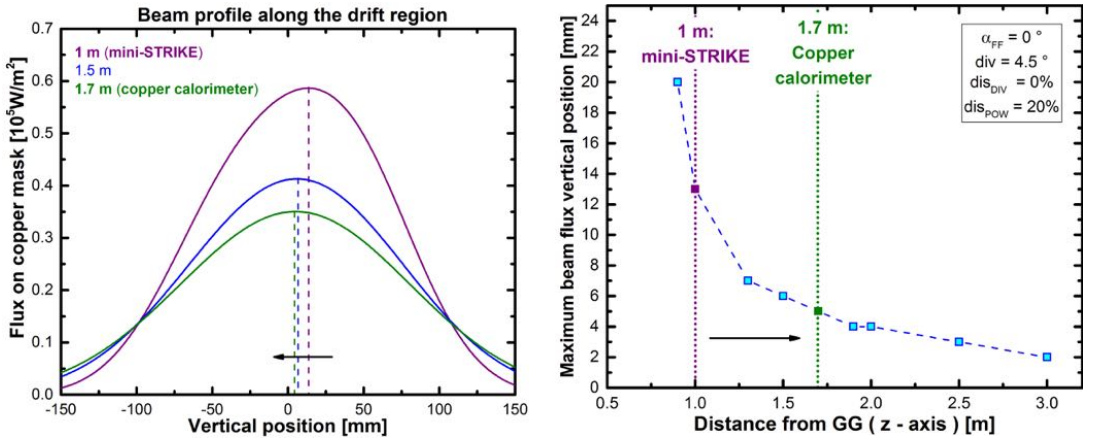

(a) **(b)**

Figure 4.20. Vertical beam flux profile and vertical position of the beam center (left) at different distances from the GG (right), as given by the RFX code: the parameters of the simulation are shown in the legend of the plot on the right.

In Figure 4.21a and 4.21b the five BES intensities, connected by a dashed line, and the beam vertical profile given by the copper calorimeter are shown for two different magnetic setup: $z = 3$ UP and $z = 9$ UP. From both figures it is clear that *the beam center moves downwards with increasing* z; this experimental observation suggests that the vertical position of the beam center along the vacuum chamber depends more on the vertical distribution of the current, contribution (2), than on the inclination of the ions trajectories, contribution (1).

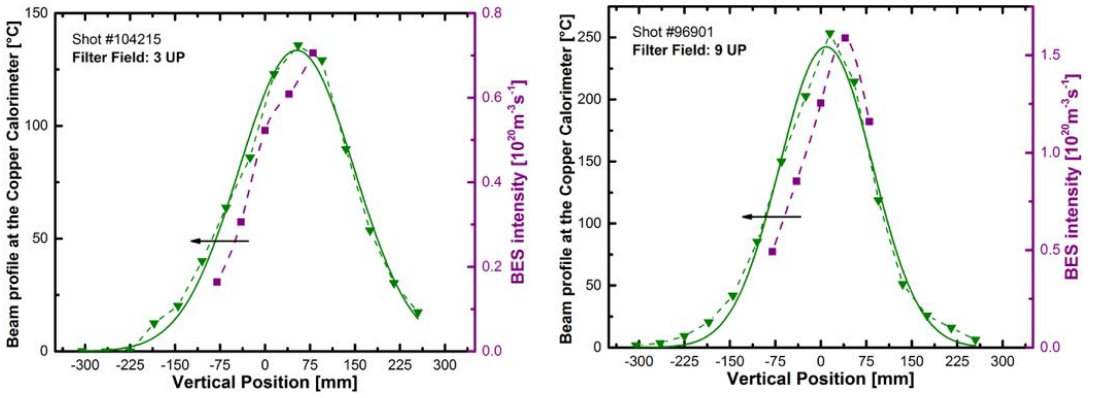

(a) **(b)**

Figure 4.21. Beam profile at the copper calorimeter and the five BES intensities for two magnetic setups: z = 3 UP (left) and z = 9 UP (right).

5 BATMAN beam characterization

The present chapter concentrates on the study of the negative ion beam properties - e.g. divergence, homogeneity and asymmetries - in different operational scenarios: with different magnetic filter field configurations, source parameters and with different gases. Possible physical interpretations for the results are discussed, in some cases supported by numerical simulations developed ad hoc.

Figure 5.1 shows six operational parameters that in principle affect the amount of ions extracted from the source: the **power** supplied to the RF-driver, the **pressure** of the source-filling gas, the quantity of **cesium** present in the source volume, the **bias current** collected at the plasma grid, the **extraction voltage** and finally the **filter field**.

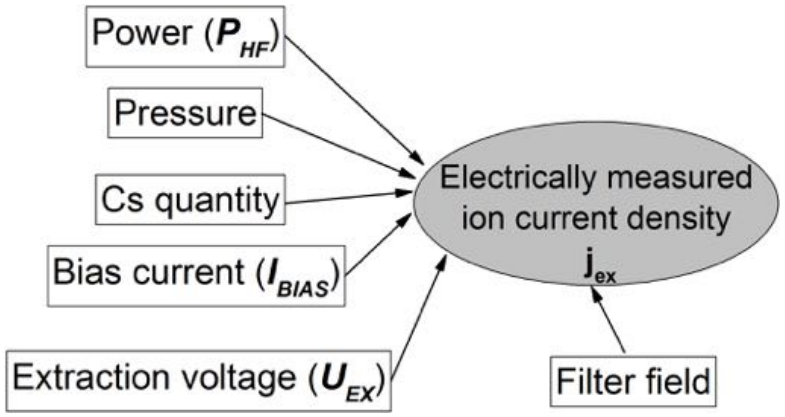

Figure 5.1. Operational parameters of BATMAN that in principe can affect the electrically measured ion current density j_{ex}.

Another important operational parameter is the **acceleration voltage**, namely the voltage drop between the extraction grid and the grounded grid: such voltage determines the energy of the beam but does not affect the amount of extracted ion current.

For the majority of these parameters a dedicated scan has been performed, in order to *study and comprehend the influence of each parameter on the properties of the beam.*

5.1 Current density dependence on source parameters

The source of BATMAN is usually operated in *surface production*, namely almost the whole beam current is composed of negative ions created at the plasma grid (PG). Neutral or positively charged hydrogen atoms coming from the plasma hit the PG surface, capture respectively one or two electrons and thus become H^-: the electron capture probability is enhanced by lowering the work function of the surface with Cs layers (see section 2.2.2).

The intensity of the negative ion production and, consequently, the amount of extracted H^- current depend on the parameters outlined in Figure 5.1; the effect that each parameter has on the *electrically measured ion current density* j_{ex} is shown in Figures 5.2a, 5.2b, 5.3a and 5.3b. The definition of the ion current density j_{ex} has been given at the end of section 3.1.3.

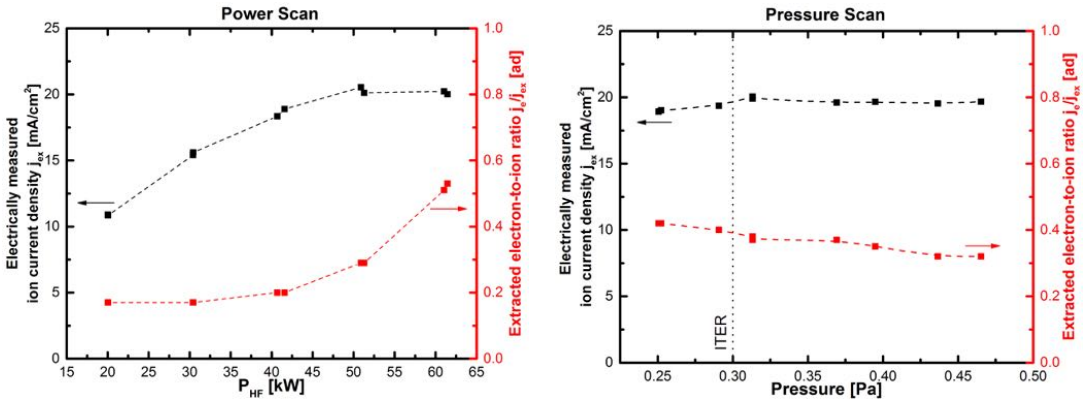

(a) **(b)**

Figure 5.2. Electrically measured ion current density j_{ex} and extracted electron-to-ion ratio j_e/j_{ex} as a function of RF power (left) and source pressure (right). The other source parameters are $P = 0.6\ Pa$, $I_{BIAS} = 5\ A$, $U_{ex} = 5\ kV$, $U_{acc} = 15\ kV$ (left) and $P_{HF} = 40\ kW$, $I_{BIAS} = 1\ A$, $U_{ex} = 5\ kV$, $U_{acc} = 15\ kV$ (right).

A higher **RF power** will result in a higher dissociation rate of the gas in the driver, a higher amount of plasma in the source and thus a higher flux of H^0 and H^+ towards the PG: the negative ion creation rate and consequently the extracted current density will increase (Figure 5.2a). The flux of particles onto the plasma grid can in principle be enhanced also by a higher pressure, since the **source pressure** determines the collision rate between the plasma and the neutral gas (H_2): however, the experimental dependency of the ion current density on the source pressure is quite flat (Figure 5.2b).

The amount of **Cesium** in the source - on lateral walls, on the plasma grid and dispersed in the volume - deeply affects the work function of the PG surface and thus the extracted ion current. The *intensity of the Cs de-excitation line at 852 nm* is a useful indicator of the amount of *neutral* Cs, proportional to the total amount of Cs (neutral or charged), in the source: such line is observed along a vertical line-of-sight (y direction) in front of the plasma grid, hence providing a LOS-integrated information. Figure 5.3a clearly shows that the extracted current density steadily increases with Cs evaporation in the source: the data refer to a typical *cesium conditioning day* in Hydrogen starting with a "clean-source" (Cs-free).
The role that the **bias current** - sometimes abbreviated simply as "bias" - has on the extracted ion current density is less clear and is a topic under investigation. From an experimental point of view, a strong correlation exists between the bias current and the properties of the beam: a higher bias leads usually to a lower current density j_{ex} and a much lower co-extracted electron current j_e up to $I_{BIAS} \sim 13\ A$, so that the *extracted electron-to-ion ratio* j_e/j_{ex} is very small (red points in Fig. 5.3b).

In the previous figures the **extracted electron-to-ion ratio** j_e/j_{ex} dependency from source parameters is also shown (in red); such ratio must be < 0.5 in Hydrogen and < 1.0 in Deuterium in order to meet ITER requirements (see Table 3.1).
It is worth to analyze the trend of j_e/j_{ex} during a Cs-conditioning day in Hydrogen (Figure

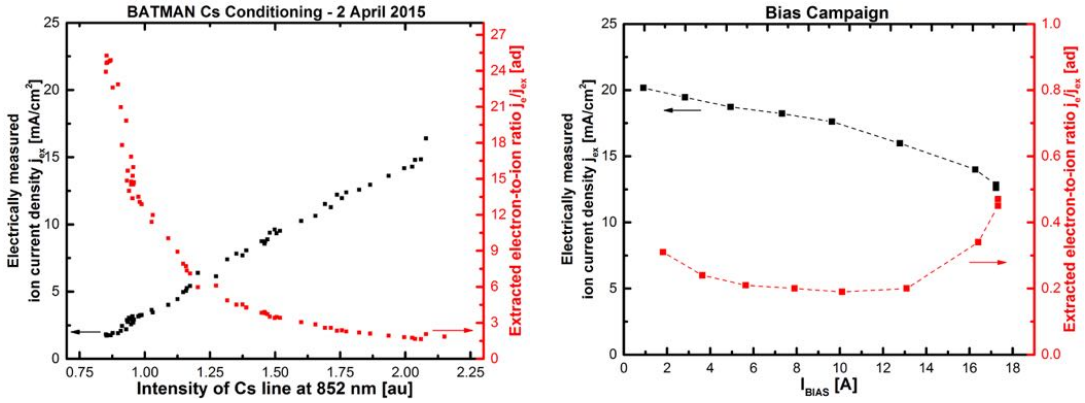

(a) **(b)**

Figure 5.3. Electrically measured ion current density j_{ex} and extracted electron-to-ion ratio j_e/j_{ex} as a function of the intensity of Cs line at 852 nm (left) and bias current (right). The other source parameters are $P_{HF} = 60\ kW$, $P = 0.3\ Pa$, $I_{BIAS} = 6\ A$, $U_{ex} = 5\ kV$, $U_{acc} = 10\ kV$ (left) and $P_{HF} = 40\ kW$, $P = 0.6\ Pa$, $U_{ex} = 5\ kV$, $U_{acc} = 15\ kV$ (right).

5.3a). At the beginning of the day almost no Cs is present (intensity of Cs line below 1.00) and the source works in *volume production*: the extracted ion current is low ($< 3\ mA/cm^2$) and the extracted electron-to-ion ratio - around 25 - is very far from ITER requirements. When Cs is evaporated into the source, a transition from volume to source production takes place and j_e/j_{ex} decreases; after some days of conditioning in Hydrogen it is usually possible to achieve ITER parameter $j_e/j_{ex} < 0.5$.

5.2 Influence of the Filter Field

The source of BATMAN is equipped, as previously described, with a *magnetic filter field* in the expansion region: its aim is to filter out the hot electrons ($T_e > 2$ eV) from the plasma which flows toward the grids. The filter field is mainly in the horizontal direction (B_x) and it penetrates the drift region (Figure 3.3): here a $v \times B$ *interaction between the field and the beam* takes place and a **vertical shift of the beam** is expected. Figure 5.4 shows schematically the interaction between the beam, moving with mean velocity v in the z direction (from the grids into the vacuum chamber), and the filter field B_x: the resulting Lorentz force $F_L = q \cdot (v \times B_x)$ is upwards (the charge q is negative).
Several different filter field setups are available in BATMAN (see Figure 3.2); the results here presented have been obtained with the "UP" configurations, leading to a drift upwards of the beam, but similar reasonings can be done if the field polarity is reversed ("DOWN").

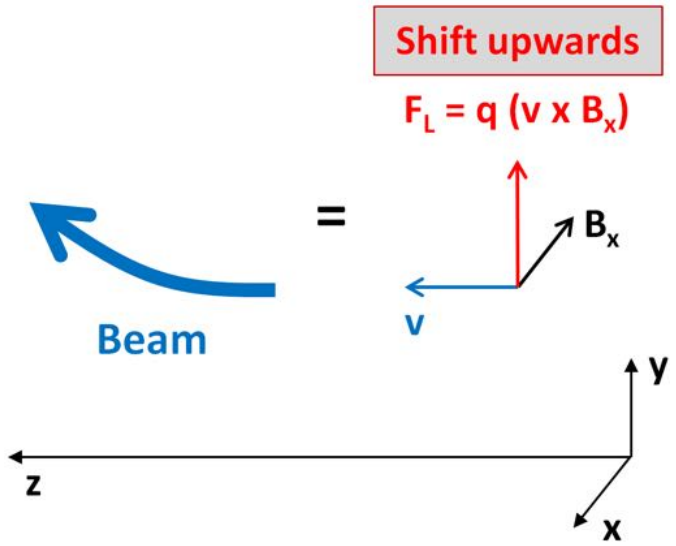

Figure 5.4. The interaction between the beam particle mean velocity v and the filter field B_x results into a $v \times B$ shift in the vertical direction (y - axis).

Figure 5.5a shows the experimental influence of the filter field on the beam vertical profile; the stronger the field in the drift region - namely passing from z = 14 to z = 9 and then z = 3 - the higher the vertical shift of the beam. This trend is in complete agreement with theoretical expectations: when the mean B field in the vacuum chamber increases, the Larmor radius of the beam particles decreases ($r_L \sim 1/B$) and thus the vertical deviation increases. Figures 5.6a and 5.6b show the effect of the filter field strength for a power scan and a bias scan respectively: it is again clear that a stronger filter field in the drift region provokes a higher deflection of the beam.

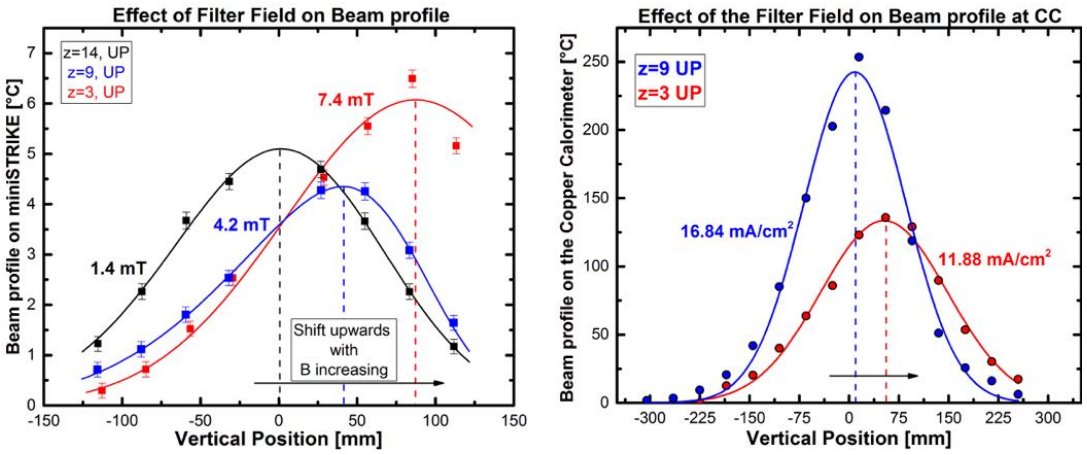

(a) **(b)**

Figure 5.5. Effect of filter field strength on beam vertical profile as seen by *mini-STRIKE* (left) and the copper calorimeter (right). The field strength $|B_x|$ at the PG for each magnetic setup (left plot) and the total ion current density j_{ex} (right plot) are also indicated: the different current densities are a consequence of different conditioning of the source. The grid voltages are fixed at $U_{ex} = 5\ kV$ and $U_{acc} = 15\ kV$ for both plots.

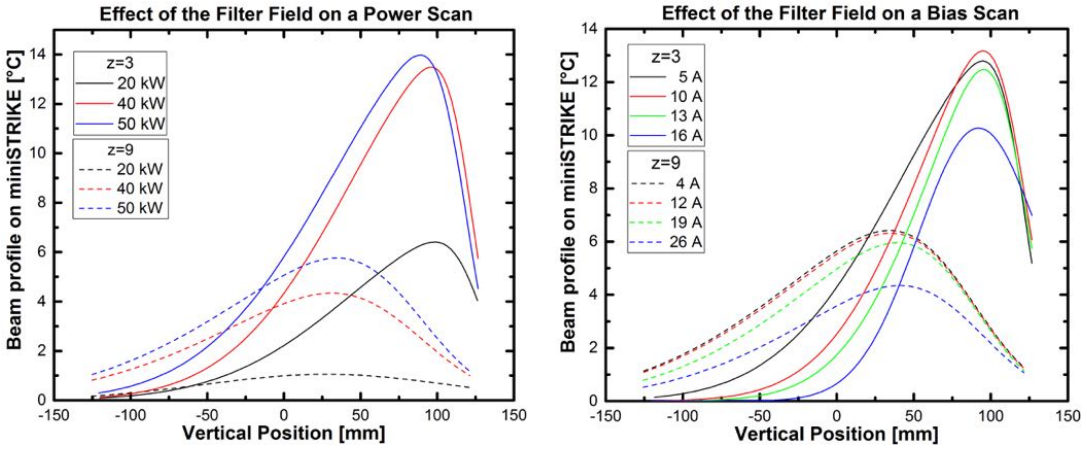

(a) **(b)**

Figure 5.6. Effect of filter field strength on beam vertical profile, as seen by *mini-STRIKE* , for a power scan (left) and a bias scan (right). The other source parameters are: $P = 0.6\ Pa$, $I_{BIAS} = 10\ A$ (at z = 9) and $5\ A$ (at z = 3), $U_{ex} = 5\ kV$, $U_{acc} = 10\ kV$ (left plot); $P_{HF} = 50\ kW$ (at z = 9) and $40\ kW$ (at z = 3), $P = 0.6\ Pa$, $U_{ex} = 5\ kV$, $U_{acc} = 15\ kV$ (right plot).

5.3 Influence of the production mechanism (surface or volume)

The influence of the production mechanism (surface or volume) on beam properties is here investigated by comparing different types of scan - pressure, power and bias scans - performed without Cs (open symbols) and with Cs (full symbols). The main observations that will be discussed in more detail in the next paragraphs are as follows:

- In a Cs-Free source the achieved extracted ion current densities are much lower than in a cesiated source (low source performance).
- In a Cs-Free source the beam divergence is much higher than in a cesiated source (bad beam optics).

Current density Figures 5.7a and 5.7b show the electrically-measured ion current density j_{ex} for a typical power and bias scan, with and without Cesium. The maximum current density never exceeds 4 mA/cm^2 in volume production, while it achieves up to 22 mA/cm^2 in a Cesiated source; furthermore it can be observed that the dependence of the ion current density on pressure is visible only during the Cs-Free operation (Figures 5.7a and 5.7b).

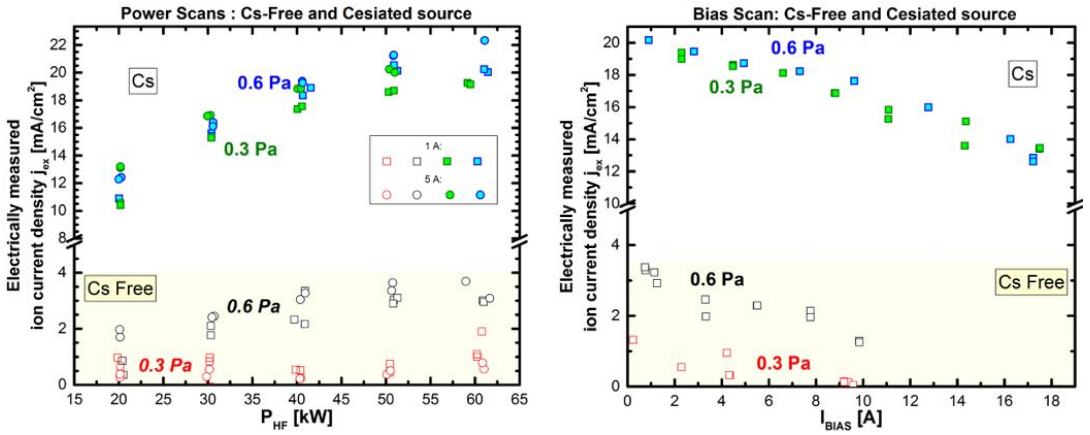

(a) (b)

Figure 5.7. Electrically measured ion current density j_{ex} for power scans (left) and bias scans (right) performed with and without Cs, with pressure P = 0.3, 0.6 Pa and bias current I_{BIAS} = 1, 5 A. The grids voltages are U_{ex} = 5 kV, U_{acc} = 10 kV for both plots; the RF power of the bias scans is P_{HF} = 40 kW.

Beam divergence The divergence of the beam is strongly influenced by the beam current: the current density indeed defines the normalized perveance (Eq. 2.9), which determines - at fixed extraction and acceleration voltages - the beam divergence (see section 2.4.2 for a detailed description). Moreover, the *divergence-to-normalized perveance* relation is experimentally approximated by a parabola (see Figure 2.11).
Since in Cs-free operation the current is much lower than in a cesiated source, the divergence is expected to be higher: this expectation is fully confirmed by Figure 5.8a and Figure 5.8b, showing the BES mean divergence - mathematical average of the divergences from the five BES telescopes - as a function of the RF power and the source pressure.

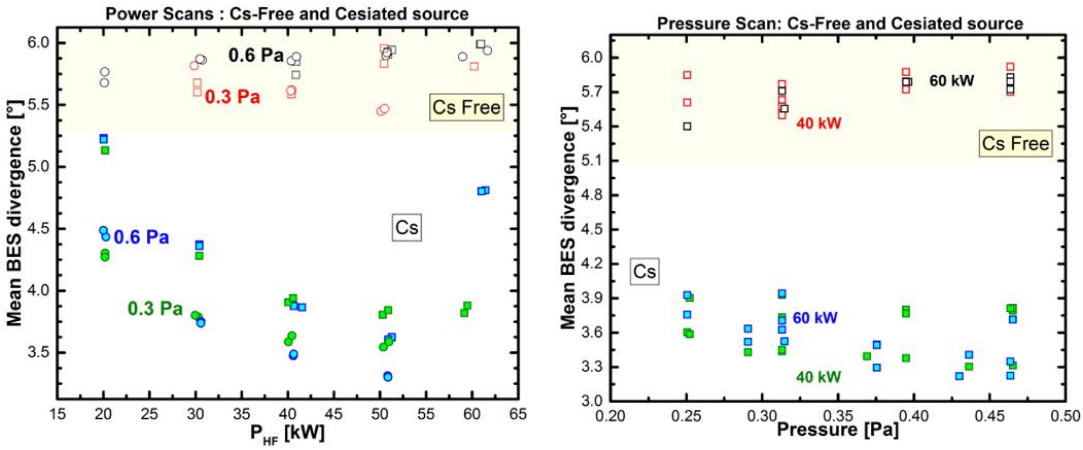

(a) (b)

Figure 5.8. Mean BES divergence for power scans (left) and pressure scans (right) with and without Cs. The grid voltages are $U_{ex} = 5\ kV$, $U_{acc} = 10\ kV$ for both plots; the bias current for the pressure scans is $I_{BIAS} = 1\ A$.

In Figure 5.9 the BES intensity from each telescope is plotted against the correspondent divergence. Such figure reproduces the *divergence-to-normalized perveance* parabolic dependence since the BES intensity and the normalized perveance Π/Π_0 are proportional: indeed the BES intensity is in the very first approximation proportional to the local current density, which is linearly proportional to the local perveance.

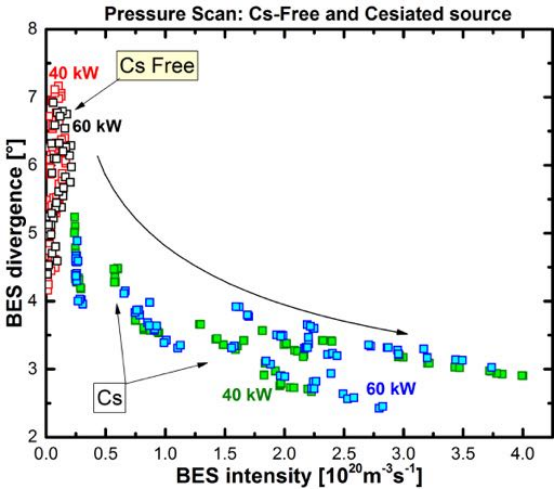

Figure 5.9. BES-telescope divergence as a function of the correspondent intensity: the parabolic shape resembles the *divergence-to-normalized perveance* relation.

5.4 Influence of the extracted ion current (at z = 3)

In the first part of this section a ***consistency check*** *between the three beam diagnostic* (BES, *mini-STRIKE* and the copper calorimeter) and the electrically measured ion current density of the beam (j_{ex}) is carried out: this is performed by studying the *integrated quantities* provided by each diagnostic.
In the last part of the section the *influence of the ion current on the* ***beam vertical inhomogeneity*** is discussed for multiple experimental situations: several power scans, pressure scans, bias scans and some Cs-conditioning days are thoroughly analyzed. A new analytic indicator of the vertical inhomogeneity of the beam is introduced; the results, presented as statements, are accompanied by possible physical interpretations.

5.4.1 Trend of integrated quantities

In order to understand whether there is a general *consistency* between the three beam diagnostics and the electrically measured current of BATMAN, a comparison between the *integrated quantities* provided by each diagnostic (BES, *mini-STRIKE* and the copper calorimeter) and the electrically measured ion current density j_{ex} is carried out. The integrated quantity of each diagnostic and its physical meaning is here briefly discussed:

- (1) the **sum of the five BES intensities**: this value is expected to be proportional to the total amount of light emitted in the interaction between the beam and the background gas, which is in first order proportional to the ion current density j_{ex} (Eq. 4.17).
- (2) the **volume of the beam-fitting-function at *mini-STRIKE*** , which is expected to be proportional to the total power and thus to the ion current density j_{ex} (Eq. 4.19).
- (3) the **volume of the beam-fitting-function at the Copper Calorimeter**, which similarly should be proportional to the beam power and therefore to the ion current density j_{ex} (Eq 4.20).

Consequently the general expectations are the following:

- **Expectation 1** The three integrated quantities (1), (2) and (3) are *linearly proportional* to the ion current density j_{ex}; this statement is true for quantity (1) only for small current density intervals, as explained in section 4.2.1.
- **Expectation 2** The three integrated quantities (1), (2) and (3) are proportional to each other during every scan.

The data that will be presented belongs to various experimental scans - varying the RF power, the source pressure or the bias current - and to some Cs-conditioning days in Hydrogen, primarily performed with the z = 3 UP magnetic filter field setup.

Expectation 1

In Figure 5.10 the *volume* of the beam-fitting function at *mini-STRIKE* (integrated quantity (2)) and the *integral* of the vertical beam profile at *mini-STRIKE* as a function of j_{ex} are shown: both quantities depend linearly on the current at fixed acceleration voltage ($U_{acc} = 10\ kV$ or $U_{acc} = 15\ kV$).
Two further remarks can be made on Figures 5.10a and 5.10b: (a) both the integral and the

volume are zero at very low - but not null - ion current density (below 2 mA/cm^2) and (b) for high ion current ($j_{ex} > 18\ mA/cm^2$) the volume, unlike the integral in the vertical direction, is no more linear with respect to j_{ex}. The first observation is easily explained: since a low current results into a high beam divergence - due to the parabolic relationship between divergence and normalized perveance - the beam optics is really bad when $j_{ex} < 2\ mA/cm^2$, the ions intercept the grounded grid and therefore cannot reach the calorimeter. For the second observation, the parting from linearity is presumably due to a failure of the 2D fit of *mini-STRIKE* ; since the problem does not affect the integral, the fit is wrong solely in the horizontal direction (see section 4.1.2 for more details about the fit procedure).

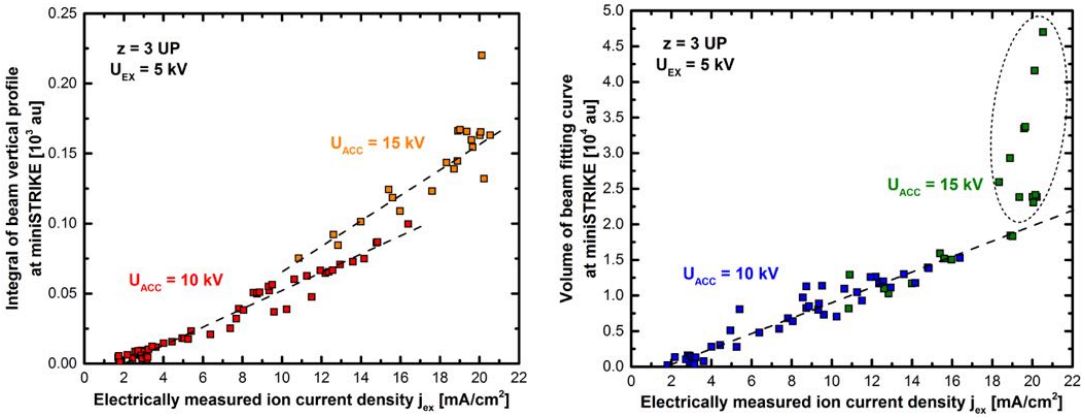

Figure 5.10. Integral of the beam vertical profile (left) and volume of the beam-fitting-curve (right) at *mini-STRIKE* as a function of the electrically measured ion current density j_{ex}.

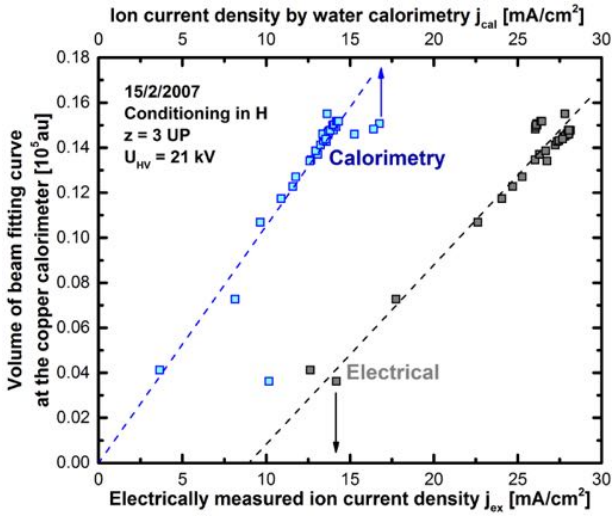

Figure 5.11. Volume of the beam-fitting-curve at the copper calorimeter as a function of the electrically measured ion current density (j_{ex}) or of the ion current density by water calorimetry (j_{cal}); the other source parameters are $P_{HF} = 66\ kW$, $P = 0.5\ Pa$, $I_{BIAS} = 2\ A$, $U_{ex} = 10\ kV$ and $U_{acc} = 11\ kV$.

Figure 5.11 shows the volume of the beam-fitting-curve at the copper calorimeter - integrated

quantity (3) - plotted against j_{ex} and the ion current density by water calorimetry j_{cal}; the volume decreases linearly with both the currents. According to the trend of the data - the dashed line - for $j_{ex} < 10\ mA/cm^2$, corresponding to $j_{cal} < 8\ mA/cm^2$ approximately, the signal on the copper plate is almost absent: again this may happen because the beam is lost between the grids as a result of bad optics. The difference existing between the two measured currents ($j_{ex} > j_{cal}$) bears out this interpretation: it clearly indicates that part of the extracted current j_{ex} does not reach the copper calorimeter, hence is lost on the grounded grid or onto the walls of the vacuum chamber.

Expectation 2

Figures 5.12a, 5.12b, 5.13a and finally 5.13b clearly show that the sum of the BES intensities (integrated quantity (1)) and the volume of beam-fitting-curve at *mini-STRIKE* (integrated quantity (2)) are proportional during each scan. Other results, here not shown, indicate that the same proportionality exists with the volume of the beam-fitting-curve at the copper calorimeter (integrated quantity (3)).

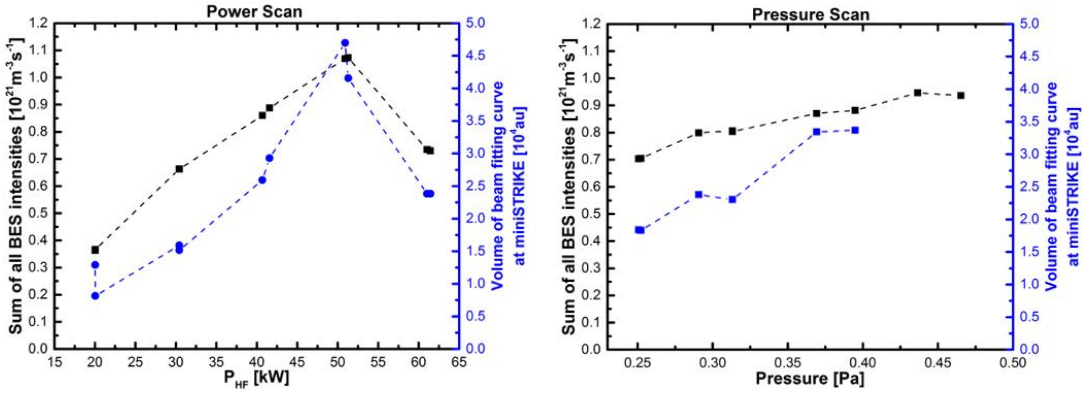

(a) **(b)**

Figure 5.12. Sum of all the BES intensities and volume of the beam-fitting-curve at *mini-STRIKE* for a power scan (left) and a pressure scan (right). The other operational parameters are listed in the caption of Figure 5.2a and Figure 5.2b respectively.

To conclude, a physical interpretation of the trend of Figure 5.12a is provided; this plot was indeed quite unexpected since it is quite in contrast with previous measurements at BATMAN. As explained at the beginning of this chapter, an increase in the RF power is theoretically expected to result into an increase of the ion current density, leading consequently to an increase of all the integrated quantities; however, this plot shows a *decrease of the integrated quantities (1) and (2) when passing from 50 kW to 60 kW.*

The explanation of such behavior is given by Figure 5.14: the electrically measured ion and electron currents and the H^- density in front of the PG from Cavity Ring Emission Spectroscopy (CRDS) are plotted as a function of the RF power. When passing from 50 kW to 60 kW, the amount of ions in front of the PG increases (green points) but the extracted ions - namely those who exit the extraction grid - are constant (black points). It can be deduced that the missing ions hit the EG together with the co-extracted electrons (red points) because of very bad beam optics (high divergence); for the same reason part of the j_{ex} can be expected to intercept the

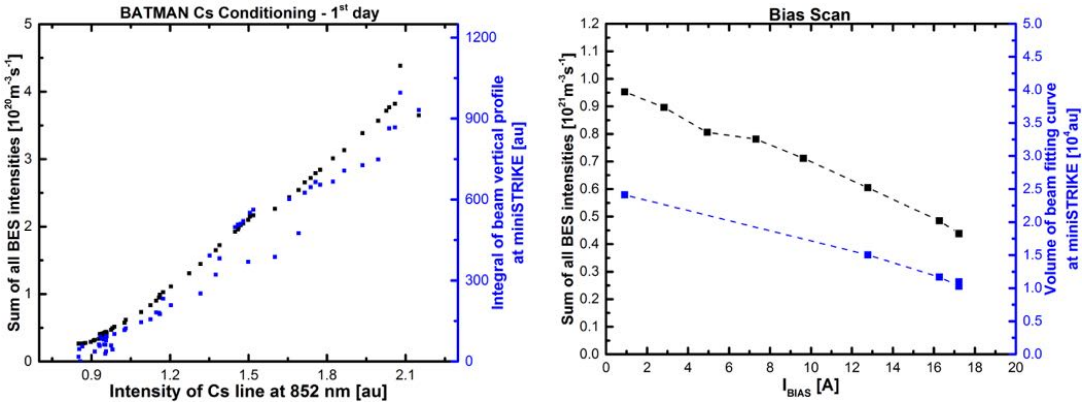

(a) **(b)**

Figure 5.13. Sum of all the BES intensities and volume of the beam-fitting-curve at *mini-STRIKE* for a Cs-conditioning day (left) and a bias scan (right). The other operational parameters are listed in the caption of Figure 5.3a and Figure 5.3b respectively.

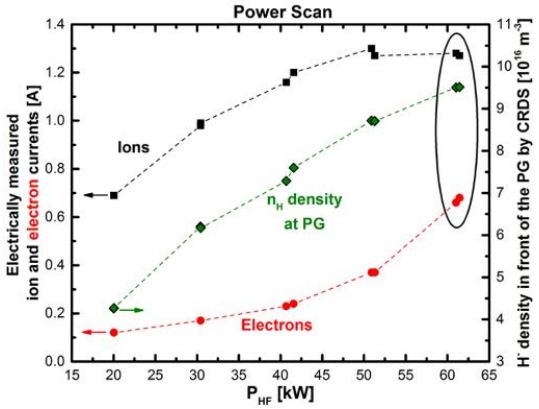

Figure 5.14. Electrically measured ion and electron currents and H^- density in front of the PG (provided by laser absorption), as a function of the RF power.

GG, leading to a decrease of the current arriving to the beam diagnostics and thus of integrated quantities (1) and (2). A considerable increase in the beam mean divergence when passing from 50 kW to 60 kW, experimentally measured, bears out this explanation.

5.4.2 Beam inhomogeneity and shift

In this section a detailed characterization of the beam is carried out by means of the three beam diagnostics available at BATMAN. The discussion focuses on two aspects tightly correlated: the *vertical beam inhomogeneity* and the *displacement of the beam center*.

A new indicator - named **asymmetry factor** - is introduced to *"measure" the level of beam vertical inhomogeneity*; it is defined as a proper combination of the five BES-telescope intensities $I_1 ... I_5$:

$$\nu := \frac{(I_4 + I_5 + 0.5 \cdot I_3) - (I_1 + I_2 + 0.5 \cdot I_3)}{(I_1 + I_2 + I_3 + I_4 + I_5)} = \frac{(I_4 + I_5) - (I_1 + I_2)}{I_{TOT}} \tag{5.1}$$

Following this definition, a perfectly symmetric beam has an asymmetry factor of zero; ν is positive for a shifted-up beam, negative for a shifted-down beam and the greater its *absolute* value, the higher the beam inhomogeneity. Figure 5.15 shows three different BES-intensity vertical profiles of the beam: a beam shifted upwards corresponds to positive ν, downwards to negative ν.

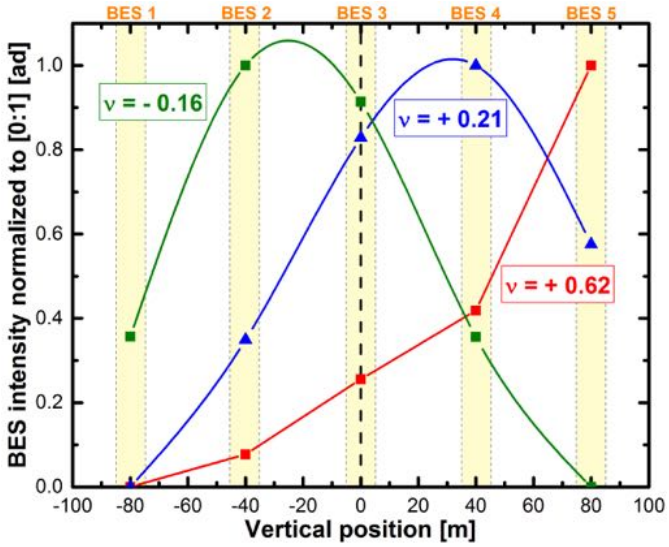

Figure 5.15. Comparison of three different BES-intensity vertical profiles; the position of each BES telescope is also shown.

If for example the amount of light in the upper half $(I_4 + I_5 + 0.5 \cdot I_3)$ were 2-times/3-times the light in the lower part $(I_1 + I_2 + 0.5 \cdot I_3)$, then the coefficient would be $\nu = 0.3$ / $\nu = 0.5$ respectively.

The asymmetry factor ν is strictly correlated with the position of the beam center. This intuitive statement is well confirmed by experimental observations: a movement upwards of the beam profile, given by *mini-STRIKE* or by the copper calorimeter, results always in an increase of the asymmetry factor and viceversa a decrease of ν corresponds to a movement downwards of the *beam center*. This proves again the good agreement between the BES and *mini-STRIKE* discussed in 4.2.3.

The general observations regarding the asymmetry factor ν and the beam inhomogeneity - with "UP" filter field setups - are summarized here and discussed in the following.

- **Statement 1** The asymmetry factor increases during Cs-conditioning (beam center drifts upwards), decreases during Cs-deconditioning (beam center drifts downwards) at z = 3.
- **Statement 2** The asymmetry factor is lower for a higher RF power (beam center drifts downwards) at z = 3, no dependance is found at z = 9.
- **Statement 3** The asymmetry factor increases with the bias current (beam center drifts upwards) both at z = 3 and z = 9.
- **Statement 4** The asymmetry factor does not depend on the source pressure both at z = 3 and z = 9.

Statement 1 discussion

Statement 1 regards the beam dynamics during a Cs-conditioning day in Hydrogen.
The Cs is dispensed into the source from a nozzle located at the top of the rear wall and oriented towards the upper half of the plasma grid (see Figure 3.4). If there is no plasma, the Cs atoms move toward the PG and cover mainly the upper half, creating a relevant vertical asymmetry of the **surface work function**. This asymmetry should be strongly reduced if a plasma is ignited: the plasma is expected to erode the Cs from the surface, ionize the bulk of the Cs atoms and thus redistribute them on all the surfaces with which the plasma interacts (as the lateral walls and the PG).
These intuitive considerations are consistent with results from the *CsFlow3D code* [31], a code for Cs-dynamics modeling under development at IPP. Simulations show that when no plasma is ignited (vacuum phase) Cs atoms tend to accumulate on the very top of the plasma grid (Figure 5.16a); after 5 s of plasma phase the asymmetry is much smaller (Figure 5.16b)[1].

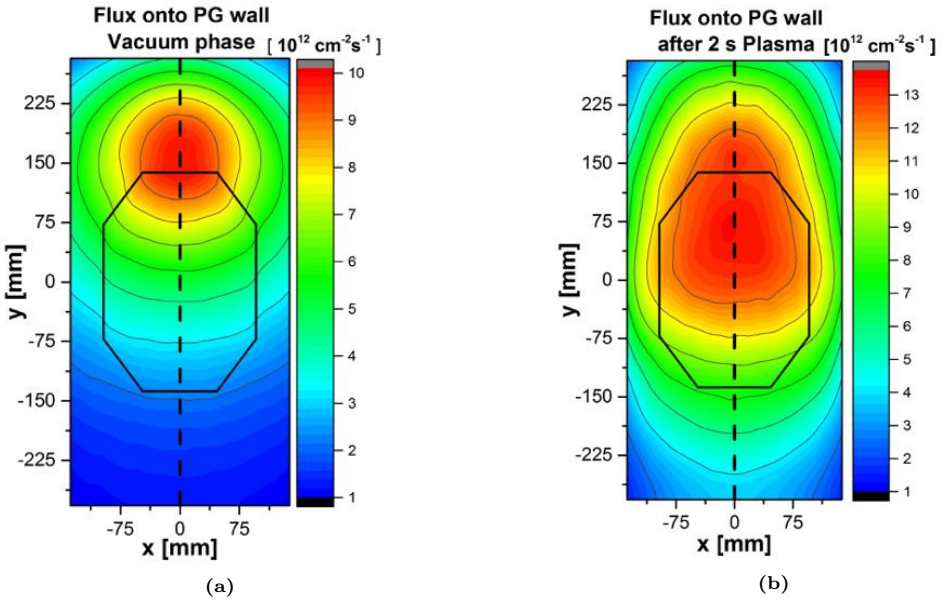

(a) (b)

Figure 5.16. Simulation, by means of the CsFlow3D code [31], of the Cs flux onto the plasma grid wall in vacuum phase (left) and after 2 s of plasma (right).

In Figure 5.17 the asymmetry factor ν as a function of the intensity of Cs line at 852 nm is shown: data refer to two days of Cs-conditioning (grey and blue symbols) and one day of Cs-deconditioning (orange symbols) in hydrogen, and each symbol corresponds to a beam pulse. During Cs-conditioning the source parameters are kept fixed; since Cs is continuously dispensed into the source, the Cs line intensity gradually increases (evolution from the left to the right of the plot). Besides the electrically measured ion current density j_{ex} is found to increase almost linearly with the intensity of the line.

The grey points represent a complete conditioning day: starting from a clean source (Cs line intensity very weak, ≈ 0.8), Cs is gradually dispensed into the source and the asymmetry factor is found to increase. Presumably the ability of the plasma to erode and redistribute the Cs all

[1] Courtesy of Alessandro Mimo (alessandro.mimo@ipp.mpg.de).

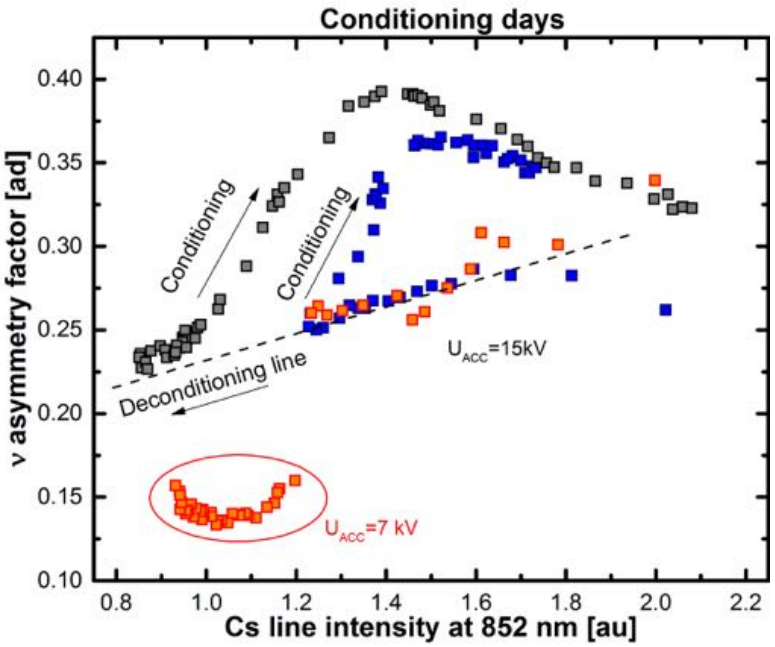

Figure 5.17. Asymmetry factor ν as a function of the Cs line intensity at 852 nm for two conditioning days (grey and blue symbols) and a deconditioning day (red symbols).The other source parameters are $P_{HF} = 60\ kW$, $P = 0.3\ Pa$, $I_{BIAS} = 6\ A$ and $U_{ex} = 5\ kV$.

over the PG is not enough, and Cs accumulates more on the upper half than on the lower half of the grid: this implies an ***increasing vertical asymmetry of the surface work function*** and therefore of the extracted current, leading to a *more and more inhomogeneous beam*.
This interpretation is consistent with measurements of the neutral Cs density in front of the two grid halves via laser absorption: the density on the upper half is virtually *four times the density on the lower half* (Figure 5.18). It is worth to notice that the density estimated via laser absorption represents only a small fraction of the total Cs density: indeed the majority of the Cs atoms are normally not neutral but ionized (up to 90 %).

The increase in the asymmetry factor should correspond to a movement upwards of the beam center seen by *mini-STRIKE* or by the copper calorimeter. This trend is clearly visible with the copper calorimeter for a similar Cs-conditioning day in Hydrogen at z = 3 (October 2006), as shown in Figure 5.19a. The *center of the beam on the copper calorimeter shifts up* by about 40 *mm* in total: the blue and red symbols are separated by a series of beam pulses not considered because the bias current was modified. Figure 5.19b shows some beam profiles given by the calorimeter during another Cs-conditioning day in Hydrogen at z = 3 (February 2007): again the profile is shifting upwards as the amount of Cs in the source increases. The same conclusions can be drawn for the beam profiles measured at *mini-STRIKE* during Cs-conditioning.

Back to Figure 5.17, the asymmetry factor ν decreases if the intensity of the Cs line exceed ~ 1.4: the reason for this inversion of the trend is purely *optical*, namely a change in the optical properties of part of the beam. An explanation is here proposed.
Figure 5.20 shows the divergence of each BES-telescope as a function of the electrically measured ion current density j_{ex} (basically proportional to the intensity of the Cs line at 852 nm); the

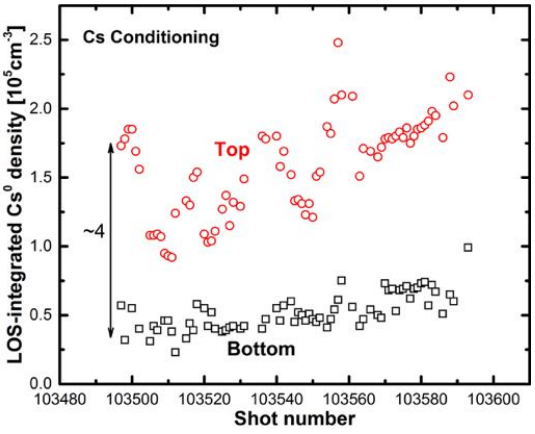

Figure 5.18. LOS-integrated Cs^0 density at the top and bottom of PG, from laser absorption.

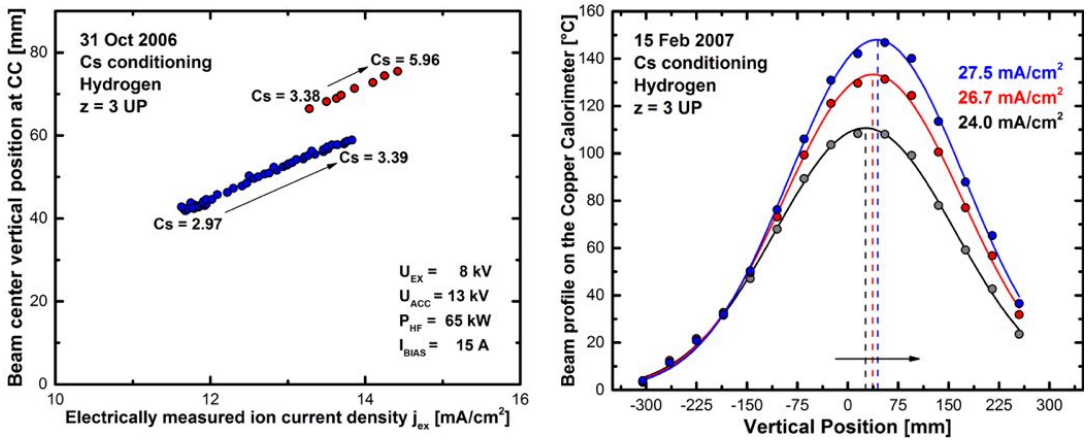

(a) (b)

Figure 5.19. Beam center at the copper calorimeter as a function of the current j_{ex} during a conditioning day (left); beam vertical profiles at the copper calorimeter during a conditioning day (right). The other source parameters for the plot on the right are listed in the caption of Figure 5.11.

data refer to the same conditioning day previously discussed (grey points in Figure 5.17).
If the beam current density is relatively low (below 9 mA/cm^2), an increase in the local current density results in a decrease of all the divergences (Figure 5.20): this implies that the beam is locally *underperveant* along all the five lines-of-sight (for a detailed description of the relation between divergence and current see section 2.4.2).
If we consider the parabolic relationship between divergence and normalized perveance, each BES telescope can be represented by a point located on the left branch of the parabola (Figure 5.21). During the conditioning the increase of local current density leads to an increase of the local beam perveance for all the telescopes: the five points move along the parabola, from left to right, until the point most on the right, namely the BES-telescope with highest intensity, passes to the overperveant branch. This transition is schematically shown in Figure 5.21.
The first point to become overperveant corresponds to BES-telescope #5: when $j_{ex} \sim 9\ mA/cm^2$ ***the upper part of the beam alone undergoes a underperveant-to-overperveant transition***, while the rest of the beam remains underperveant. After the transition, *the optical*

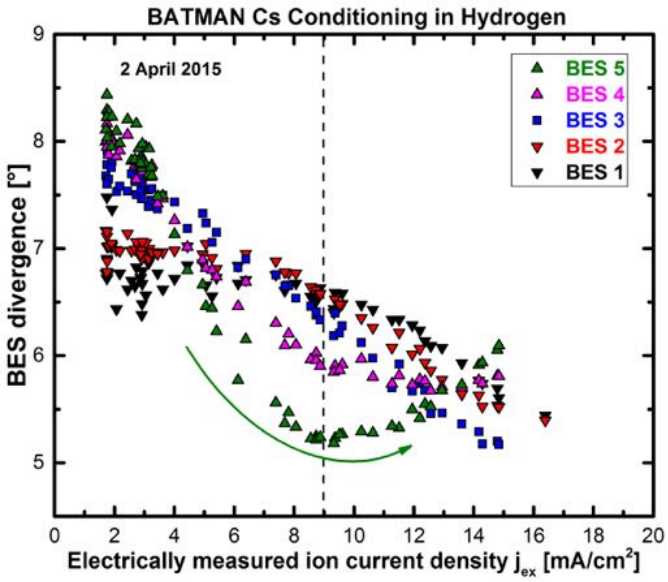

Figure 5.20. BES divergences as a function of the electrically measured ion current density j_{ex}: for BES-telescope #5 the transition from underperveant to overperveant is visible. The fixed operational parameters are: $U_{ex} = 4.5\ kV$, $U_{acc} = 10.3\ kV$, $P_{HF} = 61\ kW$ and $I_{BIAS} = 5.6\ A$.

properties of the beam are no more uniform: the asymmetry coefficient ν continues to describe the beam inhomogeneity but it is no longer correlated with the vertical current distribution at the PG. A further increase in the ion current density results in a *de-focalization of the upper part* of the beam (overperveant) and in a *focalization of the central and lower parts*.

Figure 5.22 shows the movement of the *beam center* as seen by *mini-STRIKE* .
Before the underperveant-to-overperveant transition of the beam portion seen by BES-telescope # 5, the center drifts upwards with increasing ion current, namely with Cs-conditioning: this is in full agreement with the observations from the copper calorimeter for other conditioning days (Figure 5.19a and 5.19b).
After such transition the beam center is expected to *leave the overperveant part of the beam*, which is de-focusing, and to move towards the underperveant regions, which are focusing; since the center is initially in the upper region, it drifts downwards (Figure 5.22).

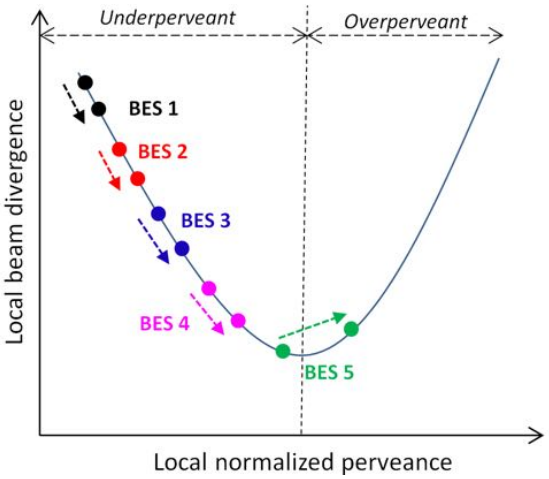

Figure 5.21. Schematic evolution of the five BES divergences during a conditioning day.

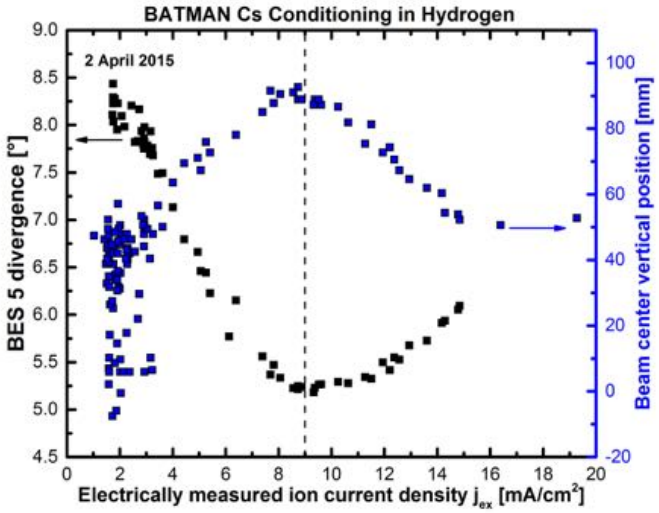

Figure 5.22. Divergence of the BES-telescope # 5 and beam center, as measured by *mini-STRIKE* , as a function of the electrically measured ion current density for a Cs-conditioning day in Hydrogen; the other source parameters are listed in the caption of Figure 5.20.

Statement 2 discussion

Figure 5.23a shows the effect of the RF power on the asymmetry factor ν for three different magnetic filter field setups: z = 9 UP and DOWN and z = 3 UP. The results, as it will be explained in the following, suggest that with z =3 UP a *vertical asymmetry of the Cs distribution on the PG surface* exists: hence statement 2 is consistent with statement 1.

In the z = 3 configuration (UP), a slight decrease of vertical inhomogeneity with increasing power is visible. Since previous considerations indicate the likely existence of a inhomogeneous Cs distribution on the PG, a higher RF power could result in a *plasma more and more able to erode the Cs from the top half of the PG and re-distribute it on the entire grid*: this re-distribution would indeed lead to a reduction of the vertical inhomogeneity of the surface work function, of the extracted current and consequently of the asymmetry coefficient ν.
The decrease of ν should correspond to a shift downwards of the beam center: this is confirmed by measurements done with *mini-STRIKE* calorimeter (see Figure 5.23b).

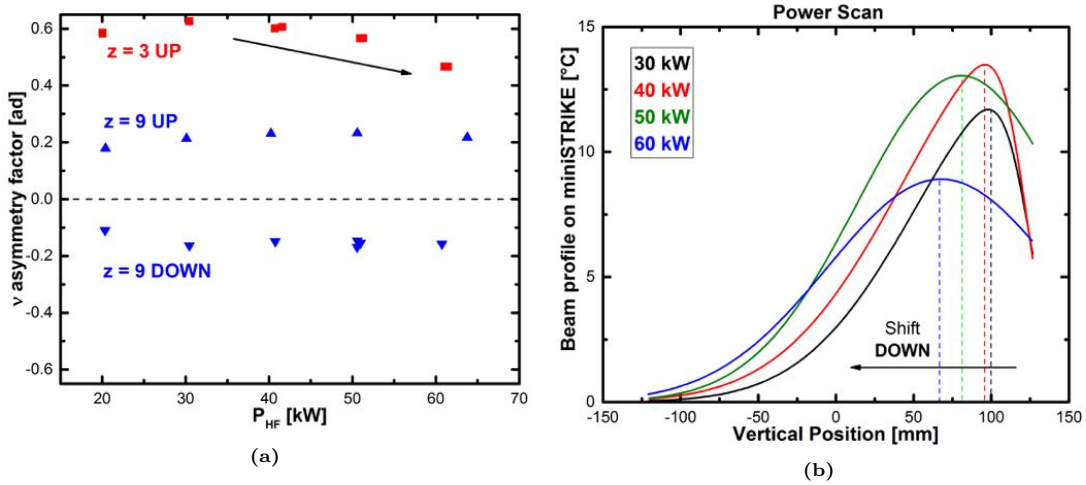

Figure 5.23. Asymmetry factor *nu* as a function of the RF power for different magnetic setups (left); evolution of the beam vertical profile - as given by *mini-STRIKE* - with increasing power (right). The other source parameters are listed in the caption of Figure 5.2a.

In the z = 9 case, on the contrary, ν does not depend on the RF power (Figure 5.23a, blue symbols) both in the UP and DOWN magnetic setups; this lack of dependency can be explained if we suppose that *at z = 9 the Cs asymmetry on the PG is much less important than at z = 3*, namely the Cs is almost homogeneously distributed on the grid surface. A major argument in favor of this interpretation is that UP and DOWN cases are, within the error bars, virtually symmetric with respect to $\nu = 0$ (Figure 5.23a).

The hypothesis that at z = 9 Cs coverage of the PG is more homogeneous than at z = 3 can be explained by physical considerations; a possible interpretation is discussed in the following paragraph.

Cs inhomogeneity and filter field strength The basic idea is that the Cs vertical distribution on the plasma grid depends, in the very first approximation, mainly on (1) the position of the Cs-oven nozzle and (2) the plasma inhomogeneity on the grid; *the reality is far more complicated*

due to the complexity of the plasma dynamics in front of the PG, which is still not completely clear.

Dependency (1) has already been discussed, see "Statement 1". Dependency (2) is due to the vertical $E \times B$ drift of the plasma in front of the PG: the *magnetic filter field* B along the horizontal direction (x - axis) interacts with an *electric field* E normal to the grid, which stems from the potential drop between the plasma potential and the PG potential. The amount of the vertical deviation depends experimentally ([16]) on the strength of the filter field in front of the plasma grid : *with z = 3 the plasma has been found to be more inhomogeneous than with z = 9.* When the plasma impinges on the PG it erodes the Cs on the surface and redistributes it: the eroded region position and shape depend on the plasma vertical drift, namely on the plasma inhomogeneity. Consequently it is reasonable to expect that *the plasma vertical inhomogeneity somehow influences the Cs vertical inhomogeneity*; with z = 3 the Cs vertical distribution is maybe more inhomogeneous than with z = 9.

To sum up, the filter field strength influences the plasma inhomogeneity which, in principle, can influence the Cs inhomogeneity and thus the vertical asymmetry of the PG surface work function. At z = 9 the $E \times B$ drift is smaller than at z = 3, the plasma is more homogeneous and it leads perhaps to a more homogeneous vertical Cs distribution.

Statement 3 discussion

Figures 5.24a and 5.24b show the modifications in the beam vertical profile at *mini-STRIKE* when the bias current is varied: the data refer to beam pulses with the z = 3 UP filter field setup and with Hydrogen or Deuterium.
The *beam center shifts upwards*, namely in the direction of the $v \times B$ drift, if the bias current is increased. Such trend is more visible in Deuterium operation than in Hydrogen operation: indeed in the latter case the beam center is nearly at the edge of the upper tile, where the resolution of *mini-STRIKE* in determining the position of maximum heat flux is not good.

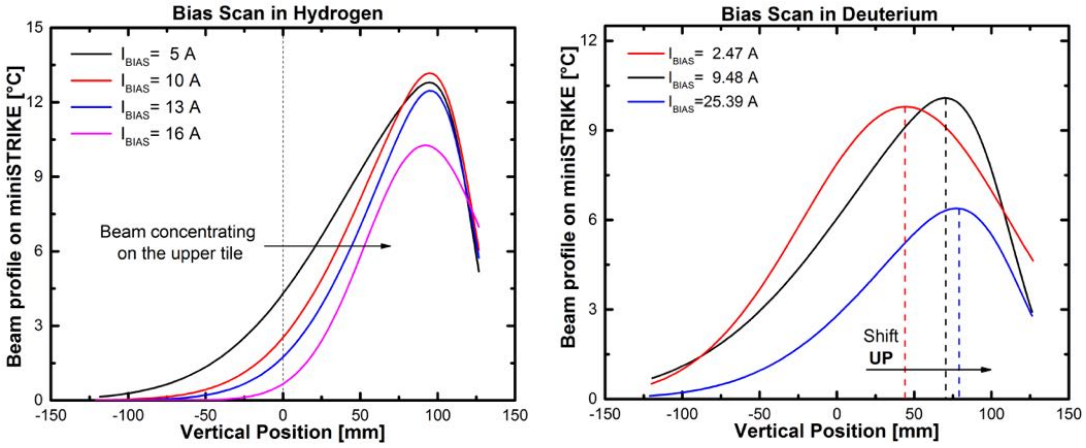

Figure 5.24. Beam vertical profiles at *mini-STRIKE* for a bias scan in Hydrogen (left) and Deuterium (right). The other source parameters are for both scans: $P_{HF} = 40\ kW$, $P = 0.6\ Pa$, $U_{ex} = 5\ kV$ and $U_{acc} = 15\ kV$.

The influence of the bias current on the beam inhomogeneity is still not completely understood, but some physical hypotheses have been proposed to try to interpret the experimental trends; the role of the bias current is an open issue and further investigations will be carried out in the next experimental campaigns.
The current idea is that the bias current may modify the *plasma asymmetry in front of the PG* and thereby the vertical distribution of the H^+ flux impinging on the grid: since the H^+ play a role in creating the H^- of the beam (even though their contribution is much lower than the H^0), a change of the plasma asymmetry can in principle result into a slight change of the beam vertical homogeneity.

In front of the PG there is an electric field E generated by the voltage drop $V_p - U_b$ between the plasma (V_p, plasma potential) and the plasma grid (U_b, bias voltage): this electric field is responsible for a $E \times B$ drift of the plasma, leading to a plasma vertical asymmetry on the PG. A change of the bias current can induce a change of the bias voltage, which will result in a modification of the electric field strength: this leads to a *vertical movement of the plasma*. Since by increasing the bias current the beam experimentally shifts up, it is reasonable to think that the plasma on the PG is moving upwards (see Figure 5.25).

In Figure 5.26 the asymmetry factor ν as a function of the bias current, for different magnetic configurations and at fixed source parameters, is shown; several important observations can be drawn from this plot.
Firstly it indicates that the stronger the magnetic filter field - passing from z = 14 (black sym-

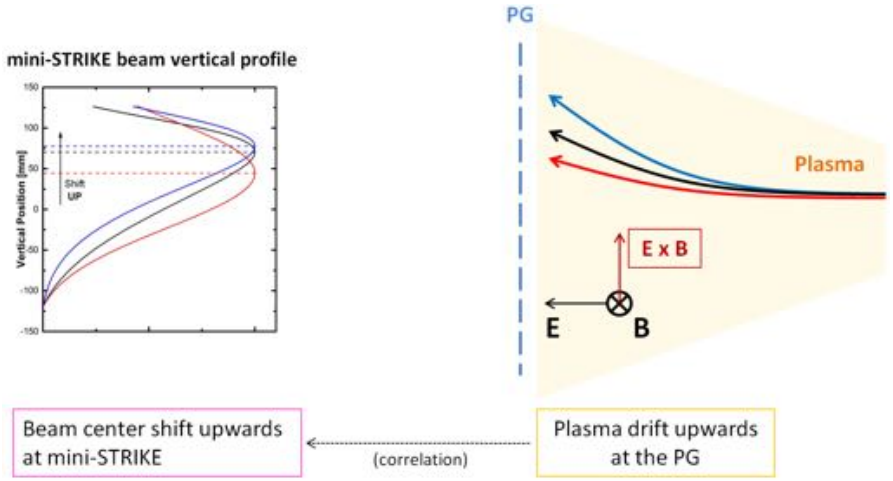

Figure 5.25. Schematic view of one possible explanation of the beam movements during a bias scan: the bias influences the plasma drift in front of the PG, which is possibly correlated to the beam center shift seen by *mini-STRIKE* .

bols) to z = 9 (blue symbols) and then z = 3 (red symbols) - the higher the asymmetry factor in absolute value: this indicates that a stronger filter field results in a higher beam deviation from the horizontal. It may also be noted that at z = 14 the filter field is so weak that no asymmetry is visible. Secondly, the trends at z = 9 UP and DOWN are symmetric with respect to the (dashed) line $\nu = 0$: this suggests (1) that no remarkable vertical Cs-inhomogeneity at the PG exists with z = 9 - otherwise a positive offset would be observed - and (2) that the influence of the bias current on the beam center position is connected to the polarity of the magnetic field. Observation (2) is consistent with the interpretation of the effect of the bias on the beam discussed above.

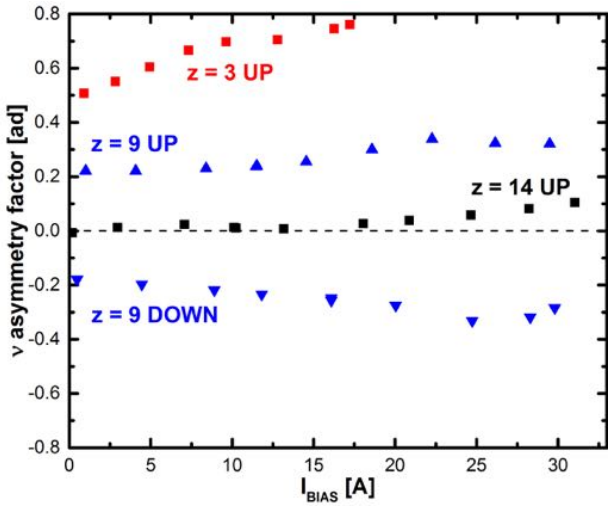

Figure 5.26. Asymmetry factor ν as a function of the bias current for different magnetic filter field setups, working in Hydrogen.

Statement 4 discussion

Figure 5.27 shows the beam asymmetry factor ν as a function of source pressure for different magnetic filter field setups.
It may be pointed out that all trends are flat within the error bars, namely *the pressure of the gas in the source does not influence the vertical asymmetry of the beam.* The position of each group of points - z = 3 UP, z = 9 UP or DOWN, z = 14 UP - is consistent with the strength or polarity of the filter field; furthermore, the symmetry of the z = 9 UP and DOWN cases with respect to the (dashed) line $\nu = 0$ bears out the hypothesis that at z = 9 the Cs vertical asymmetry on the plasma grid is much lower that at z = 3.
The pressure of the source and of the vacuum tank are correlated, namely the tank pressure changes during a source pressure scan. At z = 9 the range explored is $(2.2 \div 5.5)\ 10^{-4}$ mbar, at z = 3 is $(0.9 \div 1.5)\ 10^{-4}$ mbar.

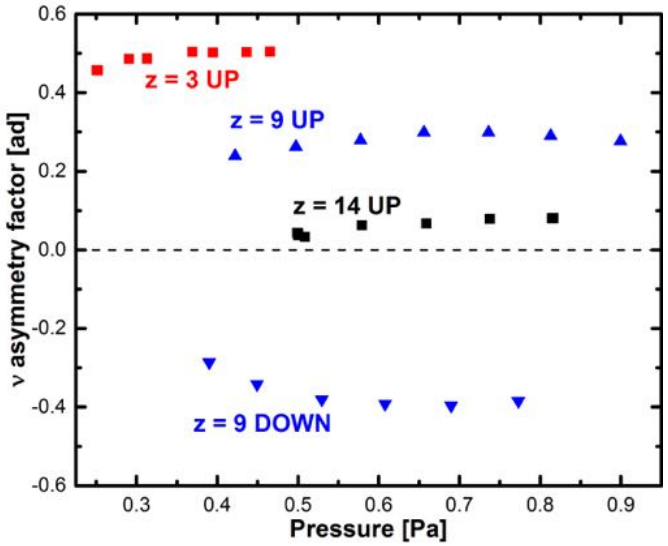

Figure 5.27. Asymmetry factor ν as a function of the source pressure for different magnetic filter field setups, working in Hydrogen. The other source parameters are listed in the caption of Figure 5.2b.

5.5 Influence of the ion mean energy

This section studies the influence of the ion mean energy on the properties of the beam.
The experimental scans analyzed here have been performed at fixed source parameters, fixed extraction voltage ($U_{ex} = 5\ kV$) and variable acceleration voltage: U_{acc} ranges from 6 kV to 15 kV. The electrically measured ion current density j_{ex} is constant ($\sim 22\ mA/cm^2$) whilst the mean energy per ion, proportional to the total voltage of the grid system $U_{HV} = U_{ex} + U_{acc}$, goes from 11 keV to 20 keV.

5.5.1 Trend of integrated quantities

Figure 5.28 shows the sum of the five BES intensities and the volume of the beam-fitting-curve at *mini-STRIKE* as a function of the acceleration voltage U_{acc} and total voltage U_{HV}; both the quantities increase with U_{acc}, but the reasons are different.

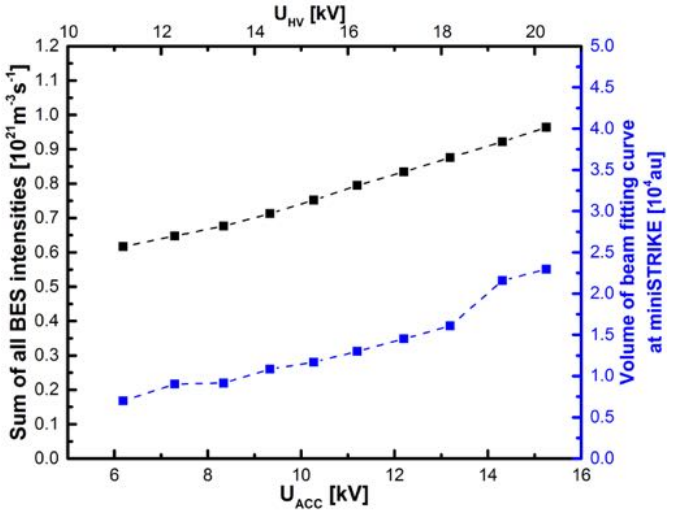

Figure 5.28. Sum of the five BES intensities and volume of the beam-fitting-curve at *mini-STRIKE* as a function of the acceleration voltage U_{acc} or of the total voltage U_{HV}. The other source parameters are $P_{HF} = 50\ kW$, $P = 0.5\ Pa$, $I_{BIAS} = 1\ A$ and $U_{ex} = 5\ kV$.

The dependence between U_{acc} and the sum of the BES-telescope intensities is *optical*. The acceleration voltage influences beam divergence and at the same time the BES-telescope intensity depends on the beam optics (see 2.4.2): a higher voltage results into a more focused beam, leading to a higher sum of the BES-telescope intensities.
The increase of the volume of the beam-fitting-curve at *mini-STRIKE* shows *more directly* the variation of the beam energy; indeed the beam current is fixed and the volume of the beam-fitting-curve on *mini-STRIKE* is, in first approximation, proportional to the total energy of the beam U_{HV} (Eq. 4.19).

5.5.2 Beam inhomogeneity and shift

The mean energy per particle influences in principle the vertical beam inhomogeneity because changes the intensity of the $v \times B$ deflection of the beam due to the filter field B in the drift region: this effect, already discussed, is schematically sketched in Figure 5.4.
A change of the acceleration voltage U_{acc} implies a change of the mean velocity v of the ions, which is proportional to the square root of the total voltage ($v \sim \sqrt{U_{ex} + U_{acc}}$); as a consequence the Larmor radius r_L of the particles changes ($r_L \sim v$). When U_{acc} is increased both the velocity v and the Larmor radius will increase, resulting into a decrease of the vertical $v \times B$ shift of the beam.
This simple reasoning states that with increasing beam energy the beam center vertical position - and similarly the asymmetry factor ν - are expected to approximate the zero from positive values if the field polarity is UP, from negative values if the field polarity is DOWN.

However, the experimental results go against these statements: for every explored magnetic configuration (z = 3 UP, z = 9 UP and DOWN, z = 14 UP) the beam center gets away from the zero with increasing acceleration voltage (Figure 5.29a); the absolute value of the asymmetry factor ν increases as well, namely *the beam is more and more inhomogeneous* (Figure 5.29b). Such trend is visible also with the copper calorimeter: Figure 5.30 compares two beam vertical profiles, at fixed source parameters, with different U_{acc}: even though the increase of the acceleration voltage is small (from 11 keV to 13 keV), the profile clearly shifts up by $\sim$ 30 mm.

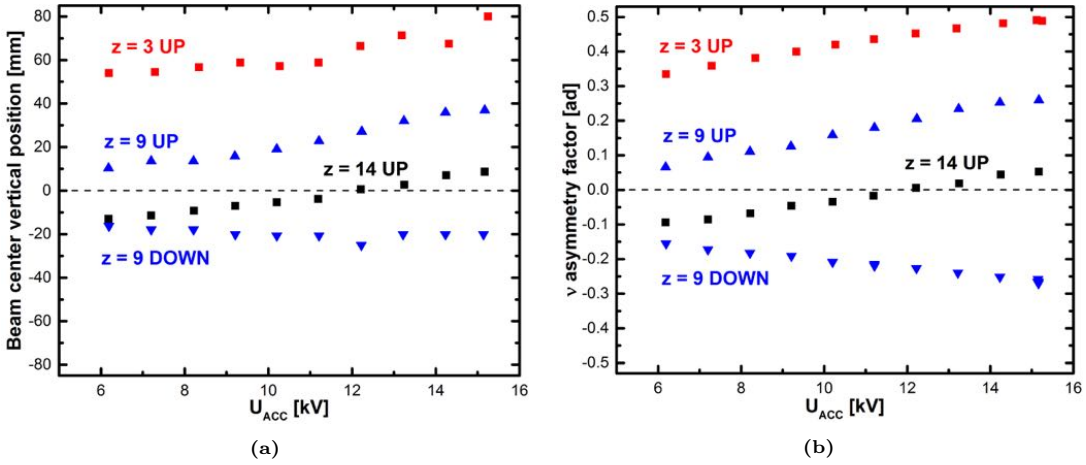

Figure 5.29. Asymmetry factor ν (left) and beam center given by *mini-STRIKE* (right) as a function of acceleration voltage for different magnetic setups. The other source parameters are $P_{HF} = 50\ kW$, $P = 0.5\ Pa$, $U_{ex} = 5\ kV$ and $I_{BIAS} = 1\ A$ (for z =3 UP) or 10 A (for z = 9 and z = 14).

Such behavior is completely unexpected and it is still an open issue. In the following a possible interpretation is presented; the interpretation is based on a simple single-particle code which does not take into account the beam dynamics or other physical phenomena happening in the extraction, acceleration and propagation of the beam. This code was written not with the aim of explaining exhaustively the issue, but just to provide some interesting *hints for future investigations*.

The idea is to observe how an ion trajectory in the vacuum chamber is affected by the filter field: the filter field is shown in Figure 3.3 and it can be noticed that it changes polarity in the drift region.

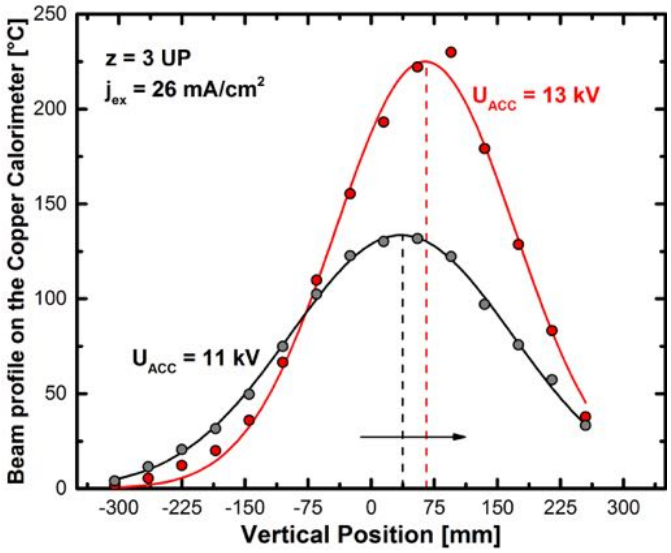

Figure 5.30. Movement upwards of the beam profile, as seen by the copper calorimeter, if - at fixed source parameters - the acceleration voltage is increased from 11 kV to 13 kV; the other source parameters are $P_{HF} = 66\ kW$, $P = 0.5\ Pa$, $I_{BIAS} = 2\ A$ and $U_{ex} = 10\ kV$.

The magnetic filter field along the beam axis and the grid voltages are given as input to the code. The vertical position (y - axis) and velocity of the ion are computed iteratively every 60 nm along the z - axis; an estimate of the ion trajectory, namely the vertical position of the particle along the beam direction, is given as output.

Figure 5.31a shows the trajectory of a H^- ion along the vacuum chamber for two acceleration voltages, 5 kV (green line) and 15 kV (red line); the filter field profile is also drawn with a pink-dashed line (z = 3 UP setup). Given the simplicity of the code, the *absolute value* of the ion vertical deviation is not meaningful; however, the *shape* of the trajectory and its dependence on U_{acc} provide important hints.

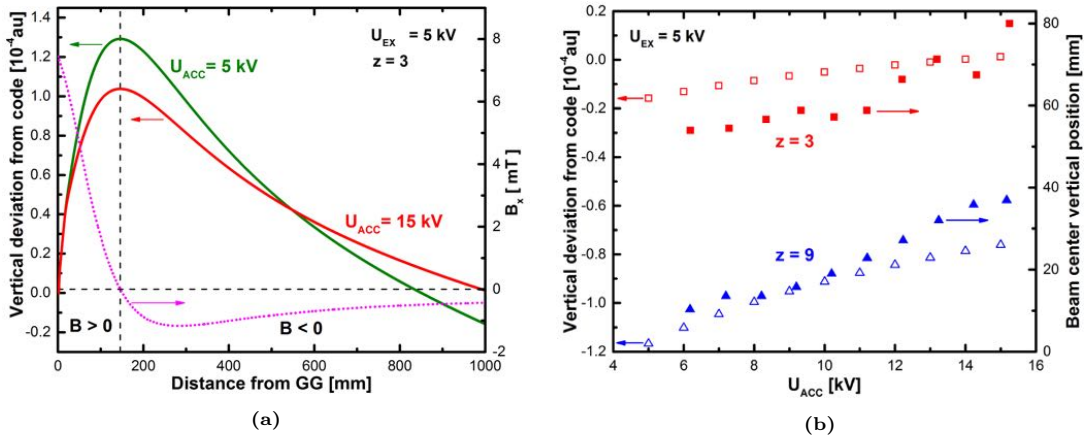

Figure 5.31. Left: vertical position of a H^- ion along the drift chamber for two different acceleration voltages and profile of the filter field strength. Right: vertical deviation of the ion at a distance of 1 m from the GG (empty symbols) and beam center at *mini-STRIKE* (full symbols) as a function of U_{acc}.

Figure 5.31a indicates that if the energy of the particle is increased ($U_{acc} = 5\ kV \rightarrow U_{acc} = 15\ kV$), in the first zone of the drift chamber the net vertical shift lowers: this is in agreement with the simple physical considerations discussed previously, namely that the Larmor radius increases with the ion velocity and thus the vertical shift decreases.
The opposite happens in the zone where the BES and *mini-STRIKE* are located (approximately 0.7 - 1 m downstream the GG): the vertical deviation of the ion is higher for a higher energy, in accordance with the experimental data. Figure 5.31b shows the beam center (from *mini-STRIKE*) and the vertical deviation of the ion at a distance of 1 m from the GG (estimated by the code) plotted against the acceleration voltage: the experimental (full symbols) and simulated (open symbols) trends are similar for both magnetic setups.

5.6 Beam characterization at fixed U_{ex}/U_{acc}

This section discusses the beam properties during a so-called "μ-scan": in this type of scan the extraction voltage U_{ex} and acceleration voltage U_{acc} are both changed from pulse to pulse, but the ratio $\mu := U_{ex}/U_{acc}$ is kept constant (see Figure 5.32a) at the value $\mu = 0.6$.
The study and interpretation of this scan is usually more complicated than the others because two parameters, and not one, are varying at the same time.

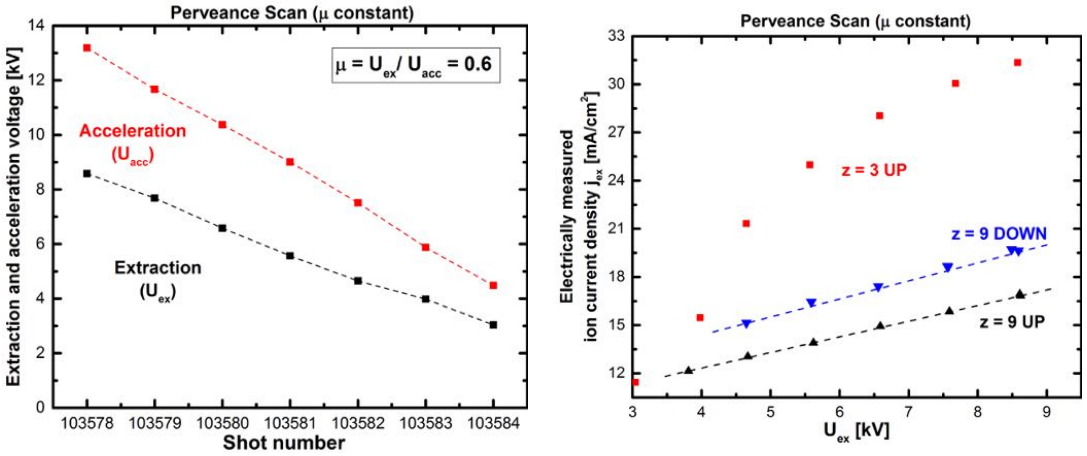

(a) (b)

Figure 5.32. Extraction and acceleration voltages during a typical μ-scan (left); electrically measured ion current density j_{ex} as a function of U_{ex} for μ-scans with different magnetic setups. The other source parameters are $P_{HF} = 50\ kW$, $P = 0.5\ Pa$ and $I_{BIAS} = 1\ A$ (for z = 3 UP) or 10 A (for z = 9).

In Figure 5.32b the electrically measured ion current density is plotted as a function of the extraction voltage for different filter field setups: a higher U_{ex} results into a higher amount of ions extracted from the plasma, leading to a higher ion current density.
A linear dependence between the extraction voltage and the extracted current is observed at $z = 9$: a simple explanation would be that with larger extraction voltage the depth of the meniscus - located at each PG aperture - increases, hence the surface area for ion extraction increases [19]. However this topic is still part of the ongoing investigations.

5.6.1 Trend of integrated quantities

Figure 5.33a and 5.33b show the volume of the beam-fitting-curve at *mini-STRIKE* and the sum of the five BES intensities as functions of the electrically measured ion current density j_{ex}: moving from left to right both the extraction and acceleration voltage increase.
The general expectations, in accordance with what stated in the previous sections, are:

- **Expectation 1.** The volume of the beam-fitting function at *mini-STRIKE* increases with the electrically measured ion current density j_{ex}.
- **Expectation 2.** The sum of the five BES intensities increases with the electrically measured ion current density j_{ex}.

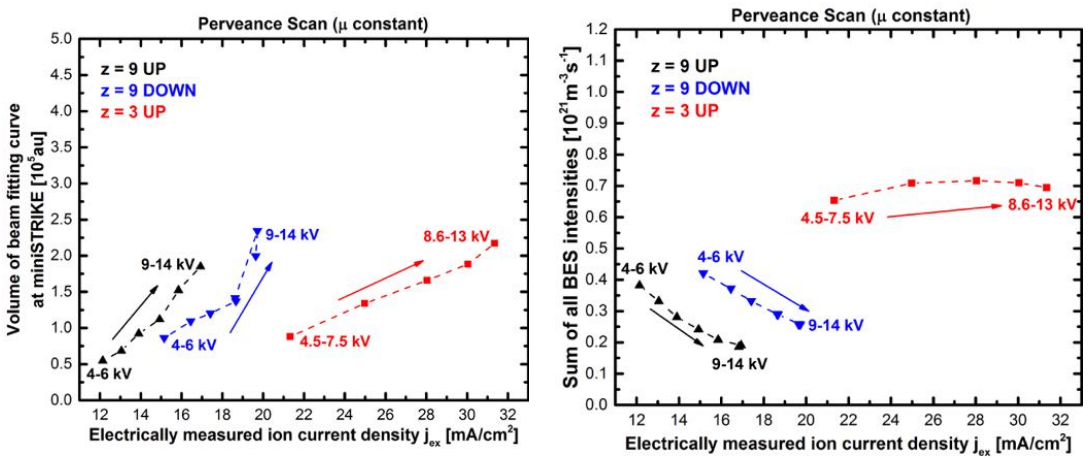

(a) (b)

Figure 5.33. Volume of beam-fitting-curve at *mini-STRIKE* (left) and sum of all the BES intensities (right) as a function of the electrically measured ion current density j_{ex}; the extraction and acceleration voltages for the start and the end of each μ-scan are also indicated. The other source parameters are listed in the caption of Figure 5.32b.

The first expectation is confirmed by Figure 5.33a: the volume of the beam-fitting curve at *mini-STRIKE* increases together with the extracted current j_{ex} for all the magnetic setups explored.

On the contrary, the second expectation is not fully supported by data: as shown in Figure 5.33b, the amount of light collected by the BES slightly increases with the j_{ex} at z = 3 but it decreases with the current at z = 9.
The reason for this decrease is that the beam at z = 9 is *more and more de-focused with increasing voltages* (see Figure 5.34a): the total amount of *emitted* light increases proportionally with j_{ex} but, due to the de-focusing, the amount of *collected* light by the BES-telescopes, which is highly sensitive to the optics of the beam, can in principle decrease (Figure 5.33b) .
A more detailed description of how the extraction and acceleration voltages influence together the beam optics is given in the next paragraph.

Influence of extraction and acceleration voltage on the beam optics The two voltages have a strong influence on the optics of the beam, namely its divergence: for the data here analyzed,

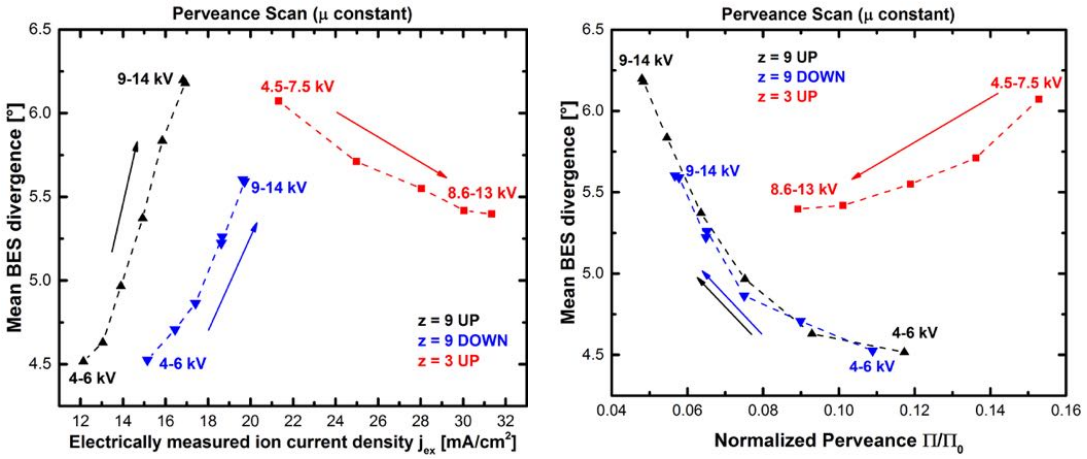

(a) **(b)**

Figure 5.34. Mean BES divergence as a function of j_{ex} (left) and of the normalized perveance Π/Π_0 (right); the extraction and acceleration voltages for the start and the end of each μ-scan are also indicated, while the other source parameters are listed in the caption of Figure 5.32b. The points at z = 9 UP or DOWN are *underperveant* (left branch of the parabolic relationship explained in Section 2.4.2), the points at z = 3 are *overperveant* (right branch).

an increase of U_{ex} corresponds to beam **de-focusing**, an increase of U_{acc} provokes a beam **focusing**. Indeed, if we approximate the dependence between j_{ex} and the extraction voltage U_{ex} (5.32b) with a straight line, the perveance becomes inversely proportional to $\sqrt{U_{ex}}$

$$\Pi/\Pi_0 \sim \frac{j_{ex}}{U_{ex}^{3/2}} \sim \frac{U_{ex}}{U_{ex}^{3/2}} \sim \frac{1}{\sqrt{U_{ex}}}$$

so that an increase of U_{ex} will result in a decrease of Π/Π_0, leading finally to an increase of the beam divergence (in the hypothesis of underperveant beam).
As already stated in section 2.4.2, a higher acceleration voltage is found to focus the beam; a de-focusing effect is possible in principle, but it has never been observed at BATMAN.

In a μ-scan both effects are present, and in principle they can balance or one can prevail on the other. For the scans considered at z = 9, the de-focusing effect given by the U_{ex} prevails since the beam divergence grows with the voltages (Figure 5.34a); at z = 3, on the contrary, the U_{acc} influence slightly prevails since the beam focuses with higher U_{acc}. This concept is schematically represented in Figure 5.35 for the z = 9 setup.

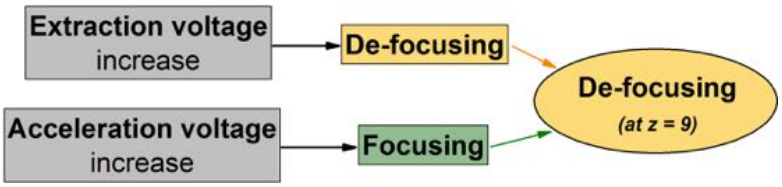

Figure 5.35. Schematic representation of the influence of the extraction and acceleration voltages on beam divergence during a μ-scan at z = 9.

5.6.2 Beam inhomogeneity and shift

As explained previously, the acceleration voltage influences the mean energy per ion of the beam: a more energetic particle is less vertically deviated by the magnetic filter field because its Larmor radius r_L is higher. The same is true for the extraction voltage since the velocity v of each ion of the beam is a function of the total voltage $U_{HV} = U_{ex} + U_{acc}$ applied to the grids: $v \sim \sqrt{U_{ex} + U_{acc}}$.

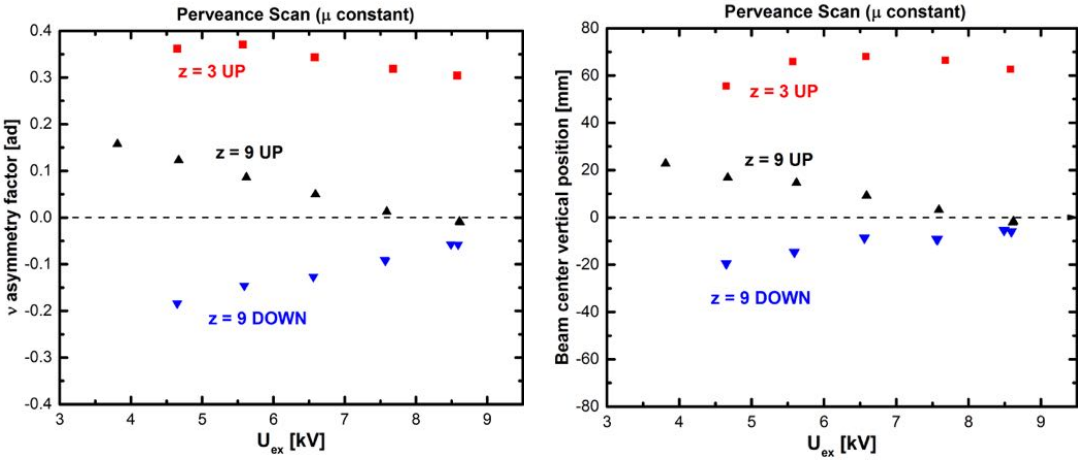

(a) (b)

Figure 5.36. Asymmetry factor ν (left) and beam center given by *mini-STRIKE* (right) as a function of the extraction voltage for μ-scans performed with different magnetic setups; the other source parameters are listed in the caption of Figure 5.32b.

Figure 5.36a and 5.36b show the asymmetry factor ν and the vertical position of the beam center (from *mini-STRIKE*) during a μ-scan, for different magnetic setups.
The experimental trends agree with the theoretical expectations. As the energy per particle increases (with U_{ex} and U_{acc}) the beam shifts towards the zero (central plane of symmetry of BATMAN); the beam center moves downwards for z = 3 UP and z = 9 UP, upwards for z = 9 DOWN.

5.7 Influence of the ion mass (Hydrogen or Deuterium)

This section compares the results obtained when operating the source with Deuterium (D) or Hydrogen (H); the most important conclusions that are discussed in detail in the next paragraphs are as follows.

- There is no major difference in the electrically measured ion current density (j_{ex}) for different gases (H or D) at fixed operational parameters; on the contrary, *the extracted electron-to-ion ratio j_e/j_{ex} is higher in Deuterium that in Hydrogen.*
- The beam vertical inhomogeneity is much less important in Deuterium operation, namely *a Deuterium beam is more homogeneous than a Hydrogen beam.*

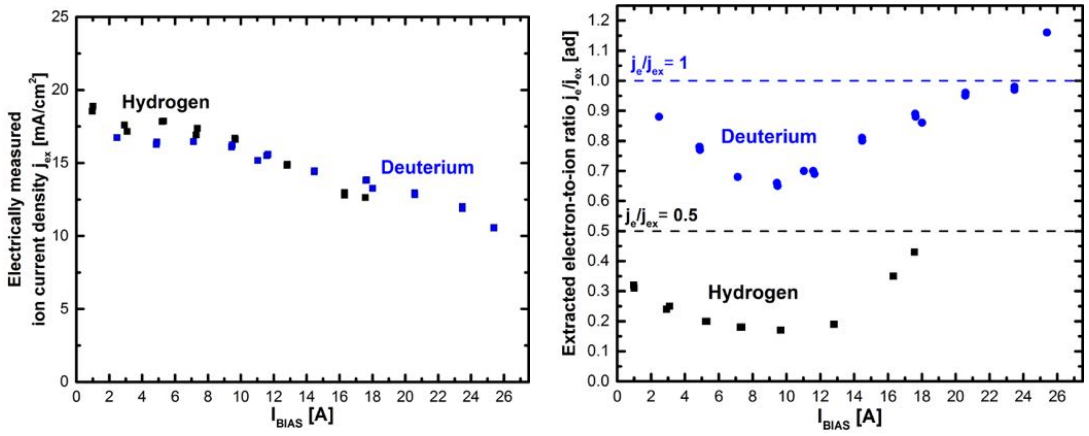

(a) **(b)**

Figure 5.37. Electrically measured ion current density (left) and extracted electron-to-ion ratio (right) as a function of the bias current; Hydrogen (black symbols) or Deuterium (blue symbols) was used as plasma gas. The other source parameters are: $P_{HF} = 40\ kW$, $P = 0.6\ Pa$, $U_{ex} = 5\ kV$ and $U_{acc} = 15\ kV$.

Figures 5.37a and 5.37b show a comparison of the electrically measured ion current density j_{ex} and the extracted electron-to-ion ratio j_e/j_{ex} for Hydrogen and Deuterium operation; the data belong to some bias scans.
At fixed source parameters, in Deuterium operation the amount of extracted negative ions is the same as in Hydrogen but much more electrons are co-extracted: the electron-to-ion ratio is bigger by a factor $2 \div 3$. This feature, probably a mass effect, has been widely observed also in the past ([18]) but an exhaustive explanation does not exist yet. In Figure 5.37b the ITER requirements for Hydrogen ($j_e/j_{ex} < 0.5$) and Deuterium ($j_e/j_{ex} < 1$) are also shown.

On the other hand, Deuterium results into a quite favorable effect, namely a more homogeneous beam: Figure 5.38 shows the vertical profile of the beam as seen by *mini-STRIKE* in Hydrogen and Deuterium operation at fixed source parameters and ion current density.
This feature is likely to be linked to the higher mass of Deuterium: a higher mass results into a larger Larmor radius of the beam ions ($r_L \sim m$), leading to a lower $v \times B$ deflection from the horizontal. Furthermore, experimental measurements of the plasma density in front of the PG have shown that a Deuterium plasma is more homogenous that a Hydrogen plasma: a more homogenous plasma is expected to produce a more homogenous beam.

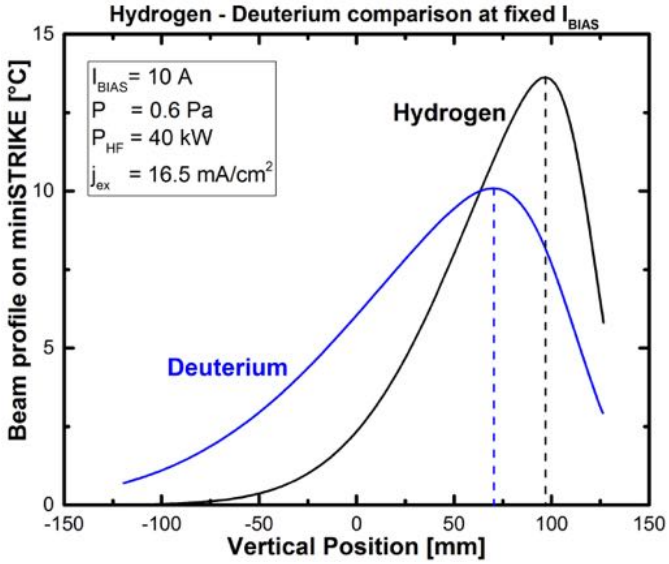

Figure 5.38. Comparison of the beam vertical profile at *mini-STRIKE* with Hydrogen and Deuterium: the source parameters, as well as the ion current, are fixed.

6 Conclusions

The ITER fusion experimental reactor will need a neutral beam system to heat the plasma at the temperature required for nuclear fusion to occur. The neutral beam is obtained from a negative ion beam (Hydrogen or Deuterium), which is extracted from a large RF-driven ion source.
The RF-driven cesiated negative ion source of BATMAN (BAvarian Test MAchine for Negative ions) test facility, located at IPP (Max-Planck Institute, Garching, Germany), is since 2007 the ITER prototype source.

The aim of this work has been to characterize the negative ion beam of BATMAN in different experimental conditions: with different gases (Hydrogen or Deuterium), with different magnetic filter field configurations (type, position and polarity of the permanent magnets), with different source parameters (e.g. RF power, source pressure, bias current, extraction and acceleration voltages). The beam diagnostics available are both calorimetric (the diagnostic calorimeter *mini-STRIKE* and a copper calorimeter) and spectroscopic (5 lines-of-sight for Beam Emission Spectroscopy, BES).
Existing codes for data analysis have been updated or completely re-written during the thesis; physical interpretations for the results, in some cases supported by numerical simulations developed ad hoc, have been discussed. The software developed for the data analysis of *mini-STRIKE* , in particular, will be the core of the future program for the measurements of the STRIKE calorimeter.

6.1 Main results

The main results are here briefly summarized; a detailed treatment can be found in the second part of Chapter 4 and in Chapter 5.

- **General agreement between the three beam diagnostics at BATMAN**. A good *proportionality* between the integrated quantities of the beam diagnostic and the ion current density j_{ex} has been found (Section 5.4.1): this indicates a general consistency between the beam diagnostics and the electrically measured ion current.
  Also a clear correlation exists between the *asymmetry factor* ν, introduced for the first time in this work and computed from the five BES intensities (Eq. 5.1), the *beam center given by mini-STRIKE* and the *beam center of the copper calorimeter*: these quantities have been used in multiple experimental situations to characterize the beam in terms of vertical inhomogeneity and asymmetry.
  Finally the vertical temperature profile given by *mini-STRIKE* was found to agree very well with the five BES intensities (Figure 4.17 and Section 4.2.3).
- **Source performance with and without Cs**. If the source is operated at 0.3 Pa without Cs - namely in *volume production* - the electron-to-ion ratio j_e/j_{ex} is much higher than with Cs, the amount of ion current is lower and consequently the beam divergence is higher

(Section 5.3): as expected without Cs the source is not able to meet ITER requirements (Table 3.1).

- **Filter field influence on the beam**. The filter field setup plays an important role in the beam positioning and thus the top-bottom asymmetry: *the stronger the field in the drift region the higher the vertical deviation of the beam* (Section 5.2). With the $z = 3\ UP$ filter field setup - i.e. strong field in the drift region - the beam vertical deviation was found to be up to 10 cm at 1 m from the GG - where *mini-STRIKE* is located - and up to 8 cm at 1.7 m from the GG - namely on the copper calorimeter - depending on the other source parameters (e.g. the RF power, bias current, extraction and acceleration voltage) .

- **Cs coverage on the plasma grid at BATMAN**. Operating the source at $z = 3\ UP$, data analysis suggests that *the Cs coverage of the plasma grid is not homogeneous but a vertical top-bottom asymmetry exists*. This asymmetry increases during the conditioning of the source with Cs (Section 5.4.2) and it is reduced by increasing the RF power (Section 5.4.2) or by increasing the bias current (Section 5.4.2). Such results have been obtained by comparing data from all the beam diagnostics: the asymmetry factor ν from the BES, the beam shape and the location of the beam center from both *mini-STRIKE* and the copper calorimeter.

- **Hydrogen or Deuterium beam**. A Deuterium beam is more homogeneous than a Hydrogen beam, probably as a consequence of the higher mass; at fixed source parameters, the amount of extracted negative ion current is the same as Hydrogen but the electron-to-ion ratio j_e/j_{ex} is three times higher (see Section 5.7).

Further investigations are required to solve some *open issues*, like the influence of the acceleration voltage on the beam properties (Section 5.5). Indeed the movement of the beam center, when the acceleration voltage is increased, is the opposite of what one can expect from simple theoretical considerations, i.e a $v \times B$ interaction between the velocity of the beam ions v and the filter field B in the drift region.

6.2 Future developments

BATMAN upgrade An important BATMAN upgrade is planned for 2016: it will involve both the source region, with a new driver and grids, and the drift region, with more BES telescopes, a new copper calorimeter and an additional tungsten-wire calorimeter.

The circular driver will be temporarily substituted with a *"race-track"* driver as shown in Figure 6.1a. A new system of four multi-aperture grids will replace the current grids: the apertures, which are similar to the ones of the ITER negative ion source, are organized in a beamlet-group of 14 x 5 holes, as shown in Figure 6.1b. [1]
The number of BES telescopes will increase, for a total of 9 or 10 horizontal lines-of-sight arranged in a vertical array. The current copper calorimeter will be replaced by a thicker one with 29 thermocouples displaced as a cross; finally, when *mini-STRIKE* is not mounted, a tungsten-wire calorimeter will be positioned in its place.

[1] Courtesy of Guillermo Orozco (guillermo.orozco@ipp.mpg.de) and Riccardo Nocentini (riccardo.nocentini@ipp.mpg.de).

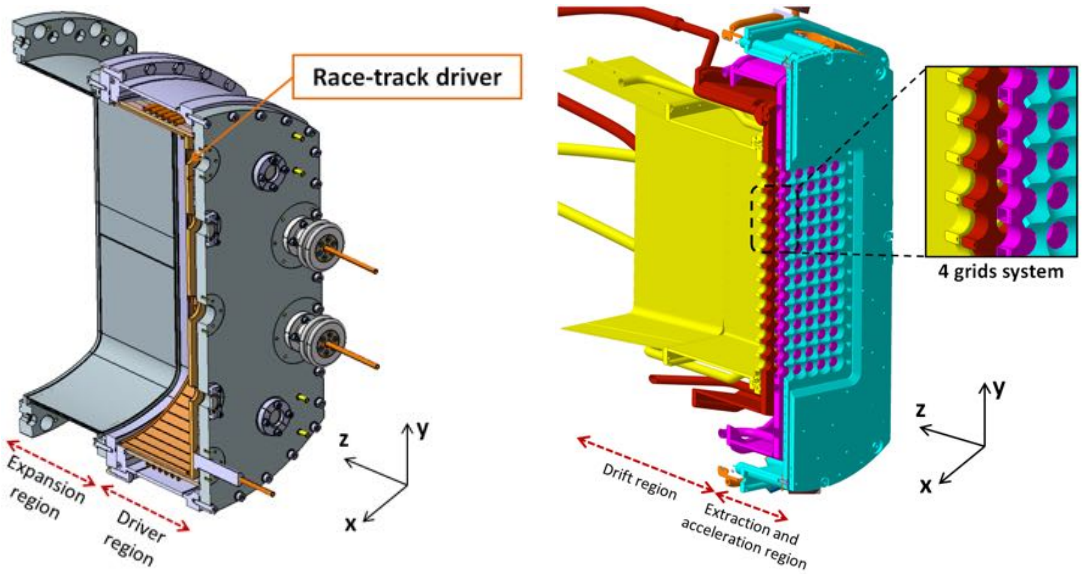

(a) (b)

Figure 6.1. Upgrade of BATMAN test facility planned for 2016: section view of the new *race-track* driver (left) and the new four-grids extraction and acceleration system (right).

Quantitative characterization of the beam The beam property characterization given in the current dissertation is primarily *qualitative*: the next natural step is to study the beam of BATMAN *quantitatively*.
In order to do so it is necessary to develop and improve the codes, already used at IPP, for advanced beam simulation: *KOBRA 3D*, which simulates the beam between the grids, *BBC-NI* (Bavarian Beam Code for Negative Ions), which simulates the beam from the plasma grid to the copper calorimeter and the BES spectra as well, and finally *ONIX* (Orsay Negative Ions eXtraction), which simulates the formation and extraction of negative hydrogen ions in a cesiated source as well as the amount of co-extracted electrons. The large number of beam diagnostics which will be available at BATMAN after the upgrade will permit a systematic comparison of simulation outcomes with experimental results and thus a rigorous benchmark of the codes and a detailed interpretation of the experimental data.

Bibliography

[1] J. Freidberg, *Plasma Physics and Fusion Energy*, ch. 3, pp. 50–51. Cambridge University Press, 2007.

[2] H. Bosch, "Basic nuclear fusion," in *Script of IPP Summer University on Plasma Physics and Fusion Research* (R.Bilato and R.Kleiber, eds.), pp. 35–50, 2014. Unpublished.

[3] C. Hopf *et al.*, "Plasma Heating: Neutral Beam Injection," in *Script of IPP Summer University on Plasma Physics and Fusion Research*, pp. 1–20, 2014. Unpublished.

[4] M. Bacal and M. Wada, "Negative hydrogen ion production mechanisms," *Applied Physics Reviews*, vol. 2, no. 021305, 2015. doi: 10.1063/1.4921298.

[5] U. Fantz *et al.*, "Plasma heating: Neutral beam injection." Script of IPP Summer University on Plasma Physics and Fusion Research, 2007.

[6] J. D. Callen, *Fundamentals of Plasma Physics*, ch. 2, p. 8. University of Wisconsin, Madison, 2006. Unpublished.

[7] Y. Belchenko *et al.*, "A powerful injector of neutrals with a surface-plasma source of negative ions," *Nuclear Fusion*, vol. 14, no. 113, 1974. doi: 10.1088/0029-5515/14/1/017.

[8] P. Sonato *et al.*, "Status of PRIMA, the test facility for ITER neutral beam injectors," *AIP Conference Proceedings*, vol. 1515, no. 549, 2013. doi: 10.1063/1.4792827.

[9] S.Humphries, *Charged Particle Beams*, ch. 7. Department of Electrical and Computer Engineering, University of New Mexico, 1990.

[10] J. D. Lawson, "Perveance and the Bennett Pinch Relation in Partially Neutralized Electron Beams," *Journal of Electronics and Control*, vol. 5, no. 2, pp. 146–151, 1958. doi: 10.1080/00207215808953898.

[11] W. Ott and F. Penningsfeld, "Beam Divergence and Ion Current in Multiaperture Ion Sources," laboratory report ipp 4/252, Max Planck Institute Fur Plasmaphysik, 1992.

[12] P. Franzen *et al.*, "Progress of the ELISE test facility: results of caesium operation with low RF power," *Nuclear Fusion*, vol. 55, no. 053005, 2015. doi: 10.1088/0029-5515/55/5/053005.

[13] R. Hemsworth *et al.*, "Status of the ITER neutral beam injection system," *Review Scientific Instruments*, vol. 79, no. 02C109, 2008. doi: 10.1063/1.2814248.

[14] R. Hemsworth *et al.*, "Status of the ITER heating neutral beam system," *Nuclear Fusion*, vol. 49, no. 045006, 2009. doi: 10.1088/0029-5515/49/4/045006.

[15] V. Toigo *et al.*, "Progress in the realization of the PRIMA neutral beam test facility," *Nuclear Fusion*, vol. 55, no. 083025, 2015. doi: 10.1088/0029-5515/55/8/083025.

[16] P. Franzen *et al.*, "Magnetic filter field dependence of the performance of the RF driven IPP prototype source for negative hydrogen ions," *Plasma Physics and Controlled Fusion*, vol. 53, no. 115006, 2011. doi: 10.1088/0741-3335/53/11/115006.

[17] M. Froeschle *et al.*, "Recent developments at IPP on evaporation and control of caesium in negative ion sources," *Fusion Engineering and Design*, vol. 84, pp. 788–792, 2009. doi: 10.1016/j.fusengdes.2008.12.063.

[18] E. Speth *et al.*, "Overview of the RF source development programme at IPP Garching," *Nuclear Fusion*, vol. 46, pp. 220–238, 2006.

[19] P. Franzen *et al.*, "Performance of multi-aperture grid extraction systems for an ITER-relevant RF-driven negative hydrogen ion source," *Nuclear Fusion*, vol. 51, no. 073035, 2011. doi: 10.1088/0029-5515/51/7/073035.

[20] W. Ott and F. Penningsfeld, "Spectroscopic Determination of Species and Divergence of Hydrogen Beams in the W7AS Neutral Beam Injectors," laboratory Report IPP 4/258, Max Planck Institute Fur Plasmaphysik, 1993.

[21] P. Sonato *et al.*, "The ITER full size plasma source device design," *Fusion Engineering and Design*, vol. 84, pp. 269–274, 2009. doi: 10.1016/j.fusengdes.2008.11.095.

[22] A. Rizzolo *et al.*, "Design and analyses of a one-dimensional CFC calorimeter for SPIDER beam characterization," *Fusion Engineering and Design*, vol. 85, pp. 2268–2273, 2010. doi: 10.1016/j.fusengdes.2010.09.003.

[23] M. D. Palma *et al.*, "Numerical Assessment of the Diagnostic Capabilities of the Instrumented Calorimeter for SPIDER (STRIKE)," *AIP Conference Proceedings*, vol. 584, no. 1390, 2011. doi: 10.1063/1.3637430.

[24] G. Serianni *et al.*, "First negative ion beam measurements by the Short-Time Retractable Instruments Kalorimeter Experiment (STRIKE)," *Review of Scientific Instruments*, vol. 85, no. 02A736, 2014. doi: 10.1063/1.4861391.

[25] G. Serianni *et al.*, "Negative ion beam characterisation in BATMAN by mini-STRIKE: Improved design and new measurements," *AIP Conference Proceedings*, vol. 060007, no. 1665, 2015. doi: 10.1063/1.4916476.

[26] V. Antoni *et al.*, "Design, installation, commissioning and operation of a beamlet monitor in the negative ion beam test stand at NIFS," *AIP Conference Proceedings*, vol. 060005, no. 1655, 2015. doi: 10.1063/1.4916474.

[27] "Lorentz distribution - Wikipedia." http://en.wikipedia.org/wiki/Cauchy_distribution.

[28] "Gaussian distribution - Wikipedia." http://en.wikipedia.org/wiki/Normal_distribution.

[29] S.Cristofaro, "Characterisation of the BATMAN beam properties by H_α-Doppler shift spectroscopy and mini-STRIKE calorimeter," Master's thesis, Physics and Astronomy Department - University of Padua, 2014.

[30] J. Geddes *et al.*, "Formation of excited hydrogen atoms in electron detachment collisions by 3-25 keV H^- ions," *Journal of Physics B, Atomic and Molecular Physics*, vol. 14, pp. 4837–4846, 1981. doi: 10.1088/0022-3700/14/24/018.

[31] S.Gutser, *Experiments and Simulations for the Dynamics of Cesium in Negative Hydrogen Ion Sources for ITER N-NBI*. PhD thesis, Physics Department - University of Augsburg, 2010.